



University of Salerno

Department of Civil Engineering

PhD course in

Risk and Sustainability in Civil, Architectural and  
Environmental Engineering Systems

PhD Thesis title:

Safeability of a beam-to-column adhesive  
connection for large scale pultruded profiles:  
experimental investigation and modeling

PhD Candidate: Luigi Granata

PhD Supervisor: prof. Francesco Ascione

PhD Coordinator: prof. Fernando Fraternali

Cycle XXXIV (2018-2021)



## Acknowledgements

I want to thank my tutor prof. Francesco Ascione first of all. I would like to express my sincere appreciation for his guide in these years of fruitful collaboration. I am grateful to him both for his academic and human leadership.

I further thank prof. Liberata Guadagno and Dr. Carlo Naddeo, from the Department of Industrial Engineering of University of Salerno, for their scientific and professional support in developing the first part of my research about the durability which was conducted in their laboratory using their equipments.

I further thank prof. Luciano Feo, from the same Department of mine, and Professors Raffaele Landolfo e Mario D'Aniello, from the University of Naples "Federico II" for their scientific and professional support in designing and testing the new dissipative hybrid connection for fiber reinforced composite materials presented in the Part II of this thesis.

Last but not least, I would like to thank Top Glass Industries S.p.A (Milan, Italy - website: [www.topglass.it](http://www.topglass.it)) for providing the pultruded profiles Triglass® and Emanuele Mascherpa SpA (Milan, Italy - website: [www.mascherpa.it](http://www.mascherpa.it)) for providing the adhesive Araldite.

With Dr. Giulia Carozzi (TopGlass) and Drs. Fulvio Doria and Stefano Gombri (Mascherpa) we had several virtual meetings for sharing the developments of the research and to discuss about the strategies to adopt.



# Index

Acknowledgements .....	3
Index .....	5
List of Figures.....	9
List of Tables.....	15
Nomenclature.....	17
Introduction .....	19
State of art on the beam-to-column connection between pultruded profiles .	23
PART I: The mechanical behaviour of a full adhesive beam-to-column connection.....	33
CHAPTER I: Hygrothermal durability of epoxy adhesives used in civil structural applications: an experimental investigation .....	35
1. Introduction and a brief <i>State of Art</i> on the durability of epoxy resins and GFRP material .....	35
1.1. Experimental program and scope .....	36
1.1.1. Materials.....	38
1.1.2. Thermal Analysis .....	39
1.1.3. Specimen fabrication.....	40
1.1.4. Hygro-thermal conditioning.....	42
1.1.5. ENF test procedure.....	43
1.1.6. Compliance-Based Beam Method for evaluating <i>GII</i> .....	44
1.1.7. ENF data analysis.....	46
1.2. Results and discussion .....	48
1.2.1. Thermal investigation of epoxy adhesives .....	49
1.2.2. Absorption behaviour .....	54
1.2.3. Desorption evaluation .....	58
1.2.4. Comparison between experimental and numerical results about absorption .....	60
1.2.5. Variability over the time of the mode II fracture energy .....	65
1.2.6. Further results relative to absorption phenomenon.....	69

1.2.7.	Further results relative to desorption phenomenon .....	71
1.3.	Conclusions .....	74
CHAPTER II: The influence of the hygrothermal aging on the strength and stiffness of adhesives used for civil engineering applications with pultruded profiles: a numerical investigation..... 77		
2.	Introduction.....	77
2.1.	Finite Element Model and simulation.....	77
2.1.1.	Mesh details and boundary condition of the 2D model used for ENF test	77
2.1.2.	Cohesive zone model assumption.....	79
2.1.3.	Load-bearing capacity and governing parameters.....	81
2.1.4.	P- $\delta$ curves: a comparison between numerical and experimental investigation.....	84
2.1.5.	Interface slip and strength: fracture propagation and safe design	90
2.2.	Conclusions .....	96
CHAPTER III: Study of the flexural and shear behaviour of the full beam-to-column adhesive connections with particular regards to the influence of the bonded area, the load condition and hygro-thermal aging..... 97		
3.	Introduction.....	97
3.1.	Experimental program.....	97
3.1.1.	Materials .....	99
3.1.2.	Specimen designation and fabrication .....	101
3.1.3.	Hygrothermal conditioning.....	104
3.1.4.	Experimental set-up .....	106
3.2.	Experimental results .....	110
3.2.1.	Influence of the bonding area extension: variation of the bonded area in terms of the base $b$ .....	111
3.2.2.	Influence of the bonded area extension: reduction of the glued area in terms of height $h$ by neglecting the angles.....	115
3.2.3.	Influence of the bonded area extension: increasing of the glued area by considering a column with a bigger cross section with respect to that of the reference configuration .....	117

3.2.4.	Influence of the load condition.....	118
3.2.5.	Influence of the hygro-thermal conditioning .....	120
3.3.	Stress-strain distribution by DIC .....	123
3.4.	Further considerations about the failure modes .....	127
3.5.	Conclusions.....	128
CHAPTER IV: Mechanical models and closed form solutions for the evaluation of the strength and the stiffness of a beam-to-column adhesive connection between pultruded profiles.....		
		129
4.	Introduction .....	129
4.1.	Phenomenological interpretation of the mechanical behaviour of the beam-column connection.....	129
4.1.1.	Hypothesis of the mechanical model .....	131
4.1.2.	Governing equations .....	133
4.1.3.	Further considerations about the mechanical model .....	137
4.1.4.	About the tangential stresses due to shear and torsion.....	138
4.2.	Adhesive layer deformability (evaluation of the vertical displacement corresponding to the force F).....	139
4.2.1.	Formula proposal for the evaluation of $K\theta$ .....	141
4.3.	Validation of the mechanical model by comparing the numerical results with the experimental ones.....	142
4.3.1.	Further considerations .....	147
4.3.2.	Importance of the adhesive layer deformability.....	150
4.4.	Further comparisons with other experimental results.....	151
4.5.	Conclusion .....	154
PART II: Hybrid GFRP/steel connection suitable for fiber reinforced composite materials .....		
		157
CHAPTER V: The design, production and testing of a dissipative hybrid beam-to-column connection for large scale structures .....		
		159
APPENDICES to the PART I .....		
		161
Appendix A. ....		
		161
Appendix B.....		
		169

Appendix C..... 179  
Appendix D..... 183  
References..... 187

## List of Figures

Figure A. Connections: a) standard joint, b) reinforced column flange and c) gusset plate angles. [25,26].	23
Figure B. Universal connector. [5,6].	24
Figure C. Wrapped connection. [29].	24
Figure D. Idealized cuff connection. [31].	25
Figure E. Experimental specimens with (a) bonded sleeve connection; (b) steel angle connection. [38].	26
Figure F. Section view of the connection system. [40].	26
Figure G. Beam part: a) series W1; b) series F2; c) series F4; d) series F2S. [40].	27
Figure H. Details of the beam.column connections tested: a) BTCJ_fc; b) BTCJ_fcr; c) BTCJ_fcm; d) BTCJ_fcmr. [41].	27
Figure I. Typical specimen: a) Adhesive; b) Bolted. [13].	28
Figure J. Multi-bolted connection. [43].	29
Figure K. Bonded sleeve connection for tubular profiles. [44].	30
Figure L. Single bolted joint configurations. [45].	31
Figure M. Schematic view of the bolted/bonded connection. [46].	31
Figure 1. Specimen fabrication: a) Teflon mold; b) DSC specimen SikaDur30; c) DSC specimen Araldite.	40
Figure 2. SLJ specimens: a) geometry; b) curing phase.	41
Figure 3. Photos of the environmental exposure set-up: a) plastic boxes for SLJ specimens; b) immersion heater and thermometer; c) redoximeter. d) values measurement redoximeter.	42
Figure 4. Sea water parameters. Graphs of the salinity, the temperature and the pH vs time.	43
Figure 5. ENF test procedure: a) Geometry of the ENF tests for the adhesive layer characterization (dimensions in mm); b) Photo of the SLJ specimen and LVDT.	44
Figure 6. Representative experimental P- $\delta$ curves of SLJ specimens with SikaDur 30 and Araldite.	47
Figure 7. Representative experimental R-curves of SLJ specimens for both epoxy resins.	48
Figure 8. Heat flux vs. temperature in the temperature range between -50 and 300 °C of the fresh Systems: a) Sikadur 30 based system; b) Araldite based system.	50
Figure 9. Heat flux vs. temperature in the temperature range between -50 and 300 °C of the isothermally cured systems: a) 1 RUN; b) 2 RUN.	51

Figure 10. Thermogravimetric curves of the Araldite and Sikadur based systems: a) in nitrogen; b) in air.....	53
Figure 11. Photo of the pre-treatment stove of SLJ specimens. ....	54
Figure 12. Resin specimens: a) specimens in test tubes; b) test tubes in cooling system; c) specimen weight control. ....	55
Figure 13. Water uptake curves for epoxy resins, a) sea water, b) tap water. ....	56
Figure 14. Silice used to avoid conditioning of the atmosphere. ....	57
Figure 15. Water uptake curves for SLJ samples and GFRP adherent, a) sea water, b) tap water.....	58
Figure 16. Absorption and desorption behaviour for SLJ samples with Araldite: a) sea water, b) tap water. ....	59
Figure 17. Sikadur30 resins in tap water: a) A1; b) A2; c) A3.....	62
Figure 18. Sikadur30 resins in sea water: a) B1; b) B2; c) B3. ....	63
Figure 19. Araldite resins in tap water: a) A4; b) A5; c) A6. ....	63
Figure 20. Araldite resins in sea water: a) B4; b) B5; c) B6.....	63
Figure 21. SikaDur30 SLJ in tap water: a) TW11; b) TW12; c) TW16. ....	63
Figure 22. SikaDur30 SLJ in sea water: a) SW2; b) SW14; c) SW20.....	64
Figure 23. Araldite SLJ in tap water: a) TW1; b) TW2; c) TW3. ....	64
Figure 24. Araldite SLJ in sea water: a) SW1; b) SW2; c) SW3.....	64
Figure 25. GFRP adherents: a) tap water; b) sea water. ....	64
Figure 26. Araldite Fracture Energy durability: a) seawater, b) tap water. ...	67
Figure 27. SikaDur 30 Fracture Energy durability: a) seawater, b) tap water. ....	68
Figure 28. P-d curve of the Araldite epoxy resins behaviour: Unaged vs Aged (12th month).....	69
Figure 29. Experimental P- $\delta$ curves for unaged and aged specimens: a) SikaDur30; b) Araldite.....	71
Figure 30. Experimental P- $\delta$ curves for unaged and aged specimens (Desorbed) with Araldite. ....	73
Figure 31. View of the 2D Model.....	78
Figure 32. Boundary conditions of the 2D model.....	79
Figure 33. Convergence test: mid-span deflection vs number of elements along the thickness.....	79
Figure 34. Traction-separation law in mode II. ....	80
Figure 35. Maximum load vs limit shear stress curves varying the fracture energy.....	82
Figure 36. Numerical P- $\delta$ curves: a) influence of $\tau_u$ ; b) influence of $G_{II}$ .....	83
Figure 37. Numerical P- $\delta$ curves: influence of $E_1$ . ....	84

Figure 38. P- $\delta$ curves for SLJ with SikaDur30: a) unaged condition; b) aged condition in tap water (absorption only); c) aged condition in sea water (absorption only). .....	87
Figure 39. P- $\delta$ curves for SLJ with Araldite: a) unaged condition; b) aged condition in tap water (absorption only); c) aged condition in sea water (absorption only). .....	88
Figure 40. P- $\delta$ curves for SLJ with Araldite: a) unaged condition; b) aged condition in tap water (desorption); c) aged condition in sea water (desorption). .....	89
Figure 41. Complete interface law $\tau$ -s for the case of absorption: a) SikaDur30; b) Araldite.....	91
Figure 42. Fracture propagation: a) SikaDur30; b) Araldite. ....	92
Figure 43. Points investigated corresponding to the reaching of the shear strength limit value. ....	92
Figure 44. Interface laws for all points were shear strength reached the limit value: a) SikaDur30; b) Araldite. ....	93
Figure 45. Evaluation of $s_{nl}$ : a) bilinear law; b) simplified rigid-softening law. ....	94
Figure 46. Specimen: a) dimension; b) assembly; c) load for type 1 and 2 and glued area.....	99
Figure 47. Variation specimens: a) Group A.1; b) Group A.2; c) Group A.3; d) Group A.4; e) Group A.5; f) Group B. ....	102
Figure 48. Photos of the specimens realized: a) type A.1; b) type A.2; c) type A.3; d) type A.4; e) type A.5; f) type B.....	103
Figure 49. Specimen fabrication steps: a) resin and GFRP pieces; b) GFRP roughened and degreased; c) gluing process; d) steel bars spacers; e) checking the adherents alignment; f) specimen after curing ready to be tested. ....	104
Figure 50. Photos of the environmental exposure set-up: a) plastic boxes for SLJ specimens; b) immersion heater and thermometer; c) redoximeter. d) values measurement redoximeter. ....	105
Figure 51. Sea water parameters. Graphs of the salinity (PSU), the temperature ( $^{\circ}$ C) and the pH vs time. ....	106
Figure 52. Steel rigid arm to apply the load: a) type A (bending+shear); b) type B (shear). ....	107
Figure 53. Steel jacket: a) 3D view; b) lateral view; c) top view. ....	108
Figure 54. Experimental set-up: a) vertical LVDTs; b) horizontal LVDTs; c) DIC; d) data acquisition system. ....	109
Figure 55. Spackle pattern preparation.....	110
Figure 56. F- $\delta$ and M- $\theta$ graphs: a) and d) Group A.1; b) and e) Group A.2; c) and f) Group A.3.....	112

Figure 57. Mixed failure between resin and GFRP for the joint.....	113
Figure 58. Mixed failure between resin and GFRP for.....	114
Figure 59. Cohesive failure (in the adhesive mainly) for .....	114
Figure 60. F- $\delta$ and M- $\theta$ graphs: a) and c) Group A.1; b) and d) Group A.4. .....	115
Figure 61. Cohesive failure (in the adhesive mainly) for .....	116
Figure 62. F- $\delta$ and M- $\theta$ graphs: a) and c) Group A.1; b) and d) Group A.5. .....	117
Figure 63. F- $\delta$ graphs: a) Group A.1; b) Group B. ....	119
Figure 64. GFRP failure.....	119
Figure 65. F- $\delta$ and M- $\theta$ graphs: a) and d) Group A.1 (Unaged); b) and e) Group C.1 (TapWater); c) and f) Group C.2 (SeaWater). ....	122
Figure 66. Strain/stress distribution evaluated by DIC (test 1, Group A.1). ....	124
Figure 67. Result by DIC, stress distribution along the vertical and horizontal direction for Test 1 of Group A.1. ....	125
Figure 68. Result by DIC, stress distribution along the vertical and horizontal direction for Test 2 of Group B.....	126
Figure 69. Tangential stresses trend inside the adhesive layer due to torsion. .....	130
Figure 70. Single lap joint scheme.....	131
Figure 71. Softening rigid bond. ....	131
Figure 72. Correction for the length of the joint width: a) Equivalent tangential stresses distribution; b) final joint scheme.....	132
Figure 73. Governing equation: a) Equilibrium problem of a single lap joint subjected to the normal stresses; b) Reference system. ....	133
Figure 74. Numerical model results in terms of relative displacement $s(z)$ and conjugated shear stress $\tau(z)$ : a) $b_{SLJ}=b$ ; b) $b_{SLJ}=b_{eff}$ . ....	136
Figure 75. Rotational spring for evaluating the adhesive layer deformability. .....	140
Figure 76. Geometrical parameters involved in the mechanical model.....	144
Figure 77. Numerical-Experimental comparison: a) F- $\delta_v$ curve; b) M- $\theta_{conn}$ curve.....	147
Figure 78. ENF test procedure: a) force-displacement curve for Araldite resin; b) geometry of the ENF tests for the adhesive layer characterization (dimensions in mm). ....	148
Figure 79. Influence of the adhesive layer deformability (comparison between the experimental and numerical results of the Group A.1: a) F- $\delta_v$ curve; b) M- $\theta_{conn}$ curve.....	151
Figure 80. Beam-to-column configuration: a) Razaqpur e al. [13]; b) Peng et al. [45]......	152

Figure 81. Comparison with Razaqpur [13] e al.: a)  $F-\delta_v$  curves, b)  $M-\theta_{conn}$  curves..... 153  
Figure 82. Comparison with Peng [45] e al.:  $M-\theta_{conn}$  curves..... 154



## List of Tables

Table 1. Unaged specimen for ENF test.....	37
Table 2. Aged specimen for ENF test.....	37
Table 3. Aged control specimen for Absorption and ENF test. ....	37
Table 4. Total number of specimens fabricated and tested for desorption....	38
Table 5. Mechanical parameters of the adhesives at 23°C (epoxy resins). ...	39
Table 6. Specimens nomenclature.....	60
Table 7. SikaDur30 resins (40mm x 10mm x 1mm).....	61
Table 8. SikaDur30 SLJ (340mm x 25mm x 21mm).....	61
Table 9. Araldite resins (40mm x 10mm x 1mm).....	62
Table 10. Araldite SLJ (340mm x 25mm x 21mm).....	62
Table 11. Adherent GFRP (340mm x 25mm x 10mm).....	62
Table 12. Test results relative to SLJ specimens after absorption period. ....	69
Table 13. Test results relating to the SLJ specimens (Araldite) after the desorption period. ....	72
Table 14. GFRP mechanical parameters. ....	78
Table 15. Values of the governing parameters for unaged and aged conditions. ....	85
Table 16. Fracture propagation zone: experimental-numerical comparison. ....	93
Table 17. Evaluation of the slip $s_{nl}$ by Eqn (25) and (28). ....	96
Table 18. Experimental program.....	98
Table 19. Mechanical parameters of the Triglass® material.....	101
Table 20. Specimens designation. ....	103
Table 21. Results of Groups A.1, A.2 and A.3.....	113
Table 22. Results of the Groups A.1 and A.4.....	116
Table 23. Results of Groups A.1 and A.5.....	118
Table 24. Results of Groups A.1 and B.....	120
Table 25. Results of Groups A.1, C.1 and C.2. ....	123
Table 26. Tangential stresses in the adhesive layer due to Shear and Torsion. ....	139
Table 27. $K_{\theta}$ evaluation. ....	141
Table 28. Values of the geometrical and mechanical parameters of resin and GFRP material. ....	143
Table 29. Joint strength prediction (in terms of force F and bending moment M). ....	144
Table 30. Joint stiffness prediction (in terms of the slope of $F-\delta_v$ and $M-\theta_{conn}$ curves). ....	145
Table 31. Values of for unprotected composite materials and epoxy adhesives. ....	149

Table 32. Partial factors for adhesive connection resistance. .... 150

Table 33. Values of the geometrical and mechanical parameters of resin and GFRP material..... 153

Table 34. Predicted values of the joint strength and stiffness..... 153

Table 35. Data absorption, average and standard deviation values of the resin Araldite..... 162

Table 36. Data absorption, average and standard deviation values of the resin SikaDur 30. .... 163

Table 37. Data absorption, average and standard deviation values of the SLJs with Araldite. .... 164

Table 38. Data absorption, average and standard deviation values of the SLJs with SikaDur 30. .... 165

Table 39. Data absorption of the GFRP adherents..... 167

Table 40. All test results relative to Araldite specimens..... 170

Table 41. All test results relative to SikaDur30 specimens. .... 172

Table 42. Test results in terms of average and standard deviation values relative to Araldite specimens..... 175

Table 43. Test results in terms of average and standard deviation values relative to SikaDur30 specimens..... 177

Table 44. Experimental data of the absorption and the desorption phenomenon relative to SLJ. .... 180

Table 45. Test results relating to the Araldite specimens. .... 184

Table 46. Test results relating to the SikaDur 30 specimens. .... 185

## Nomenclature

$a$	pre-crack in the adhesive layer measured for the notch to the support
$a_e$	Equivalent crack length
$a_{eq}$	equivalent crack length
$a_0$	pre-crack in the adhesive layer
A	Continuous absorption
b	Chapters I & II: Width of the adherents
b	Chapters III & IV: horizontal dimensions of the rectangular adhesive area
$b_{eff}$	Effective stress transfer length
CBBM	Compliance-Based Beam Method
CBT	Corrected Beam Theory
CBTE	Corrected Beam Theory with Effective Crack Length
C.D.	Curing degree
$C_{c0}$	SLJ compliance in ENF test
CFRP	Carbon Fibre Reinforced Polymer
$C_0$	Initial compliance in ENF test
D	Continuous desorption
$d_a$	Distances load application points (bending + shear)
$d_b$	Distances load application points (shear)
DBT	Direct Beam Theory
DSC	Differential Scanning Calorimetry
$E_{app}$	Apparent longitudinal modulus
$E_L$	Longitudinal modulus
ENF	End Notch Failure
F	Force applied at the free end of the built-up beam
FEM	Finite Element Model
FPZ	Fracture Portion Zone
$f_v$	Transverse shear factor
$G_{II}$	Fracture energy in mode II
$G_{II,P_{nl}}$	The energy in mode II corresponding to $P_{nl}$
$G_{II,P_{max}}$	The energy in mode II corresponding to $P_{max}$
$G_{II,P_u}$	The energy in mode II corresponding to $P_u$
$G_{13}$	Shear modulus of the adherents
GFRP	Glass Fibre Reinforced Polymer
h	Vertical dimensions of the rectangular adhesive area
$L_s$	Length of the SLJ

M	Bending moment
$M_t$	Moisture uptake content
P	Force applied at midspan in ENF test
$P_{nl}$	The loss of linearity (nl stands for non-linear)
$P_{max}$	The maximum value of the applied load
$P_u$	The end of the post-elastic zone
RT	Room Temperature
$s_e$	Sliding at the limit elastic stage of the adhesive
$s_{nl}$	Sliding at non linear load
$s_u$	Ultimate sliding
SLJ	Single Lap Joint
SW	Sea Water
t	Thickness of the adherents
$T_g$	Glass Transition Temperature
TGA	Thermogravimetric analysis
TW	Tap Water
$w_0$	weight before exposure
$w_t$	weight after exposure
$\beta_{II}$	Constant Mode II
$\delta$	Chapters I & II: Displacement at midspan in ENF test
$\delta$	Chapters III & IV: Displacement of the beam
$\theta$	Rotation between the beam and the column.
$\mu$	Average values
$\sigma$	Standard deviation values
$\tau_u$	ultimate adhesive shear stress

## Introduction

Fibre Reinforced Polymer (FRP) materials are appealing as alternative to traditional construction materials due to their high tensile strength, excellent resistance to aggressive environments [1–5], high strength to weight ratio, simple and rapid installation time. Also, due to their low maintenance requirements, these materials offer a promising alternative for the development of more durable and sustainable structures [6,7]. Moreover, through suitable combinations of matrix and fibers it is possible to tailor make composite materials to optimally meet specific design requirements.

Presently, pultrusion is the preferred method for production of continuous FRP profiles with constant cross-section, such as hollow sections, angles, I-beams and channels, all being suitable for construction of frame type structures. FRP composites can be made with carbon, glass, basalt or aramid fibers, but glass fibre is commonly used for fabrication of composites materials used in the construction industry due to its relatively lower cost compared to the other types of fibre [8].

Although glass FRP (GFRP) members have high strength and reasonable stiffness, a functional and safe frame structures also require reliable connection systems between the structural members, including beam-to-column connection.

The connections in GFRP structures are deemed to be essential in providing the required load-carrying capacities. Due to the significant impact of the stress concentration and initial defect, the premature failure of the connections may lead to the catastrophic failure of the entire structure, while the load-carrying capacity of the GFRP members may not be fully used, resulting in the inefficient use of the material. In this regard, sufficient strength of the connections serves as the basis in achieving the expected structural behaviour of GFRP profiles.

The connection technology for pultruded GFRP profiles presents numerous challenges due to the brittle and anisotropic nature of the material. GFRP profiles are usually connected via bolting, adopting the design rules for similar steel connections, but in the last decade the adhesive technique has gained more and more interest.

International Standards [9, 10] stipulates those bonded connections should not be allowed for primary load bearing components, where failure of the connection could lead to progressive collapse or unacceptable risks. Their use

is permitted only in combination with or as a backup for bolted connections. At the same time, this prohibition represents one of the key issues that impede the steadily increasing market for FRP profiles in the field of civil construction, which already utilizes 35% of the annual world-wide production of GFRP profiles. The main reason for the prohibition of bonded connections is lack of knowledge about and experience with the performance of such connections. Hence, there is need for research on bonded connections in order to understand their behavior, in terms of strength and stiffness, and to assess their performance vis-a-vis similar bolted connections. The knowledge thus gained can be used by designers to safely design composite structures with bonded connections, provided that it can be demonstrated to be more advantageous than using bolted connections.

Theoretically, there are reasons to believe that bonded connections can be superior to bolted connections in FRP composite structures.

In fact, compared with the traditional mechanical assembly technologies (e.g., bolted, pinned or riveted methods), adhesive bonding has a lot of advantages. First of all, nearly all types of materials, including composite materials in particular, [11 ,12] can be bonded by adhesives. Secondly, adhesive bonding technology makes bonded structures light in comparison to other assembly technologies (e.g. mechanical fasteners). Thirdly, due to the characteristic of making no holes in the surface prior to bonding, stress concentration can be decreased compared to other methods such as bolting and/or riveting [13–15]. However, as confirmed by current literature, the mechanical response of structural adhesives in general and that of the bonded joints, in particular, is significantly dependent on several factors such as the temperature (both high and low values) and the moisture which may limit the applicability of structural adhesives. The environmental temperature may exceed the glass transition temperature ( $T_g$ ) of the adhesive formulation entailing relevant changes in its properties, determining a transition from a hard to a rubbery behaviour, thus compromising its specific application [16]. Due to different environmental parameters experienced by the assembled structures during the use, among which the temperature values, the adhesive can be naturally subjected to a delay or increase in the curing degree. This can lead to adverse or positive changes in strength and stiffness. The speed and extent of the changes depend on the magnitude and duration of the temperatures experienced by the adhesive [17].

The temperature and moisture may also produce effects on the long-term properties of the adhesives [18]. Within this framework, several studies have been carried out on the durability of epoxy adhesives in general [20] and

bonding joints in particular, considering several environmental conditions typical of applications in various fields of engineering and with particular regard to the aeronautical, [21] automotive [20] and building sectors. [21–24] The main findings are that hygrothermal aging promotes higher decreases of the failure load and maximum failure displacement of a joint independently of the adhesive used, [19,20] while thermal shocks in the air have only a marginal effect on the joint's performance. [19]

Within this framework, in order to further encouraging the spread of bonded connections, with particular regard to the field of civil engineering where the beam-to-column is the most common connection, the scopes of the present research activity are: 1) to find the most accurate geometry for such a connection; 2) to evaluate the fracture energy (in function of the hygrothermal durability) of epoxy resins which are in general the most suitable ones for bonding each other pultruded profiles; 3) to evaluate the strength and stiffness by the approach of “testing by testing” in order to create a large database that could be useful when building predictive mechanical models; 4) to try to overcome some negative peculiarities of such a connection like the brittle failure and the not repairability .

After the “State of Art” section, devoted to the beam-to-column connections, the thesis is organized into two different parts. The first is relative to the first three points before introduced while the second one to the fourth one. More in detail, the first part is composed of four chapters: from the experimental (chapter 1) and numerical (chapter 2) study of the hygrothermal durability of epoxy resins to the experimental (chapter 3) and modeling (chapter 4) of the full scale beam-to-column adhesive connections. Finally, the second part is composed by an only one chapter relative to the presentation of an innovative hybrid (GFRP/steel) beam to column dissipative connection suitable for large pultruded structures. The latter, due to the patent request still under investigation, is strictly descriptive without graphs in support.



## State of art on the beam-to-column connection between pultruded profiles

In the early nineties, Bank et al. [25, 26] tested pultruded GFRP I-beam and column, connected by GFRP bolts, pultruded seat angles and web clips, as shown in Fig. A(a), or they strengthened the facing flange of the column in the joint region by GFRP angles, Fig. A(b), and then used the same type of connecting elements as in (a). Finally, to mitigate the failure mode initiated by the separation of the column web from the facing flange in the region of the top seat angle, they stiffened the beam and column in the connection region, by adhesively bonded GFRP tubular sections, and joined the members by FRP gusset plates and bolts as in Fig. A(c). They concluded that the design of beam-column connections in pultruded FRP members requires careful consideration of the unique local failure modes occurring either at the web-flange junction or in the web transverse to the direction of pultrusion.

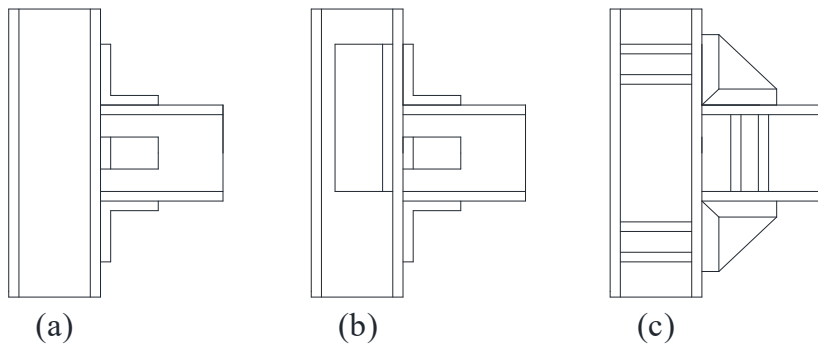


Figure A. Connections a) standard joint, b) reinforced column flange and c) gusset plate angles. [25,26]

In 1994, Mosallam [27] and Mosallam et al. [28] pointed out that it is not appropriate to design FRP frame connections using concepts developed for connections in steel structures. Instead, they developed a built-up GFRP connecting element termed “universal connector”, Fig. B, bolted to the beam and column. The typical failure mode in the latter connection was a combination of local failure in the universal connector and punching of the bolts through the column flanges. This connection increased joint strength almost threefold over the standard seat angle joint.

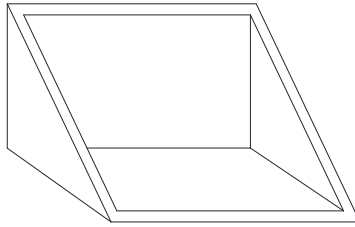


Figure B. Universal connector. [27,28]

Bank et al. [29] modified the seat angles by wrapping them with a GFRP sheet, Fig. C, and used this so-called wrapped connector to bolt the beam to the column. They indicated that, compared to other types of connections previously tested in [25] and in [26], their proposed connection yielded the best combination of strength, stiffness, failure modes and construction practicality. However, although the stiffness was much higher for this connection compared to the one in [27], [28], it should be pointed out that the failure load was almost 30% lower.

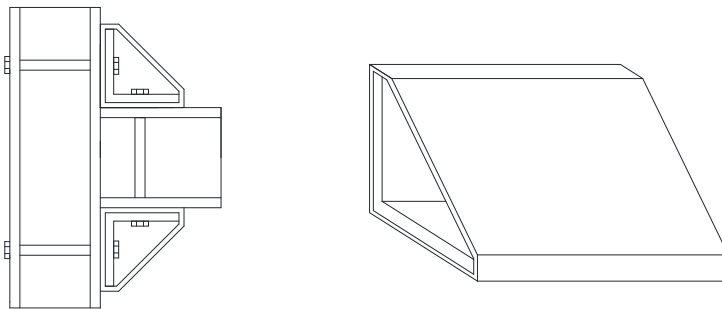


Figure C. Wrapped connection. [29]

In 1998, Smith et al. [30] presented the results of an experimental investigation on pultruded GFRP I- and box- sections. The tests comprised six specimens: three beams and columns with I-profile and three with hollow or box section. In the case of the I-section, the beam-column connection was almost identical to the one used by Bank et al. [29], but instead of GFRP bolts, steel bolts were used. In one case, the GFRP seat angles were replaced by steel angles. The box sections were joined on the top and bottom faces of the beam to the column by GFRP angles and on the sides by GFRP plates. In all cases steel bolts were used to join the elements. With respect to both strength and stiffness, the box beam connections performed much better than the I-beam connections.

In 1999, Smith et al. [31] presented the findings of an experimental investigation to demonstrate the performance of their proposed monolithic

connecting element, termed “cuff” (Fig. D). The element was used to connect GFRP box beams and columns and led to substantial increases in joint stiffness (90%) and strength (330%), compared to the earlier typical seat angle connections used to join GFRP I-beams and columns. The concept of the cuff connection is that the beam and column can fit into the hollow cuff sections, ideally requiring only epoxy to keep them in place, albeit Smith et al. used both steel bolts and adhesive to join the beam and column to the cuff.

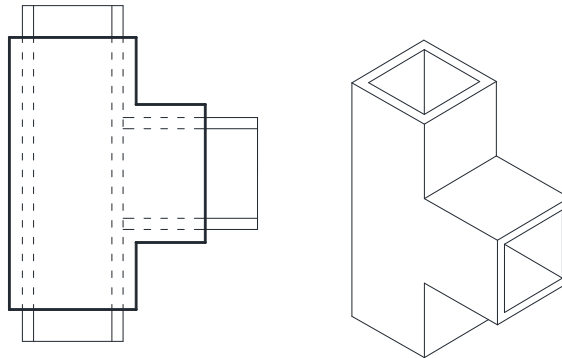


Figure D. Idealized cuff connection. [31]

In 1999, Mottram and Zheng [32,33] conducted an experimental investigation on an interior connection, involving two cantilever beams connected to a central column. They studied the stiffness and behavior of web-cleated and flange-cleated beam-to-column connections. In the former, only GFRP clips were used in conjunction with steel bolts to join the beams and the column while in the latter they used GFRP seat angles and steel bolts. They concluded that the connection satisfied the requirements of the Eurocomp design code [34], [35].

As a follow up to the latter study, Quareshi and Mottram [36,37] focused on the number and location of required steel bolts in the connection and concluded that only two bolts are required to achieve satisfactory connection performance. They also investigated the behavior and failure mode of the connection when the cleat was made of either steel or GFRP. They concluded that steel cleats lead to connection failure by the general failure of the column while with GFRP cleats failure is initiated by local delamination in the column flange above the cleats.

In 2016, Zhang et al. [38] and Wu et al. [39] investigated a new bonded sleeve connection suitable for connecting hollow GFRP profiles to steel members (Figure E). The GFRP beam was fastened to the steel column by steel bolts.

They concluded that the end plate thickness is the most influential parameter insofar as the initial stiffness and the bending capacity of the bonded sleeve are concerned.

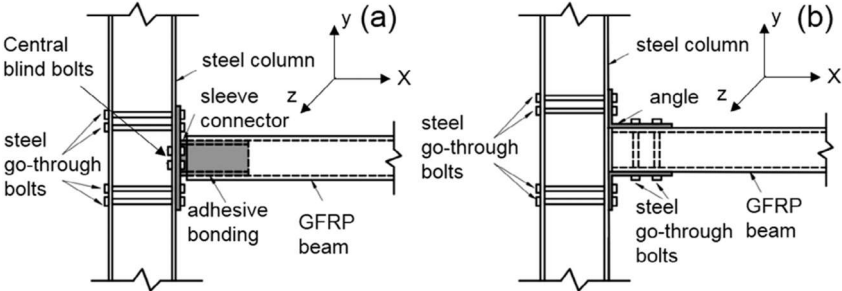


Figure E. Experimental specimens with (a) bonded sleeve connection; (b) steel angle connection. [38]

In 2017, Martins et al. [40] developed an innovative beam-to-column bolted connection system for GFRP tubes, comprising purpose-built steel connection elements to be inserted into the GFRP hollow sections (Figure F).

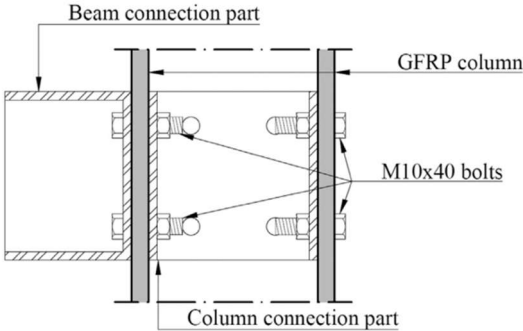


Figure F. Section view of the connection system. [40]

Four different bolt configurations were tested (Figure G), including the number and distance of the bolts from the connected beam end. They included one bolt per web (i), two bolts per flange and short end distance (ii), four bolts per flange (iii), two bolts per flange and a longer end distance (iv). They concluded that the maximum rotational stiffness was provided by the (iii) configuration while the maximum failure load by the (iv) configuration.

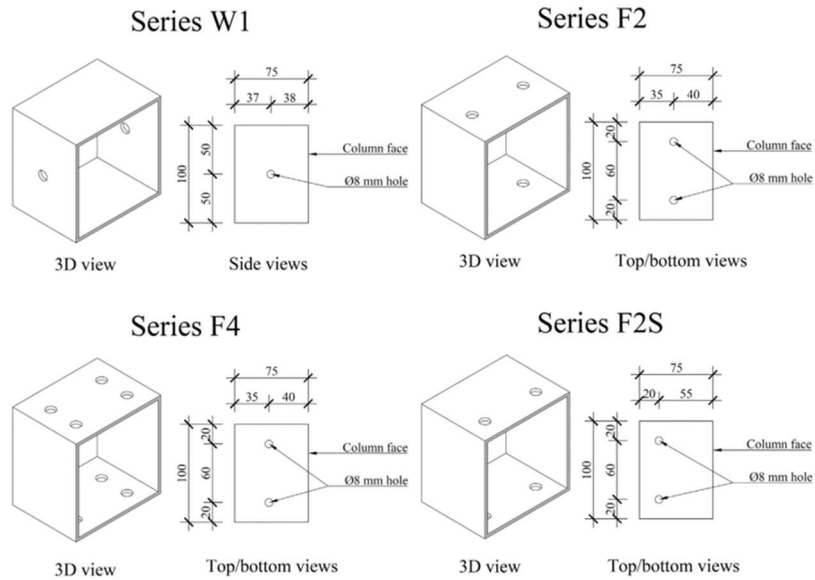


Figure G. Beam part: a) series W1; b) series F2; c) series F4; d) series F2S. [40]

In the same year, Ascione et al [41] experimentally investigated for the first time the behavior of full-scale bolt-free GFRP epoxy bonded beam-to-column moment resisting connections under static load. Both the beam and the column had I-profile with dimensions of 200x100x10 mm. Four beam-to column connection prototypes were tested. In all cases, the beam flanges and web were epoxy bonded to the column compression flange by 50x50x6mm seat angles, with 100mm length in the case of angles connecting the beam and column flanges and 170mm when connection beam web to column flange. The test parameters considered were the location of the connection with respect to the free end of the column and the column strengthening method (Figure H).

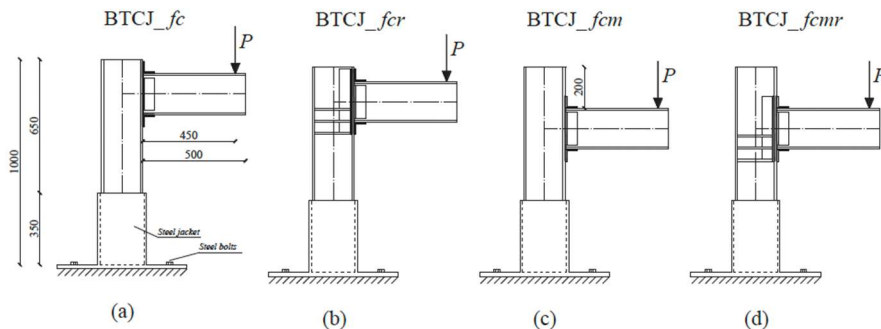


Figure H. Details of the beam-column connections tested: a) BTCJ\_fc; b) BTCJ\_fcr; c) BTCJ\_fcm; d) BTCJ\_fcmr. [41]

The connections are designated as BTCJ\_fc, BTCJ\_fcr, BTCJ\_fcm and BTCJ\_fcmr, where BTCJ stands for Beam-to-Column Junction, fc for flange connection, the letters m and r for middle and reinforced, respectively. The connections involving seat angles and column stiffeners achieved nearly the same percentage of the GFRP profile ultimate moment capacity as achieved by the best performing bolted connections previously tested by others. Furthermore, the authors declare that a key disadvantage of the adhesive connection seems to be its brittle failure mode initiated by the failure of the adhesive layer, which may render it less desirable in building structures.

Later, in 2019 Razaqpur et al. [13] present a new adhesive beam-column connection which possess the highest strength and stiffness compared to any other similar adhesive or bolted connection tested in the past. A square GFRP hollow section, acting as a column, was connected to a built-up beam made of two GFRP U-profiles by means of either epoxy or steel bolts (Figure I).



a) b)  
Figure I. Typical specimen: a) Adhesive; b) Bolted. [13]

The beam-column assembly formed an L-shaped frame which was tested by applying a point load at the beam free end while the column was fixed at its base. Five bolted and five adhesive replicate connections were subjected to quasi-static loading up to failure. Another three adhesive connections were subjected to 400, 800 or 1200 cycles of loading and unloading with the

maximum load being equal to  $0.50 P_{u,avg}$ , where  $P_{u,avg}$  is the average static strength of the replicate adhesive specimens. At the end of the cyclic loading, the latter specimens were loaded quasi-statically to failure. Finally, another two adhesive connections were subjected to fatigue type loading. They were successively subjected to at least 196 cycles of loading and unloading with the load amplitude being  $0.50 P_{u,avg}$  in the first 60 cycles,  $0.75 P_{u,avg}$  in the next 60 cycles,  $0.85 P_{u,avg}$  in the following 60 cycles and  $0.95 P_{u,avg}$  after the 180th cycle. The test results show that the proposed adhesive connection can achieve on average 82% higher strength and 380% higher rotational stiffness than the companion bolted connection.

Furthermore, the above cyclic loading has negligible effect on either the strength or the stiffness of the connection. Finally, the connection can sustain the foregoing fatigue load up to almost 180 cycles without significant damage but it will not be able to withstand the full 60 cycles of the load with  $0.95 P_{u,avg}$  amplitude.

The current results demonstrate the superior strength and stiffness of the new adhesive connection compared to a similar bolted connection.

In the same year, Russo [42] studied the mechanical behaviour of multi-bolted (MB) and high multi-bolted (HMB) connections in presence of in plane actions (Figure J).



Figure J. Multi-bolted connection [42]

The authors underline that in general the design formulas, currently available in the literature for classical FRP connections, could not be applied to this type of junction. Furthermore, in complex and MB connections, it appears that the mode of failure related to net-tension and cleavage are excluded in favor of a dominant interaction between bearing and shear-out, that acquire a feature of chain/combination mode of failure developed by vertical and horizontal bolt's lines in function of the load orientation.

Always in the same year, Qiu et al [43] present experimental and numerical investigations of the bending performance of innovative splice connections developed for tubular section FRP members. Each of the splice connections consists of a steel bolted flange joint between two tubular steel-FRP bonded sleeve joints (Figure K).

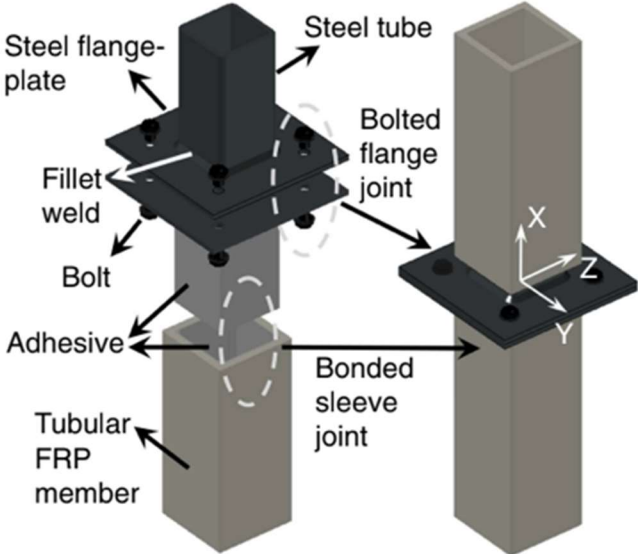


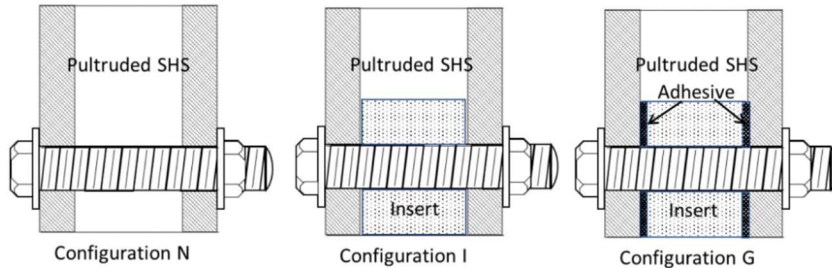
Figure K. Bonded sleeve connection for tubular profiles [43]

The authors declare that all of the connection specimens exhibit excellent ductility through yielding of the steel flange-plate before ultimate failure.

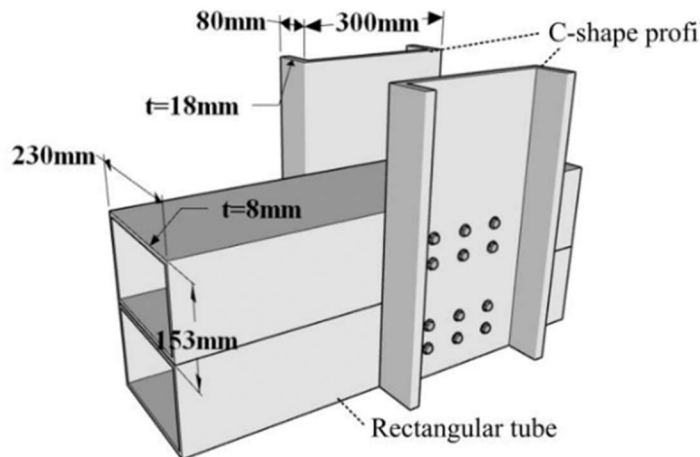
In 2020, Hizam et al. [44] present a study of the effect of elevated temperatures and mechanical inserts on the joint strength and failure mechanism of a square hollow section (SHS) of pultruded glass FRP (GFRP) composites.

Three pultruded GFRP bolted joint configurations were implemented (see Figure L): a joint without mechanical insert (N), a joint with mechanical insert with tight-fit attachment (I), and a joint with mechanical insert bonded with epoxy adhesive (G). Sixty (60) square pultruded GFRPs with a single all-

threaded bolt connection each were tested up to failure at room temperature 40°C, 60°C, and 80°C. Specimen G exhibited the highest joint strength, with twice more than that of Specimen N across the temperature range. Specimens N and I failed by shear-out at high temperatures mainly due to the deterioration of the interfacial bond between the fibers and the matrix.



In chronological order the last research developed was that one by Peng et al [45] in 2021 where the flexural behavior of an adhesive-bolt hybrid connection for pultruded glass fiber reinforced polymer (GFRP) frame is investigated through monotonic and cyclic loading tests (Figure M).



The authors declare that the hybrid connection fabricated using resin adhesive and steel bolts is able to exhibit a quasi-plastic behavior. Multistage damage occurred in tests, and the adhesive failed initially, followed by GFRP failure at bolt holes.



## **PART I: The mechanical behaviour of a full adhesive beam-to-column connection**

Object of this Part I of the thesis is the study of the global behaviour of a full adhesive beam-to-column connection from both an experimental and mechanical point of view. More in details, the role played by the hygro-thermal aging, by the bonded area extension and by the load condition is investigated. For what concerns the study of the aging influence, a wide preliminary experimental study about the durability of epoxy resins, suitable for bonding pultruded profiles each other, is presented (Chapter 1). This topic was developed in collaboration with Professor Liberata Guadagno and Dr. Carlo Naddeo of the Industrial Department of the University of Salerno. Furthermore, the experimental investigation related to the global mechanical behaviour of the full scale beam-to-column adhesive connections presented in the Chapter 3 was developed in collaboration with Dr. Giulia Carozzi of the TopGlass Industries.



# CHAPTER I: Hygrothermal durability of epoxy adhesives used in civil structural applications: an experimental investigation

## 1. Introduction and a brief *State of Art* on the durability of epoxy resins and GFRP material

The topic of the present chapter is the study of the hygro-thermal durability of two commercial epoxy resins, suitable for civil engineering applications, respect to the immersion in tap water and sea water for a period of fifteen months at the temperature of 30°C. To this scope a wide experimental program was developed comprising both End Notch Failure (ENF) tests on the adhesive samples (adherent in glass fiber reinforced polymer, GFRP) for evaluating the pure fracture energy in Mode II of the resins and the water absorption and desorption tests for resins and GFRP materials.

Parallel to the experimental program, analytical simulations, based on the application of the Fick's law, were developed in order to simulate the water uptakes experimentally observed.

### *State of art on the durability of epoxy resins and GFRP material*

The excellent performance of the pultruded profiles in terms of corrosion resistance as well known in literature [46-58] was the reason why the beam-to-column connection, in this thesis presented, was studied taking into account a long immersion period in sea water and tap water, as better described in the next. In these previous studies, the main results obtained are summarized in the following. (1) Prolonged exposure to seawater at 30°C causes degradation in flexural strength and modulus [50, 51] of glass-polyester and glass/vinylester composites which are among the materials proposed for use in marine application. (2) Seawater can cause swelling and plasticization of the matrix and debonding at fiber/matrix interface leading to reduction in mechanical properties [50-53].

(3) Absorption of seawater and/or distilled water is responsible for variations in mechanical, chemical and thermo-physical properties of the adhesive due to hydrolysis or plasticization effects [46-49]. (4) Damage entity and decrease in mechanical performance is related to the temperature and nature (ionic activity or unitary activity of the pure water) of the fluid where the joint is immersed.

Plasticization and swelling usually cause relaxation phenomena of curing stresses, hence partially compensating possible interfacial degradations due to the moisture. An increase in the temperature during the immersion in water determines an increase in moisture absorption and as a direct consequence a decrease in ductility, tensile strength and in interfacial adhesion of glass/epoxy composites [53-54].

More in detail, (5) the mechanical properties of the GFRP materials decrease by about 8% for an immersion time of ninety months in seawater at a temperature of 23°C and about 50% at 65°C [53]. (6) High temperature can be used as an acceleration agent in time-temperature-superposition models to predict long-term effects from accelerated short-term tests [53].

### 1.1. Experimental program and scope

The main scopes of this experimental program here presented and discussed are to study the hygro-thermal durability in terms of fracture energy in pure mode II of two commercial epoxy resins (SikaDur30 and Araldite), suitable for civil engineering applications, respect to the immersion in Tap Water (TW) and Sea Water (SW) for a period of fifteen months at the temperature of 30°C and their absorption and desorption behaviour. The temperature was selected for two reasons: in the specific case of the sea water it represents the most severe environmental condition while for both conditioning it accelerates the diffusion and promotes the degradation mechanisms [53].

Within this scope one hundred and sixty-two single lap joints (SLJ) and six resin samples (three per each adhesive) were fabricated as described in the subsection 1.1.3. The laboratory test adopted to evaluate the toughness in mode II is the End Notch Failure (ENF) as discussed in detail in the next subsection 1.1.5.

The SLJ specimens were divided into four groups: the first group comprises the twelve unaged samples of Table 1 which were tested to evaluate the initial fracture energy (time zero); the second group (the main one) comprises the one hundred and thirty-eight aged specimens of Table 2 which were tested to evaluate the fracture energy relative to different immersion periods; the third group comprises the twelve specimens of Table 3 which were used firstly to evaluate the absorption behaviour of the single lap joints and consequently used for ENF tests corresponding to fifteen month of immersion in water for SikaDur30 and corresponding to twelve month of immersion in water for Araldite; finally, the fourth group comprises twelve aged specimens of Table 4 which were used to evaluate the desorption influence.

Table 1. Unaged specimen for ENF test.

Number of unaged SLJ specimens	
<i>ENF test</i>	
SikaDur 30	Araldite
6	6
<i>Total number of specimens</i>	
12	

Table 2. Aged specimen for ENF test.

Number of aged SLJ specimens				
<i>ENF test</i>				
<i>Months of immersion</i>	SikaDur30		Araldite	
	<i>Sea Water</i>	<i>Tap Water</i>	<i>Sea Water</i>	<i>Tap Water</i>
1	3	3	5	3
2	-	-	5	3
3	3	3	3	3
4	3	3	2	2
5	3	5	4	4
6	6	6	5	5
7	-	-	-	-
8	-	-	-	-
9	5	4	5	5
10	-	-	-	-
11	-	-	-	-
12	6	7	6	5
13	-	-	-	-
14	-	-	-	-
15	6	7	-	-
	<i>Partial number of specimens</i>			
	35	38	35	30
	<i>Total number of specimens</i>			
	138			

Table 3. Aged control specimen for Absorption and ENF test.

Number of aged SLJ specimens			
<i>Absorption</i>			
SikaDur30		Araldite	
<i>Sea Water</i>	<i>Tap Water</i>	<i>Sea Water</i>	<i>Tap Water</i>
3	3	3	3
<i>Total number of specimens</i>			
12			

Table 4. Total number of specimens fabricated and tested for desorption.

Aged	Araldite	
	<i>Sea Water</i>	<i>Tap Water</i>
	6	6

### 1.1.1. Materials

The adhesives investigated in this study were two bi-component paste epoxy adhesives commercially named SikaDur 30 [59] and Araldite AV 5308 (Hardener HV 5309-1) [60] produced by Sika SpA (Italy) and Huntsman Adv. Materials (Switzerland), respectively. The main technical specifications of the two different structural adhesives are shown in Table 5. As recommended by supplier's documentation the following mixing weight ratios were adopted: 1:3 for SikaDur30 and 1:1 for Araldite. The SikaDur 30 system is composed of a bisphenol A resin with a polyamine based hardener and inert fillers. The Araldite AV 5308 is composed of a mixture of epoxy resins bisphenol A/bisphenol F/butanedioldiglycidyl ether (reactive diluent) cured with a mixture of amine compounds. The commercial compositions of the two hardeners were studied to activate the curing reactions at low temperature, as deducible from the presence of aliphatic amines, including primary, secondary and tertiary amines. The components of the two different systems were mechanical-mixed at low speed of 500 rpm using a paddle mixer until uniform grey and neutral colors were achieved for the two systems. A spatula was used to check that there were no streaks near the bottom edges of the containers. The mixing was performed at room temperature. Table 5 shows some parameters provided by the suppliers. A spatula was used to check that there were no streaks near the bottom edges of the containers. The mixing was performed at Room Temperature (RT,  $23 \pm 2^\circ\text{C}$ ).

The adherents are made of E-glass G967P reinforcement, with a volume fraction of 60%, whereas the remaining volume is made of an isophalic polyester P4506 Firereta matrix. The colour is light grey RAL 7035 with a veil surface. The modulus of elasticity of the plates along the fiber direction is equal to 24 GPa, while the shear modulus is equal to 3 GPa [61].

Table 5. Mechanical parameters of the adhesives at 23°C (epoxy resins).

Resin	Colour	Density [g/cm <sup>3</sup> ]	T <sub>g</sub> [°C]	Tensile Strength [MPa]	Shear Strength [MPa]	Tensile Modulus [GPa]
SikaDur30 [59]	Base A component -White Hardener – Mid Grey	1.65	52	26 – 30	16	11
Araldite [60]	Base A component -White Hardener – Mid Grey	1.40	67	30	9	2

SikaDur30 was cured at 23°C for 7 days and Araldite was cured at 23°C for 1 days.

### 1.1.2. Thermal Analysis

#### *Differential Scanning Calorimetry (DSC) and Thermogravimetric analysis (TGA)*

A key parameter in the set of tests for the characterization of adhesive joints is the evaluation of the Glass Transition Temperature ( $T_g$ ). When adhesively bonded joints are tested below this temperature, the adhesive behaves like a low-strain rigid material, while above this temperature it has a more rubber-like behavior.

The glass transition temperature ( $T_g$ ) of two epoxy adhesives has been evaluated by thermal analysis performed with the differential scanning calorimeter Mettler DSC 822 operating under nitrogen flow. The samples were analyzed by a three-step dynamic heating program in the temperature range between -50°C and 350°C considering a first step from -50°C to 280°C with a scan rate of 10°C min<sup>-1</sup>, a second cooling step from 280°C to -50°C with a scan rate of 50°C min<sup>-1</sup> and a third step from -50°C to 350°C with a scan rate of 10°C min<sup>-1</sup>. The use of such a dynamic heating program allows detecting both the characteristic thermal transitions and also the Curing Degree (C.D.) of the two different epoxy adhesives. Calorimetric data have been used for the estimation of the C.D. of the samples under the assumption that the exothermic heat evolved during cure is proportional to the extent of reaction. The C.D. was determined from the total heat of reaction ( $\Delta H_{Rtot}$ ) of the first run curing reaction and the residual heat of reaction ( $\Delta H_{Rres}$ ) of the partially cured epoxy resin as follows Eqn. (1):

$$C. D. = \frac{\Delta H_{R_{tot}} - \Delta H_{R_{res}}}{\Delta H_{R_{tot}}} \cdot 100 \quad (1)$$

Thermogravimetric analysis (TGA) was carried out using a Mettler TGA/SDTA 851 thermobalance. The samples were heated from 0°C to 800°C at a 10°C/min heating rate under both nitrogen and air flows. The weight loss was recorded as a function of temperature and the results were used to evaluate the gravimetric consumption and the temperature of thermos-degradation ( $T_g$ ) of the two structural adhesives in different reactive environments (air and nitrogen).

### 1.1.3. Specimen fabrication

#### *Differential Scanning Calorimetry (DSC) specimen*

The specimens for the DSC and TGA investigation were manufactured according to EN ISO 62:2008 [62]. Their dimensions are 40 mm long, 10 wide and 1 mm thick. Bulk specimens were prepared as follows: (1) the two components, including the epoxy resin and curing agent, were mixed as described in the previous section; (2) each mixture was poured into the rubber molds for 24h under controlled environment at  $23 \pm 2$  °C (Figure 1); (3) after 24h the specimens were removed from the molds and cured at the following condition: seven days for SikaDur30 [59] while those with Araldite [60] for 24 hours at the room temperature equal to  $23 \pm 2$  °C. Concerning the temperature of the curing stage, the room temperature has been chosen to simulate as much as possible the conditions of real employment. Parts of these specimens were removed away by using a scraper to perform the thermal investigation.

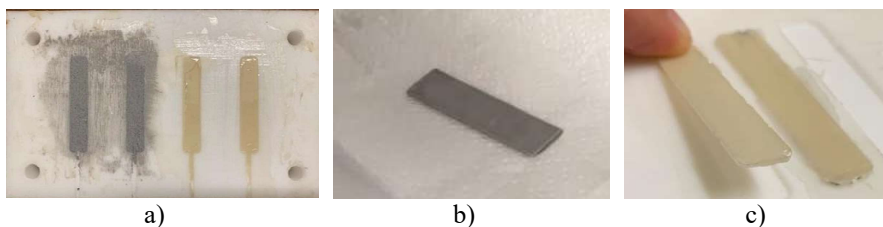


Figure 1. Specimen fabrication: a) Teflon mold; b) DSC specimen SikaDur30; c) DSC specimen Araldite.

### Single Lap Joint (SLJ) specimen

In order to evaluate the fracture energy in Mode II, the End Notch Failure Test (ENF), considered in the literature the most suitable characterization test [63], was adopted.

The SLJ pieces, suitable for the ENF test, consist of two GFRP plates bonded with the two structural epoxy adhesives before introduced. GFRP plates were 10 mm thick ( $t$ ), 25 mm wide ( $b$ ) and 340 mm long ( $L_s$ ) as depicted in Figure 2a. The Young Modulus of the plates along the fiber direction and that one in transversal direction are equal to 30 GPa and 7 GPa, respectively, while the shear modulus was equal to 3 GPa.

Before bonding, surfaces were grit blasted and degreased with acetone prior to the application of the adhesive. Being the joint symmetric, a pure mode II characterization is expected [63]. The bondline thickness was nominally 1.0 mm. Spacers (calibrated steel bars of 1.0 mm) were inserted between the adherents before the application of the adhesive in order to control the bondline thickness.

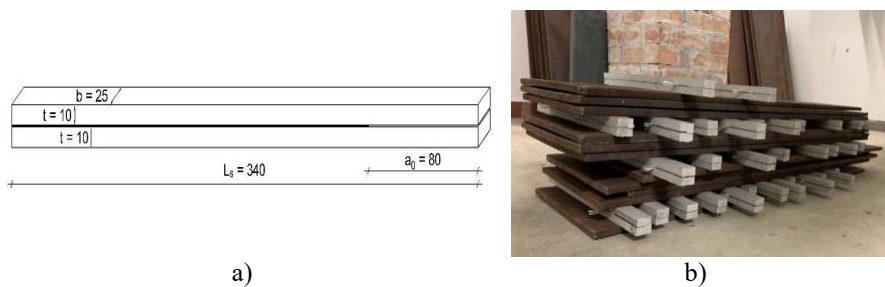


Figure 2. SLJ specimens: a) geometry; b) curing phase.

A pre-crack 80 mm long ( $a_0$ ) in the adhesive layer (Figure 2a) was assured in order to have a stable crack growth as reported in [64]. The pre-crack was realized inserting a squared sheet of polystyrene between the adherents before bonding. In fact, the authors in [64, 65] suggested to this scope to adopt an initial crack larger than a critical value equal to  $0.35 2L$  ( $2L$  is the span of Figure 5a). The SLJ specimens were produced at room temperature of  $21 \pm 2^\circ\text{C}$ . After having checked the alignment between the adherents, the specimens were cured for 24h as depicted in Figure 2b. After 24h, the specimens were removed from the steel frame and cured at the same condition of resins: for seven days the SLJ specimens with SikaDur 30 and for twenty-four hours those with Araldite according to the RT above cited as reported in their technical data sheets.

### 1.1.4. Hygro-thermal conditioning

The experimental apparatus shown in Figures 3 was used for conditioning. It consists of a two separate plastic boxes containing Sea Water (SW) and Tap Water (TW) as depicted in Figure 3a, respectively, both at a constant temperature of about 30°C served by the immersion heater of Figure 3b. The salinity, the temperature and the pH of the seawater were continuously recorded by a redoximeter HI9829 (Figure 3c) and their distributions over the time are depicted in Figure 4. For the sake of clarity, oscillations of temperature and salinity are justified by the need for adding cold water in order to maintain the salinity in the range 36-39 PSU (typical values) due to the evaporation phenomenon. Regarding the tap water, it was continuously monitored the temperature (average value of 27.95 °C) and the pH (average value of 7.72).

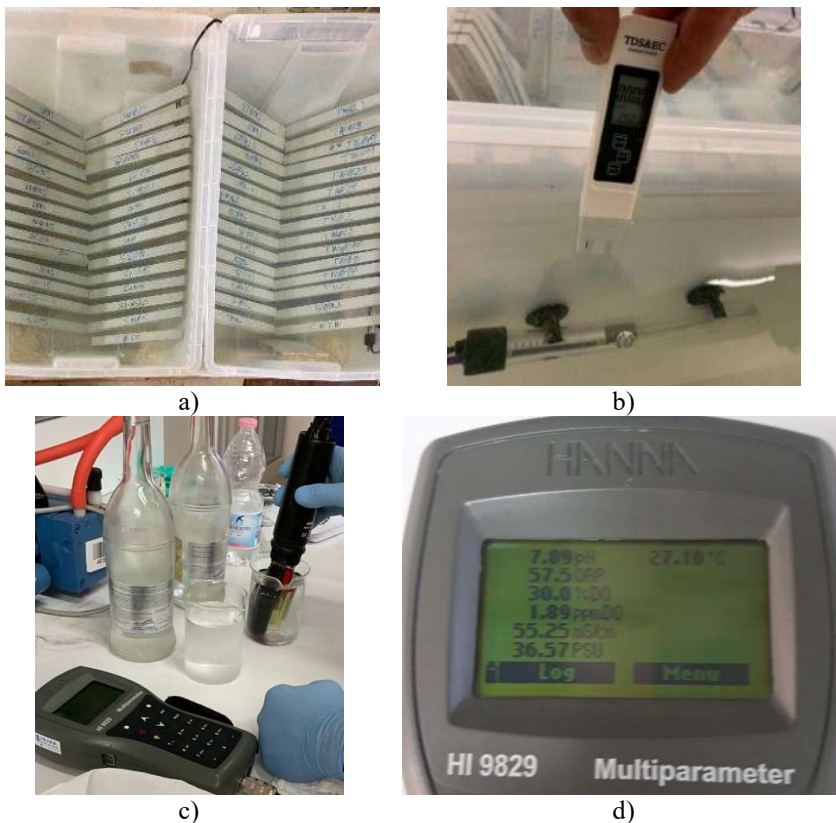


Figure 3. Photos of the environmental exposure set-up: a) plastic boxes for SLJ specimens; b) immersion heater and thermometer; c) redoximeter. d) values measurement redoximeter.

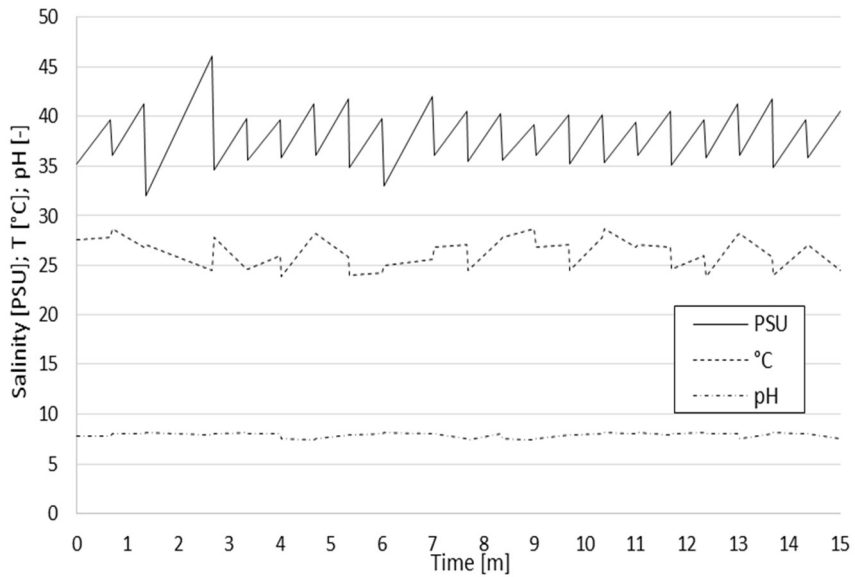


Figure 4. Sea water parameters. Graphs of the salinity, the temperature and the pH vs time.

### 1.1.5. ENF test procedure

A schematic representation of the ENF test is shown in Figure 5a. The End Notch Failure Test (ENF) [66], considered by current standards [24] as the reference test, was adopted to evaluate the fracture energy in mode II. The evaluation of fracture data is based on global force-displacement measurements. The sample was loaded with a force,  $P$ , normal to the bondline, applied at the mid-span position, in displacement control at a rate of 0.25 mm/minute.

Vertical displacement was measured by one transducer sensor placed under the specimen at the same cross section where the load was applied (Figure 5b). The distance between the supports (span  $2L$ ) was 300 mm. The joint was loaded continuously until the stable propagation of the fracture was observed.

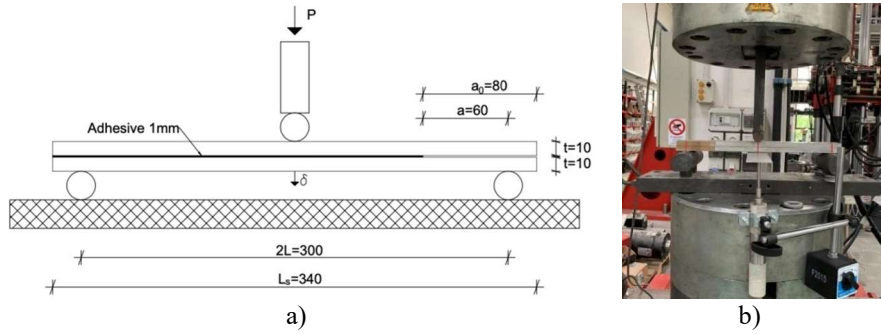


Figure 5. ENF test procedure: a) Geometry of the ENF tests for the adhesive layer characterization (dimensions in mm); b) Photo of the SLJ specimen and LVDT.

### 1.1.6. Compliance-Based Beam Method for evaluating $G_{II}$

For the evaluation of fracture energy in mode II ( $G_{II}$ ) the *Compliance-Based Beam Method* (CBBM) presented in [64] was adopted. This method is based on the crack equivalent concept, depending only on the specimen compliance during the test and not on the mechanical properties of GFRP (difficult to characterize considering the conditioning for fifteen months). Furthermore, the method here adopted doesn't require the crack length monitoring during crack growth which was observed to be very difficult to perform with accuracy in the ENF test [64, 65]. In addition, the equivalent crack length,  $a_{eq}$ , accounts for the Fracture Process Zone (FPZ) effects at the crack tip, which are not taken into account when the real crack length is considered.

In order to better understand the main features of the model as mentioned before, it is worth to remember that the CBBM is derived by the original *Direct Beam Theory* (DBT) and *Corrected Beam Theory* (CBT). In CBT, respect to DBT, a transverse shear factor in the expression of the fracture energy in mode II as below reported is presented:

$$G_{II}^{CBT} = \frac{9 P^2 a^2}{16 B^2 E_L h^3} f_v \quad (2)$$

where  $E_L$  is the longitudinal modulus,  $a$  is the crack length,  $f_v$  is a transverse shear factor,  $P$  is the applied load,  $B$  is the specimen width and  $h$  is the adherent thickness. The toughness  $G_{II}^{CBT}$  of Eqn. (2) is dependent on both the crack length measurement during propagation and the longitudinal Young modulus of the adherents. In addition, by adopting CBT it isn't possible to consider the FPZ effects which are quite large as demonstrated in [66]. To overcome these

difficulties in [67, 68] was proposed a *Corrected Beam Theory with Effective Crack Length* (CBTE) where shear effects were introduced in the specimen compliance. The following specimen compliance firstly introduced in [69] could be adopted:

$$C = \frac{2 L^3 + 3 a_e^3}{8 B E_L h^3} + \frac{3 L}{10 G_{13} B h} \quad (3)$$

where  $G_{13}$  is the shear modulus of the adherents and  $a_e$  is the equivalent crack length, which, during crack growth, includes the effect of the FPZ. By Eqn. (3), if the elastic properties are known, the equivalent crack length can be easily obtained from the measured compliance  $C$  as follows:

$$a_e = \sqrt[3]{\frac{8 E_L B h^3 C_c - \frac{2 L^3}{3}}{3}} \quad (4)$$

In Eqn. (4)  $C_c$  assumes the following meanings:

$$C_c = C - \frac{3 L}{10 G_{13} B h} \quad (5)$$

By substituting Eqn. (4) into Eqn. (1) it is possible to obtain a new version of the toughness in mode II that requires to only know the elastic longitudinal modulus.

$$G_{II}^{CBT} = \frac{9 P^2 a_e^2}{16 B^2 E_L h^3} \quad (6)$$

Finally, to avoid the preliminary knowledge of the elastic property above mentioned, in [70] the Eqn. (3) was modified by introducing the measured initial compliance  $C_0$  and the initial crack length  $a_0$  as follows:

$$C_0 = \frac{2 L^3 + 3 a_0^3}{8 B E_{app} h^3} + \frac{3 L}{10 G_{13} B h} \quad (7)$$

From Eqn. (7) it is easy to obtain the apparent longitudinal modulus which assumes the following expression:

$$E_{app} = \frac{2 L^3 + 3 a_0^3}{8 B C_{c0} h^3} \quad (8)$$

being

$$C_{c0} = C_0 - \frac{3 L}{10 G_{13} B h} \quad (9)$$

Using into Eqn. (3) the apparent modulus,  $E_{app}$ , instead of the measured one,  $E_L$ , the following expression of the equivalent crack length could be obtained:

$$a_e = \sqrt[3]{\frac{c_c}{c_{c0}} a_0^3 + \frac{2}{3} L^3 \left( \frac{c_c}{c_{c0}} - 1 \right)} \quad (10)$$

By introducing the Eqn. (8) and (10) into Eqn. (6) the final expression of the fracture energy in mode II is:

$$G_{II}^{CBBM} = \frac{9 P^2 C_{c0} a_e^{\frac{2}{3}}}{2 B (3 a_0^3 + 2 L^3)} \quad (11)$$

In conclusion, the fracture energy in mode II according to CBBM only requires the knowledge of shear modulus  $G_{13}$ . Considering its small effect on the results, a typical value of the shear modulus can be used. In detail, in the current investigation the value of the shear modulus used was that one reported in [71].

### 1.1.7. ENF data analysis

Representative experimental P- $\delta$  curves of the ENF specimens for both epoxy resins used are reported in Figure 6. The load increases until the crack initiation process is completed. After that, the crack tip starts propagating. A continuous drop in the force is seen as the crack continuously propagates until the crack reaches the middle of the ENF specimen (at the time the crack approaches the loading cylinder, the load starts to increase due to the compression near the crack tip, which obstruct propagation because of friction effects). From Figure 6 it can be seen that the behavior between SikaDur 30 and Araldite is quite different. In the first case, the adhesive shows a linear elastic behavior up to failure followed by a vertical drop (brittle failure) while in the second case the

presence of a plastic zone leads to a ductile behavior. Three different values of the load  $P$  are indicated in Figure 6:  $P_{nl}$ ,  $P_{max}$  and  $P_u$ . The load  $P_{nl}$  corresponds to the loss of linearity (nl stands for non-linear) in the  $P$ - $\delta$  curve and it defines the end of the elastic zone,  $P_{max}$  is the maximum value of the applied load  $P$  and it defines the end of the post-elastic zone, while  $P_u$  is the ultimate value of the load  $P$  corresponding to the stop of the crack evolution (crack moves from an unstable state to stable one, the load restarts to increase) and it defines the end of the fracture propagation zone. In the first case, the SLJ shows a linear elastic behaviour up to failure followed by a vertical drop (brittle failure), while in the second case the presence of a post-elastic zone leads to a ductile behaviour.

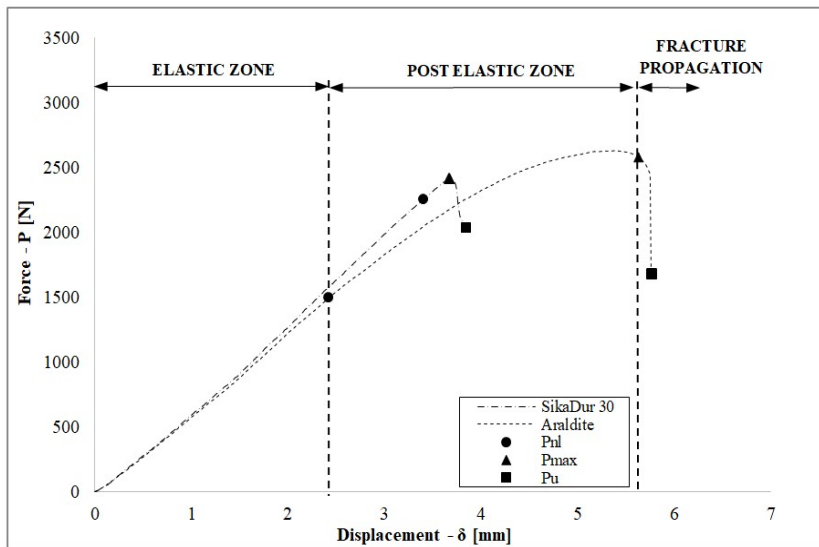


Figure 6. Representative experimental  $P$ - $\delta$  curves of SLJ specimens with SikaDur 30 and Araldite.

The critical fracture energy value in mode II was estimated using the CBBM method presented in the previous subsection. Representative experimental R-curves for SLJ specimens are presented in Figure 7, where the ductile behaviour of Araldite in relation to the brittle behaviour of SikaDur 30 can be easily observed again. The R-curve for Araldite rises rapidly in the initial stages of equivalent crack growth and gradually reaches the steady state (a stable plateau region). While, for SikaDur 30, the brittle behaviour is represented by a steady state close to the initial stages of the equivalent crack growth (absence of post-elastic zone).

In Figure 7, three different values of the fracture energy in mode II were evaluated for each SLJ specimen:  $G_{II,P_{nl}}$ ,  $G_{II,P_{max}}$  and  $G_{II,P_u}$ . They are strictly connected to the three values of the load P of Figure 6. In detail,  $G_{II,P_{nl}}$  is the fracture energy corresponding to the load  $P_{nl}$  (in this case no Fracture Portion Zone FPZ is taken into account and then the equivalent crack length,  $a_e$ , coincides with the initial crack,  $a$ , equal to 60mm);  $G_{II,P_{max}}$  is the fracture energy corresponding to load  $P_{max}$  (the whole post-elastic zone is taken into account and  $a_e$  is greater than  $a$ );  $G_{II,P_u}$  is the maximum fracture energy relative to the load  $P_u$  corresponding to the stop of the crack evolution (crack moves from an unstable state to stable one, the load restarts to increase).

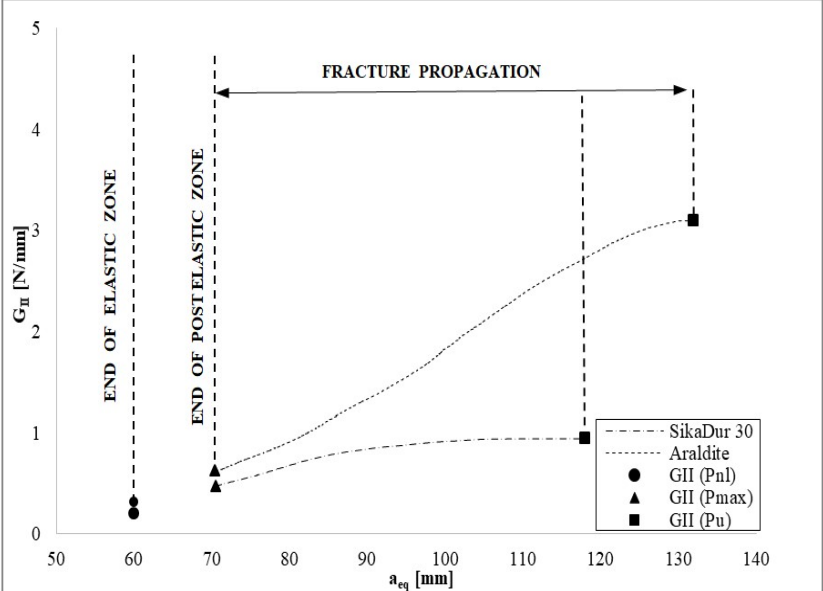


Figure 7. Representative experimental R-curves of SLJ specimens for both epoxy resins

## 1.2. Results and discussion

In this section all experimental results obtained are described and discussed, in terms of the fracture energy in mode II as well as of the strength and stiffness of the two resins under investigation. In particular, in subsection 1.2.1 the results about adhesives in terms of glass transition temperature and curing degree are reported, in subsection 1.2.2 the water absorption behaviour of adhesives and of GFRP samples is described, in subsection 1.2.3 the water

desorption behaviour of GFRP samples is described, in subsection 1.2.4 it is shown how the absorption behaviour is predictable by using the Fick's law. In subsection 1.2.5 the variability of the fracture energy over the time is reported. Finally, in subsections 1.2.6 and 1.2.7 further results about the influence on the strength and stiffness of GFRP samples of the absorption and desorption phenomenon are presented and discussed, respectively.

### 1.2.1. Thermal investigation of epoxy adhesives

DSC analysis is usually used to determine glass transition temperatures before and after curing, as well as the temperature and reaction enthalpy during the curing of the mixture.

Figures 8a and 8b show the DSC curves of the two epoxy adhesives before the curing reactions, so just after the mixing procedure. As described in the section 1.1.1 the fresh mixture (before the curing) were analysed in dynamic regime by a three-step heating/cooling program: a) a first step from  $-50^{\circ}\text{C}$  to  $280^{\circ}\text{C}$  with a scan rate of  $10^{\circ}\text{C min}^{-1}$  (First heating run – RUN 1), b) a second cooling step from  $280^{\circ}\text{C}$  to  $-50^{\circ}\text{C}$  with a scan rate of  $50^{\circ}\text{C min}^{-1}$  (Cooling RUN) and c) a third step from  $-50^{\circ}\text{C}$  to  $350^{\circ}\text{C}$  with a scan rate of  $10^{\circ}\text{C min}^{-1}$  (Second heating run – RUN 2). The continuous line corresponds to the DSC curve of the first heating dynamic run (RUN 1) (step from  $-50^{\circ}\text{C}$  to  $280^{\circ}\text{C}$ ) whereas the dotted line corresponds to the second heating dynamic run (RUN 2).

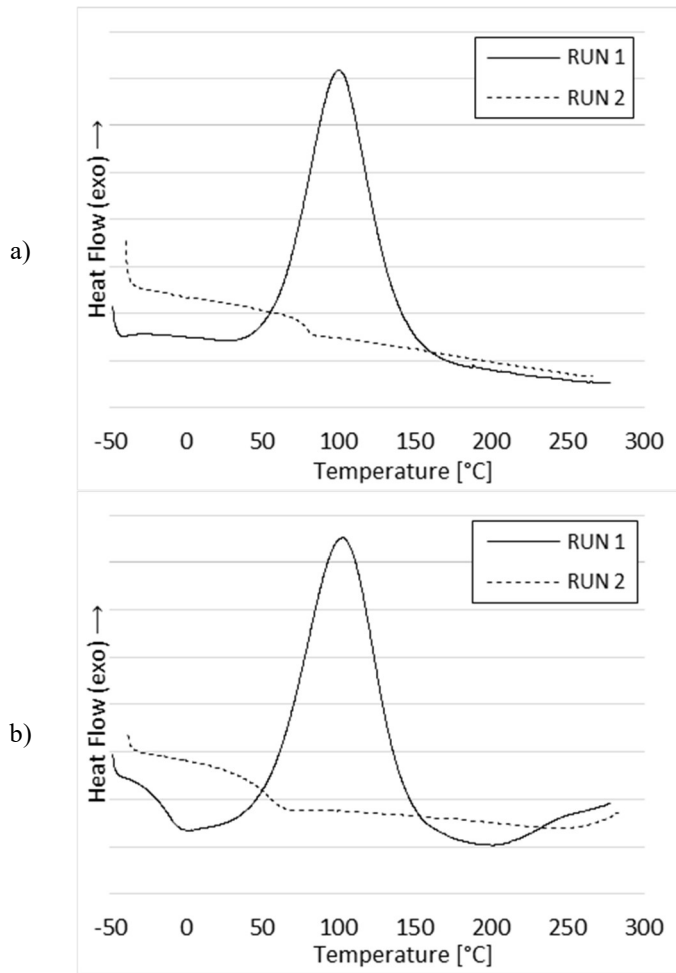


Figure 8. Heat flux vs. temperature in the temperature range between -50 and 300 °C of the fresh Systems: a) Sikadur 30 based system; b) Araldite based system.

Both systems, during RUN 1, undergo a curing process in the planned dynamic regime, as deducible from the presence of the broad exothermic peak between 30°C and 200°C for the Sikadur based-system and 0°C and 200°C for the Araldite based-system. From these different intervals, it is possible to deduce relevant information. The curing reactions in the Araldite based-system system activate (in dynamic regime) already starting from the very low temperature of 0°C. The absence of the exothermic peak in the dotted curves of the two systems indicates that the two systems are completely cured after the first RUN (RUN 1). This occurrence allows determining with a good approximation the value of the total heat of reaction ( $\Delta H_{R_{tot}}$ ) and therefore through Eqn.1 the

evaluation of the curing degree of the samples isothermally cured. The values of  $\Delta H_{R_{tot}}$  are 93.02 J/g and 110.15 J/g for SikaDur 30 and Araldite systems respectively.

Figure 9 shows the DSC curves of the two epoxy systems isothermally cured at Room Temperature (RT), with values ranging between 23°C and 25°C, for seven days for the SikaDur30 based-system and 1 day for the Araldite based-system (as described in the section 1.1.1.). Also for the samples isothermally cured, the three-step heating/cooling program before introduced has been performed.

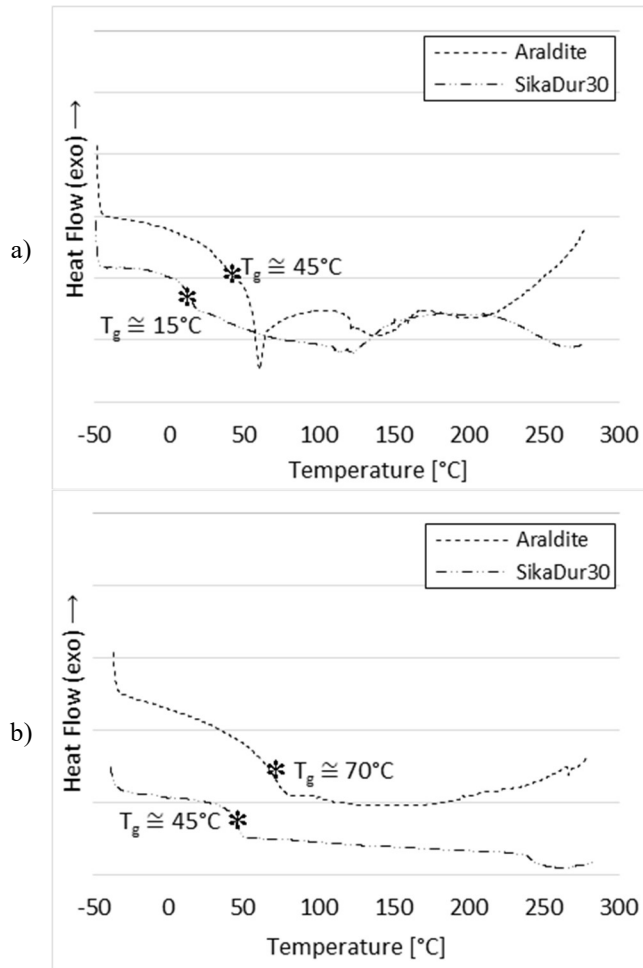


Figure 9. Heat flux vs. temperature in the temperature range between -50 and 300 °C of the isothermally cured systems: a) 1 RUN; b) 2 RUN.

In the first Run, the thermal traces of Figure 9 show a second-order phase transition, which identifies the glass transition temperature ( $T_g$ ) value of the samples after the planned curing stage. In particular, the SikaDur 30 system manifests a value of  $T_g$  around 15 °C, whereas the Araldite a higher value of about 45 °C. In this last case, an endothermic peak is manifested at the glass transition temperature ( $T_g$  endo). This phenomenon can manifest for samples cured at a temperature below the maximum value of  $T_g$  achievable for the sample (the sample was cured at 23°C for 1 day, whereas the maximum value of  $T_g$  is 70 °C - see Figure 9b). It is due to a phenomenon of thermal hysteresis determined by the fact that the relaxation rate of the molecular segments (vitrified at room temperature) is too slow to allow the material to reach the equilibrium state during the heating until the glass transition is reached.

It is worth noting that both systems show traces (see Figure 9a) typical of resin only partially cured. In fact, the trace of the Sikadur system manifests a broad exothermic peak between 120°C and 270°C, indicating additional curing reactions in the sample isothermally cured for 7 days. Similar behaviour is observed for the Araldite based-system, which manifests a more reduced exothermic peak between 140°C and 210°C.

The absence of the exothermic peaks in the curves of Figure 9b allows evaluating the C.D. of the two samples isothermally cured at 23 °C.

Applying Eqn. (1), the C.D. of the Sikadur system results in a percentage of 82%, whereas that of the Araldite 97%. It is worth noting that for the two analysed systems of Figure 9a, the Araldite-based system, even if subjected to considerably shorter curing time, shows a higher  $T_g$  value (45°C compared to the value of 15° of the Sikadur system). Generally, the range of temperature corresponding to glass transition is strongly dependent on the nature of the components, level of chemical crosslinks, physical chain entanglements in the system, as well as the degree of flexibility of the polymer chains themselves. In the case of the two analysed systems, the different  $T_g$  values found for the two formulations (after the curing) are due not only to the different chemical composition but most of all to a different density of the crosslinking network, as deduced from the different values of Curing Degree (C.D.) achieved by the systems at the end of the isothermal treatment. In fact, the Araldite based-system, compared with the Sikadur, is characterized by a C.D. enhanced by about 19%.

Considering the thermograms in Figure 9a, the higher curing degree of the Araldite system determines a higher value of thermal energy to activate the mobility of the chain segments; making this system more suitable for applications where a higher value of  $T_g$  is required.

Figure 10 shows the thermogravimetric curves of the two isothermally cured epoxy adhesives. In the inert atmosphere, the Sikadur system is stable up to 330°C, while the Araldite system up to 270°C (see Figure 10a). Very similar results are also obtained in ambient air (see Figure 10b). Both systems exhibit thermal stability in a much wider temperature range than that corresponding to usual applications.

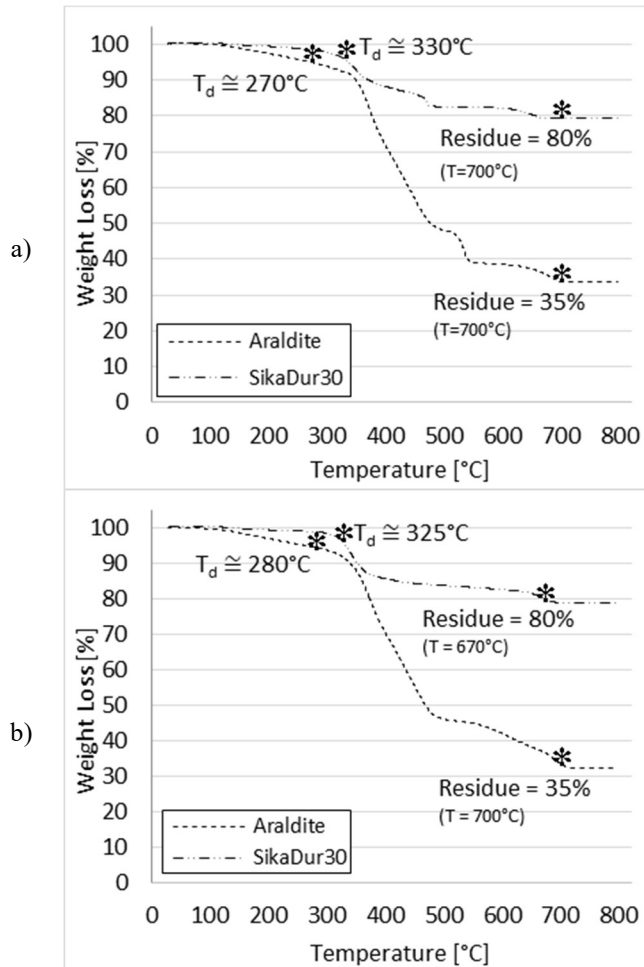


Figure 10. Thermogravimetric curves of the Araldite and Sikadur based systems: a) in nitrogen; b) in air.

### 1.2.2. Absorption behaviour

The moisture uptake content ( $M_t$ ) absorbed by each resin and/or specimen was calculated in accordance with the EN ISO 62:2008 [72] evaluating its weight before exposure ( $w_0$ ) and after exposure ( $w_t$ ) as follows:

$$M_t = 100 \left( \frac{w_t - w_0}{w_0} \right) \quad (12)$$

The elimination of moisture for the resins took place through an 96h pretreatment with vacuum at 100°C in the "P-Selecta Vaciotem-T" oven (Figure 11). The average weight loss of the specimens analyzed, following the pretreatment, was 0.45% and 4.22% for SikaDur30 and Araldite, respectively.



Figure 11. Photo of the pre-treatment stove of SLJ specimens.

Three SikaDur30 and Araldite resin specimens were immersed in both sea water (SW) and tap water (TW) by means of test tubes (Figure 12a). The tubes were immersed in a temperature-controlled system of 25°C (Figure 12b). The absorption of water by the specimens was monitored by means of a balance with precision of one hundred thousandth of a gram (Figure 12c). The evaluation of the weight variation of the specimens was monitored according to a predefined time scale: initial weight after pre-treatment in the oven, 30min, 1h, 2h, 4h, 8h, 24h, 28h, 32h, 48h, 52h, 56h, 56h, 72h, 80h, 96h, 102h, then continued at 24h intervals until the nine hundredth hour (37 days and 12 hours).

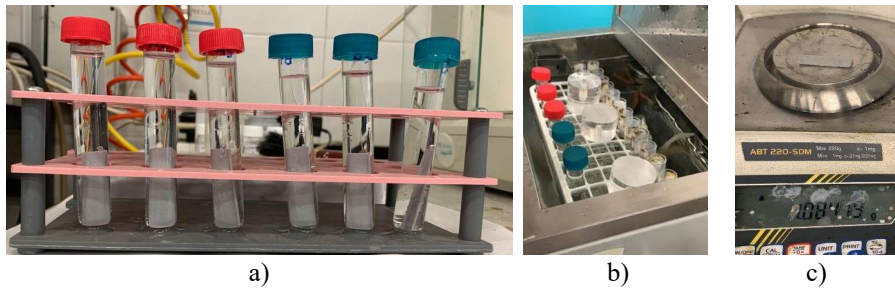


Figure 12. Resin specimens: a) specimens in test tubes; b) test tubes in cooling system; c) specimen weight control.

Water absorption in the resins is shown in Figure 13 for both types of conditioning considered. The curves reported are the average one (three samples per each adhesive were monitored). As expected, the rate of water absorption increases with immersion time showing a high incorporation rate at early stages and then continues to incorporate water at a smaller rate. In particular, TW final intakes were higher than that of SW for both resins. More in details, SikaDur 30 final intakes were 0.71% and 0.78% for SW and TW, respectively (with a difference equal to 9%). While, for Araldite the final intakes were 3.54% and 4.06% for SW and TW, respectively (with a difference equal to 15%). In general, it is possible to conclude that water intake for Araldite is 5 times bigger than that of SikaDur 30 irrespective of the type of liquid. All the data measured during the current experimental investigation are in Appendix A (Table 35 for resins Araldite and Table 36 for resins SikaDur30).

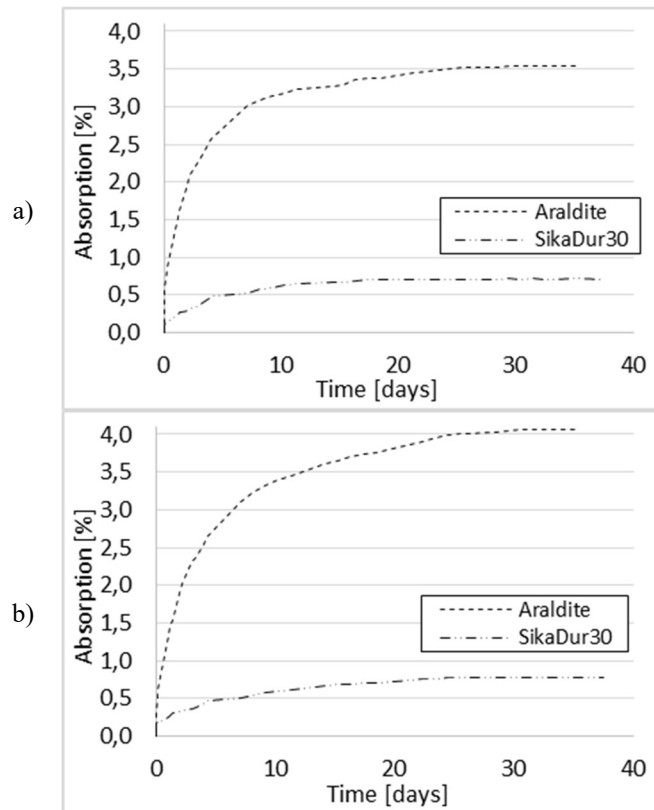


Figure 13. Water uptake curves for epoxy resins, a) sea water, b) tap water.

The percentage weight loss was 0.22% for the SLJs with SikaDur30 and 0.33% for the SLJs with Araldite following the pretreatment. Given that the conditioning of both the SLJs and the adherents took place in rooms other than those in which the material was pretreated to avoid conditioning of the atmosphere before immersion in water, they were placed in a box containing silica (Figure 14). The moisture was removed from the silica by pre-treating it in the oven. The absorption of water through the specimens was monitored by means of a balance with precision of one hundred hundredth of a gram. The evaluation of the weight variation of the specimens was monitored according to a predefined time scale: initial weight after pre-treatment in the oven, then continued at 24h intervals until the reaching of the horizontal asymptote, later once a week.



Figure 14. Silice used to avoid conditioning of the atmosphere.

As for the resins, in Figure 15 the water absorption of SLJ specimens and GFRP adherents is reported. Also, in this case the curves reported are the average ones (three joints per each adhesive were monitored). All data measured during experimental investigation with relative average values and standard deviations are collected in Appendix A (Table 37 for SLJs with Araldite, Table 38 for SLJs with SikaDur30 and Table 39 for only adherents). SLJs present the same final water intake irrespective of adhesive used: about 3.0% for SikaDur 30 and 3.5% for Araldite. A further important result is that Sea Water (SW) reduces drastically the intakes at early stages making longer the period of immersion to reach the final intake respect to the Tap Water (TW). Considering the results for joints with SikaDur 30, the final intake was reached for SW in five months instead of the three months for the case of TW. Some authors attributed this phenomenon to the presence of salt in aqueous solutions resulting in a lower equilibrium content, by virtue of its lower chemical activity. Another possibility is that salts that cover the surfaces of GFRP adherents obstruct the water permeation through the material. Finally, in terms of absorption of SLJs, the influence of the resin is negligible with respect to that of GFRP material.

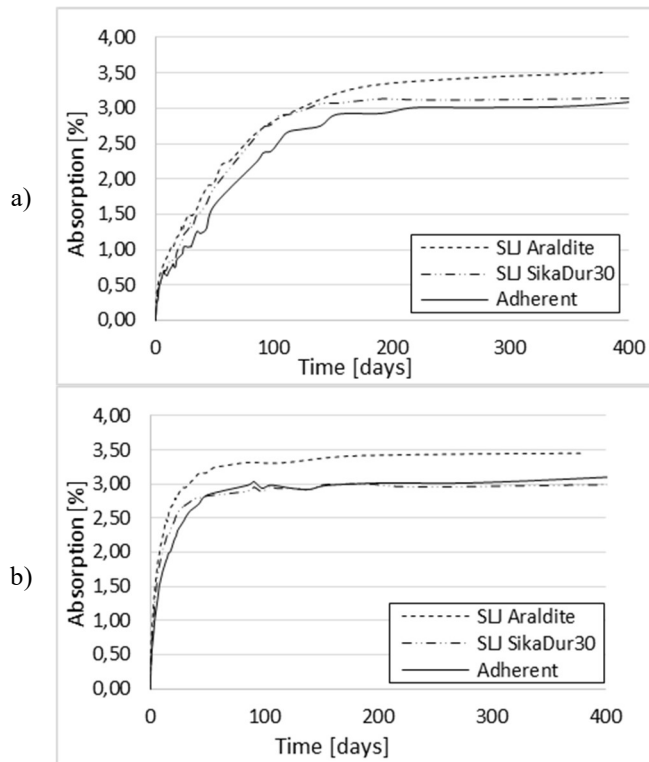


Figure 15. Water uptake curves for SLJ samples and GFRP adherent, a) sea water, b) tap water.

The uptake curves of all conditioned specimens (bulk adhesive and SLJ) show initial linear diffusion trend. The edge surfaces of GFRP adherents are protected from environmental attacks by the surface veil (MAT), which meant the moisture absorption from the edge surfaces of specimens could be neglected.

Therefore, Fick model can be used to estimate the moisture diffusion coefficient being the diffusion process into SLJ specimens essentially one-dimensional (through the thickness direction).

### 1.2.3. Desorption evaluation

In Figure 16a and 16b the absorption and desorption evaluation of the SLJ specimens with Araldite only is presented. The curves reported are the average ones (three joints per each conditioning type). All the data measured during the current experimental investigation are in Appendix C (Table 44).

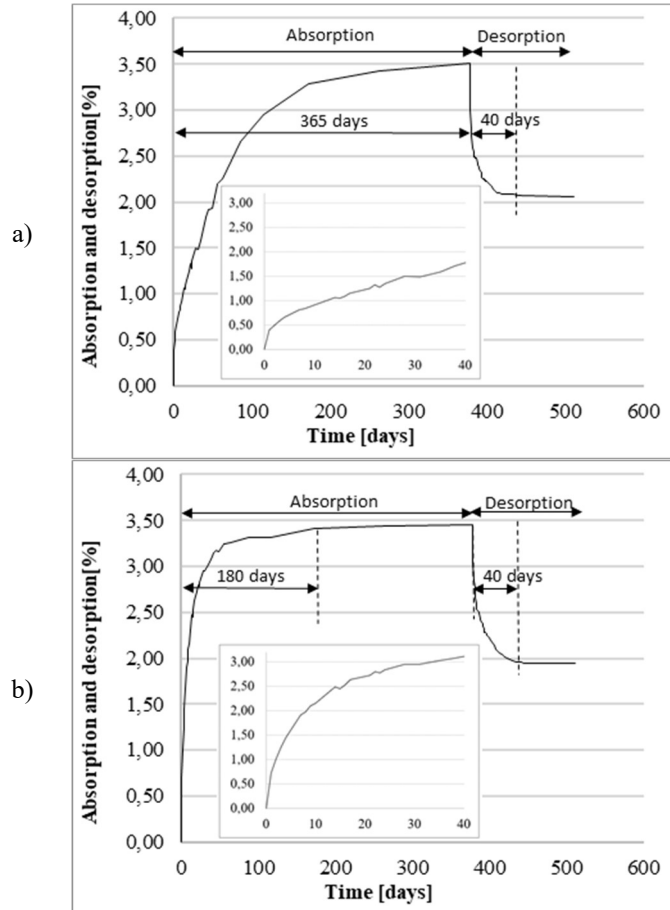


Figure 16. Absorption and desorption behaviour for SLJ samples with Araldite: a) sea water, b) tap water.

Regarding the desorption, SLJs present the same water intake (2%) at the end of the desorption period. The final intake was reached at the same time irrespective of the conditioning type (40 days).

The amount of water trapped inside the joint is an expected result given a desorption occurring at RT. To eliminate all the absorbed water, it is necessary to treat it in a stove at a temperature of about 100°C as performed on the joints before immersing them in water.

How this 2% of moisture is distributed between the GFRP adherents and the adhesive is still under investigation. As discussed in section 1.2.5, it was possible to study how this 2% affects the fracture energy as well as the stiffness and strength of the joint.

#### 1.2.4. Comparison between experimental and numerical results about absorption

A comparison between numerical results obtained by adopting the Fick model and all experimental ones obtained is presented and discussed. More in detail, the comparison was done respect to the twelve specimens of resins and SLJs (three per each resin and type of conditioning) and respect to the two GFRP adherents as summarized in Table 6.

Futhermore, the Fick model was applied to both bulk adhesive specimens and SLJ samples. According to standard EN ISO 62:2008 [72], being the SLJ samples under investigation cut from finished products and their thickness being substantial for the type of application proposed, they were tested with their original thickness. The curves of Figure 15 were obtained by considering the average values relative to the samples of Table 6.

Table 6. Specimens nomenclature.

	Resin		SLJ		Adherent	
	40x10x1 mm <sup>3</sup>		340x25x21 mm <sup>3</sup>		340x25x10 mm <sup>3</sup>	
	Tap W.	Sea W.	Tap W.	Sea W.	Tap W.	Sea W.
SikaDur30	A1,A2,A3	B1,B2,B3	#11,#12,#16	#2,#14,#20	-	-
Araldite	A4,A5,A6	B4,B5,B6	#1,#2,#3	#1,#2,#3	-	-
GFRP	-	-	-	-	CWTW	CWSW

For the sake of brevity, in Table 6, SLJ specimens are only indicated by a sequel number. In the next, the full nomenclature used to refer to SLJ specimens is the following: SD30#i and AR#j relative to specimens made of SikaDur30 and Araldite, respectively. Furthermore, the adherent specimens are named CWTW and CWSW; where CW stands for control weight and TW and SW for Tap Water and Sea Water, respectively.

To adopt the Fick's law, two data are requested:

- the water absorption  $C_i$  of the sample immersed at time  $i$ ;
- the thickness (d) of the sample.

According to the Fick model, the first step is to evaluate the time of immersion corresponding to the 70% of the saturation,  $t_{70}$ , by the following expression.

$$t_{70} = t_1 + \frac{0,7 - \frac{c_1}{c_s}}{\frac{c_2}{c_s} - \frac{c_1}{c_s}} (t_2 - t_1) \quad (13)$$

In Eqn. (13), the parameters  $C_1$  and  $C_2$  are the experimental absorption values corresponding to immersion times  $t_1$  and  $t_2$ , which are the previous and the next time respect to  $t_{70}$ , respectively. Furthermore,  $C_s$  is the experimental absorption value corresponding to the final intake.

The diffusion index,  $D$ , is evaluated by the following expression:

$$D = \frac{d^2}{\pi^2 \cdot t_{70}} \quad (14)$$

Finally, the function of the absorption respect to the time (Fick's law) is reported below:

$$c(t) = C_s - C_s \frac{8}{\pi^2} \sum_{k=1}^{20} \frac{1}{(2k-1)^2} \exp \left[ -\frac{(2k-1)^2 \cdot D \cdot \pi^2}{d^2} t \right] \quad (15)$$

In the following Tables (7-11), all values relative to the parameters  $t_{70}$  and the diffusion index  $D$  of all specimens tested, are reported. It is worth to underline that only for adhesive specimens (Tables 7 and 8), the values of thickness were reported being not equal for all specimens. In the case of SLJs, due to the presence of spacers, the thickness of the adhesive layer was kept constant. The total thickness per each SLJ specimen is equal to 21 mm being each adherent 10mm thick.

Table 7. SikaDur30 resins (40mm x 10mm x 1mm)

	Tap Water			Sea Water		
	A1	A2	A3	B1	B2	B3
d [mm]	1.20	1.30	1.40	1.50	1.50	1.30
t70 [s]	292400	927450	951800	627075	338688	522240
t70 [d]	3.38	10.73	11.02	7.26	3.92	6.04
D [mm <sup>2</sup> /s]	4.99E-07	1.85E-07	2.09E-07	3.64E-07	6.73E-07	3.28E-07

Table 8. SikaDur30 SLJ (340mm x 25mm x 21mm)

	Tap Water			Sea Water		
	A4	A5	A6	B4	B5	B6
d [mm]	0.95	1.00	1.00	1.00	0.90	1.00
t70 [s]	353864	363334	334080	247598	268736	348516
t70 [d]	4.10	4.21	3.87	2.87	3.11	4.03
D [mm <sup>2</sup> /s]	2.58E-07	2.79E-07	3.03E-07	4.09E-07	3.05E-07	2.91E-07

Table 9. Araldite resins (40mm x 10mm x 1mm)

	Tap Water			Sea Water		
	TW#11	TW#12	TW#16	SW#2	SW#14	SW#20
$t_{70}$ [s]	918845	1082592	1059563	5744310	5026505	6040408
$t_{70}$ [d]	10.63	12.53	12.26	66.49	58.18	69.91
$D$ [mm <sup>2</sup> /s]	4.86E-05	4.13E-05	4.22E-05	7.78E-06	8.89E-06	7.40E-06

Table 10. Araldite SLJ (340mm x 25mm x 21mm)

	Tap Water			Sea Water		
	TW#1	TW#2	TW#3	SW#1	SW#2	SW#3
$t_{70}$ [s]	1395051	1292465	1060029	4754795	7138165	6824712
$t_{70}$ [d]	16.15	14.96	12.27	55.03	82.62	78.99
$D$ [mm <sup>2</sup> /s]	3.20E-05	3.46E-05	4.22E-05	9.40E-06	6.26E-06	6.55E-06

Table 11. Adherent GFRP (340mm x 25mm x 10mm)

	Tap Water	Sea Water
	CWTW	CWSW
$t_{70}$ [s]	1737937	6852964
$t_{70}$ [d]	20.12	79.32
$D$ [mm <sup>2</sup> /s]	5.83E-06	1.48E-06

In the following Figures (17-25) the comparison between numerical/experimental data are presented. It is worth to underline the very good agreement between the Fick's law prediction and experimental data for all specimens tested. This last evidence confirms that the diffusion in the case of SLJ specimens as well as for the GFRP adherents is mono-dimensional (through the thickness).

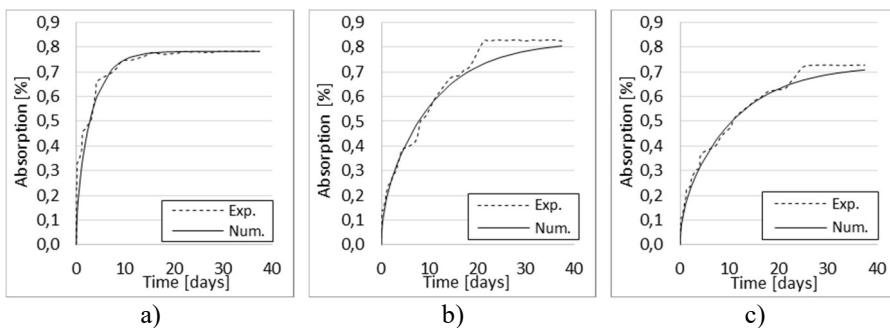


Figure 17. Sikadur30 resins in tap water: a) A1; b) A2; c) A3.

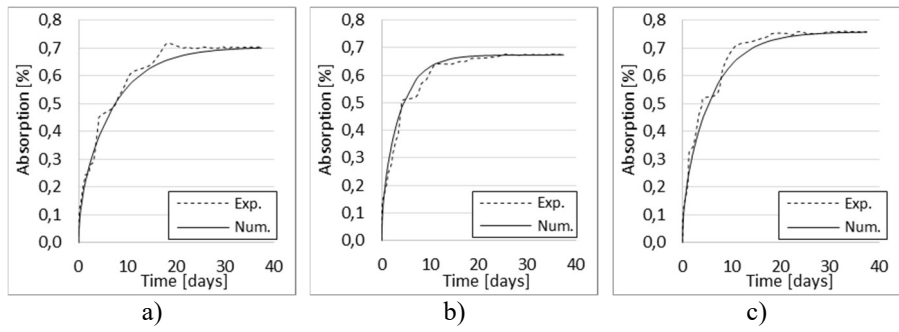


Figure 18. Sikadur30 resins in sea water: a) B1; b) B2; c) B3.

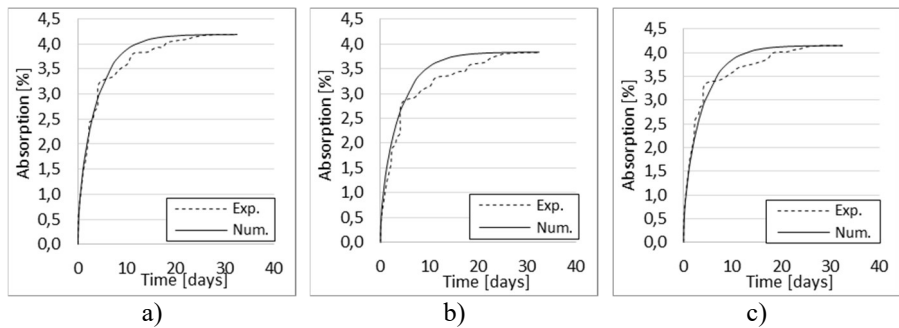


Figure 19. Araldite resins in tap water: a) A4; b) A5; c) A6.

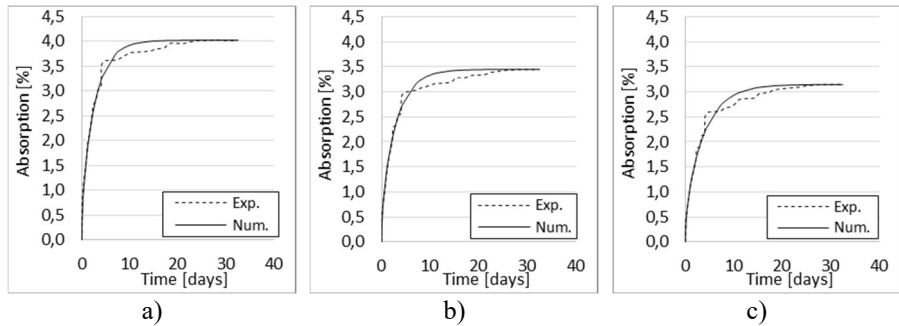


Figure 20. Araldite resins in sea water: a) B4; b) B5; c) B6.

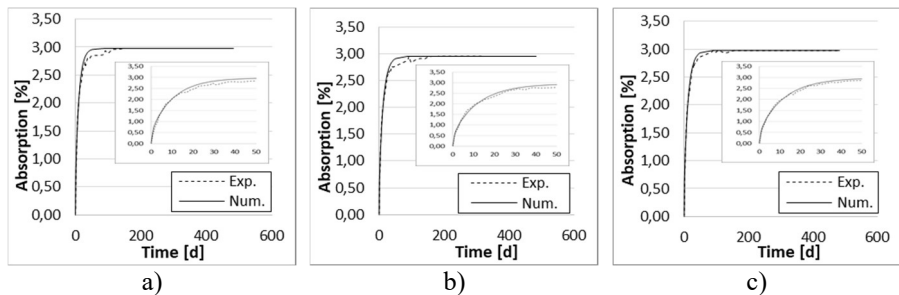


Figure 21. SikaDur30 SLJ in tap water: a) TW11; b) TW12; c) TW16.

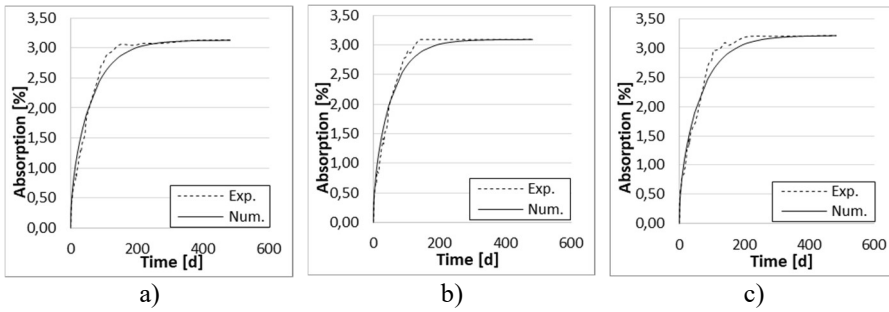


Figure 22. SikaDur30 SLJ in sea water: a) SW2; b) SW14; c) SW20.

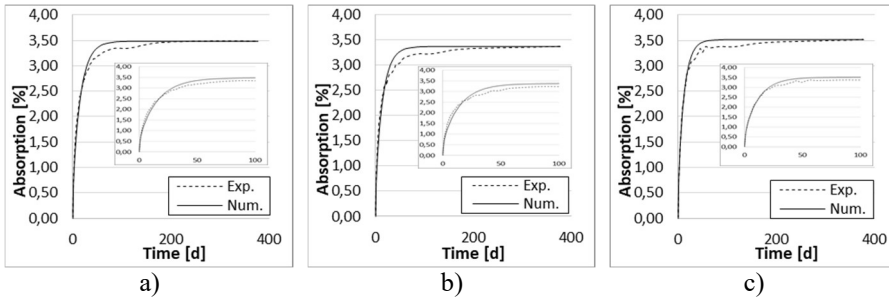


Figure 23. Araldite SLJ in tap water: a) TW1; b) TW2; c) TW3.

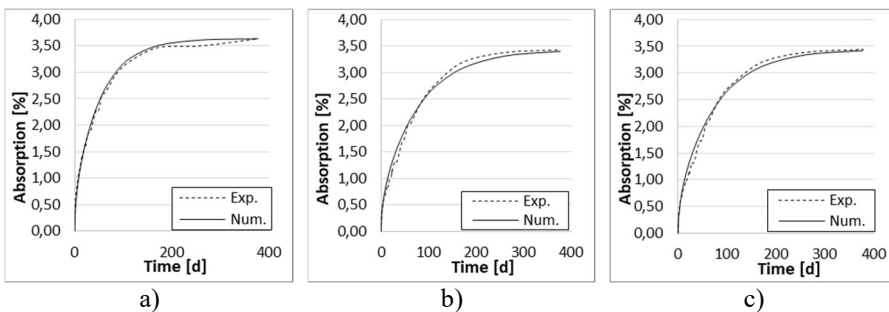


Figure 24. Araldite SLJ in sea water: a) SW1; b) SW2; c) SW3.

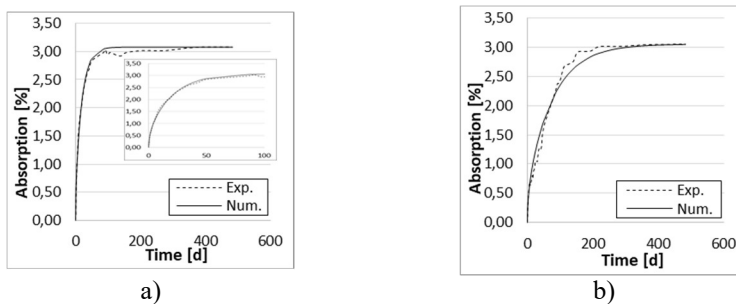


Figure 25. GFRP adherents: a) tap water; b) sea water.

### 1.2.5. Variability over the time of the mode II fracture energy

In this subsection all values of the fracture energy for both resins are reported according to the procedure described and discussed in the subsection 1.1.6. In detail, in Figures 26 and 27, the variability of the three average values of the fracture energy ( $G_{II,P_{nl}}$ ,  $G_{II,P_{max}}$  and  $G_{II,P_u}$ ) are depicted for each resin and for each type of conditioning. For the sake of brevity, in the Appendix B. Table 40 for SLJs with Araldite and Table 41 for SLJs with SikaDur30 in term of P- $\delta$ - $G_{II}$  for each three values, in Table 42 and in Table 43 in term of average values and standard deviation for Araldite and SikaDur30, respectively.

As expected, due to the not fully curing degree for both adhesives as depicted in section 1.2.1, the temperature of the water (about 30°C) triggers a post-curing phase. As a consequence, in the first five months per each resin it is possible to observe an increase especially with reference to the  $G_{II,P_u}$  values. It is worth to underline that the beneficial effect of the post-curing phase is more evident in general for Araldite than for SikaDur 30. This result seems to be in contrast with the results obtained about the curing degree: in fact, it was evaluated in 97% for the Araldite system and 82% for the SikaDur 30 system. If the chemical nature of the two different systems is not taken into consideration, the most significant changes in the structural organization of the resins (during the post-curing phase in water) are expected to occur for the SikaDur 30 system, which is characterized by a lower curing degree and hence an expected major tendency to reorganize. It is worth noting that the Araldite based system is characterized by many polar sites in the structure of the resin, able to give a higher absorption of water (in equilibrium condition) than the SikaDur 30 system. The plasticization determined by the higher concentration of water molecules results in higher mobility of the chain segments with more consistent rearrangements in the structure, which most affect the changes in fracture energy observed in Figure 27. After this initial increment, the conditioning leads to a decrement of the fracture energies as expected.

Among the three values of energy before cited, the  $G_{II,P_u}$  value (corresponding to the maximum fracture energy and to the entire FPZ) is more sensible to variation than the others two for which the FPZ is limited ( $G_{II,P_{max}}$ ) or absent ( $G_{II,P_{nl}}$ ). The more sensible variations of  $G_{II,P_{max}}$  and  $G_{II,P_u}$  values, especially when Araldite is considered could be justified coupling the effect of the curing degree and the water absorption.

More in details, relative to the Araldite resin and to the values collected in the Appendix B, the reduction of the fracture energy  $G_{II,P_u}$  is equal to 20% for seawater conditioning and 77% for tap water conditioning.

Furthermore, relative to SikaDur 30 adhesive and values collected in Appendix B, an increase of the fracture energy  $G_{II,P_u}$  equal to 20% and 40% was evaluated for seawater and tapwater conditioning, respectively. The long term increment evaluated for SikaDur 30 and the long term decrement for the Araldite is in agreement with results above mentioned of the curing degree. It is possible to conclude that the effect of the water absorption vanishes along the time while the beneficial effect of the water temperature became stronger. From a civil engineering point of view the most reliable value for the fracture energy is that one named  $G_{II,P_{nl}}$  for which the adhesive is totally in an elastic stage and no micro fractures (absence of FPZ) were activated. Relative to Araldite, no reduction was evaluated for seawater while a reduction equal to 61% was experimentally observed for tap water, confirming a major general influence of tapwater respect to the seawater. Relative to the SikaDur 30, instead, a reduction of 18% was evaluated for seawater while no reduction was evaluated for tapwater conditioning. The higher reductions evaluated for the Araldite resin confirms its initial ductile behaviour which tends to a brittle one when conditioning effect is taken into account.

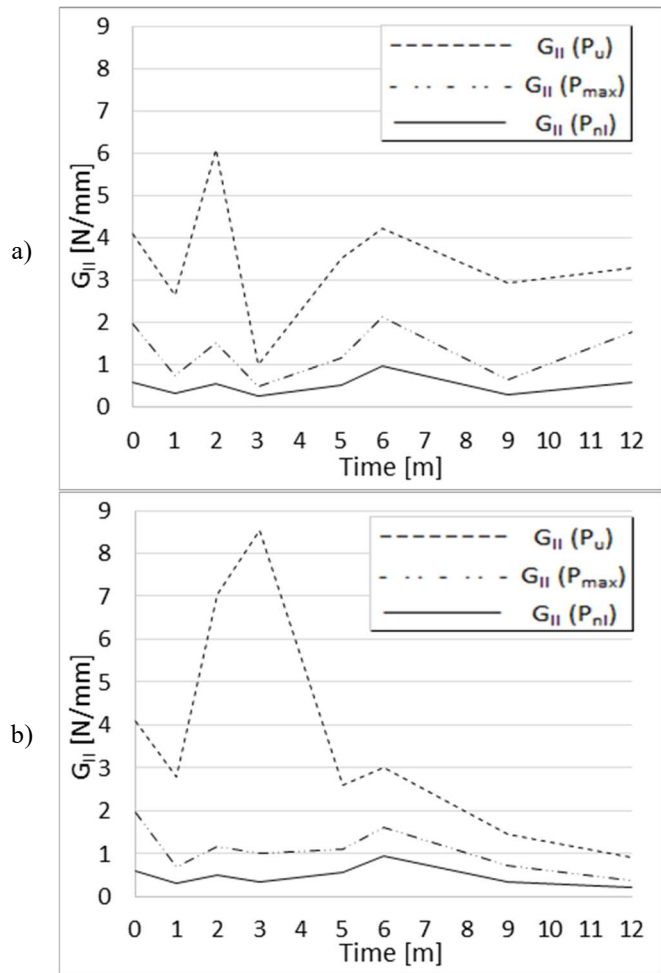


Figure 26. Araldite Fracture Energy durability: a) seawater, b) tap water.

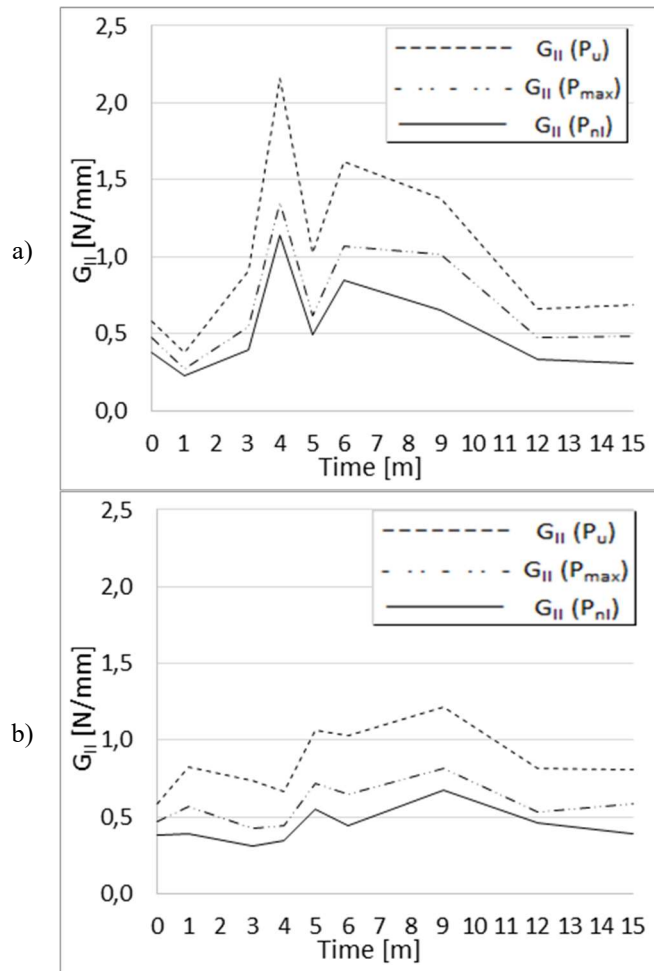


Figure 27. SikaDur 30 Fracture Energy durability: a) seawater, b) tap water.

The above-mentioned drastic modification of the behaviour of Araldite is depicted in Figure 28 where a representative  $P$ - $\delta$  curve, corresponding to the twelve months of conditioning, is compared with that one relative to the absence of any kind of conditioning.

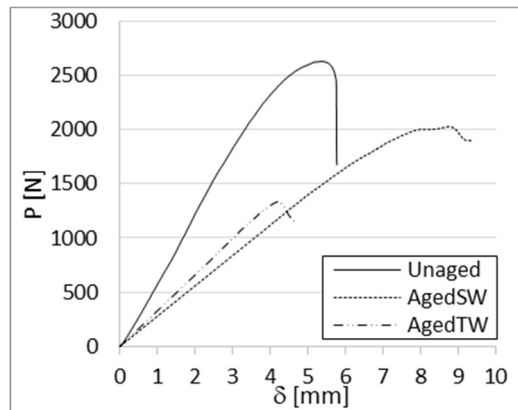


Figure 28. P-d curve of the Araldite epoxy resins behaviour: Unaged vs Aged (12th month).

### 1.2.6. Further results relative to absorption phenomenon

Table 12 reports the average ( $\mu$ ) and standard deviation ( $\sigma^2$ ) values of the three mentioned loads  $P$  within the corresponding both vertical displacements  $\delta$  and the fracture energy values.

Table 12. Test results relative to SLJ specimens after absorption period.

		<i>End of Elastic Stage</i>			<i>End of Post-Elastic Stage</i>			<i>End of fracture propagation</i>			
		$P_{nl}$ [N]	$\delta_{nl}$ [mm]	$G_{II, Pnl}$ [N/mm]	$P_{max}$ [N]	$\delta_{max}$ [mm]	$G_{II, Pmax}$ [N/mm]	$P_u$ [N]	$\delta_u$ [mm]	$G_{II, Pu}$ [N/mm]	
SikaDur30	<i>Unaged</i>	$\mu$	1577	2.56	0.38	1624	2.72	0.47	1366	2.57	0.58
		$\sigma^2$	0.05	0.01	0.14	0.04	0.02	0.14	0.03	0.02	0.11
	<i>Aged (SW),A</i>	$\mu$	1492	2.33	0.31	1642	2.68	0.48	1385	2.87	0.69
		$\sigma^2$	0.06	0.04	0.16	0.04	0.04	0.17	0.14	0.04	0.13
	<i>Aged (TW),A</i>	$\mu$	1622	2.82	0.39	1744	3.16	0.59	1585	59.11	0.81
		$\sigma^2$	0.01	0.01	0.03	0.02	0.01	0.06	0.03	4.45	0.08
Araldite	<i>Unaged</i>	$\mu$	2053	3.30	0.59	3129	5.26	1.97	2941	6.68	4.11
		$\sigma^2$	0.03	0.03	0.10	0.10	0.11	0.37	0.11	0.11	0.34
	<i>Aged (SW),A</i>	$\mu$	1430	4.05	0.59	2082	7.73	1.77	1935	9.18	3.28
		$\sigma^2$	0.01	0.11	0.10	0.01	0.01	0.03	0.00	0.00	0.00
	<i>Aged (TW),A</i>	$\mu$	892	2.60	0.23	1030	3.16	0.38	1060	4.44	0.92
		$\sigma^2$	0.15	0.13	0.38	0.09	0.07	0.21	0.01	0.01	0.03

A= continuous absorption

Figure 29 reports all the experimental P- $\delta$  curves for the unaged and aged specimens as well as both resins. Matching the values of Table 12 and the curves of Figure 29, it is possible to observe that in general no relevant changes for SikaDur30 were revealed even if an increment of the fracture energy  $G_{II,P_u}$  was recorded. This last result was due to the fact that the curing degree of SikaDur 30 (cured at  $23 \pm 2$  °C) was equal to 87%. The curing degree was estimated by the calorimetric data obtained with a Differential Scanning Calorimetry (DSC) test (it was assumed that the exothermic heat evolved during curing is proportional to the extent of the reaction).

The temperature of the water in which the samples were immersed activated a post curing phase with a consequent increment of the fracture energy. The beneficial influence of post-curing is greater than the degradation due to plasticization and/or hydrolysis. The ultimate load is increased, while the whole stiffness of the P- $\delta$  curve is substantially the same (for SikaDur 30 the behaviour is linear elastic). In contrast, significant changes were monitored in the case of Araldite, both in terms of the fracture energy and stiffness. The greatest reduction, in terms of fracture energy  $G_{II,P_u}$ , was recorded in the case of tap water conditioning. In general, the decrease of Araldite was due to the fact that its curing degree (the curing was performed under the same conditions as SikaDur 30) was equal to 98%. The temperature of the water, differently from the case of SikaDur 30, was not sufficient to activate a post curing phase. The degradation phenomenon, due to plasticization and/or hydrolysis, subsequently analysed in detail, is more evident. Both the ultimate load and the initial stiffness of the P- $\delta$  curve were halved. Furthermore, the mechanical response was changed, from a ductile behaviour (elastic and post-elastic stage) for the unaged specimen to a linear elastic for the aged ones.

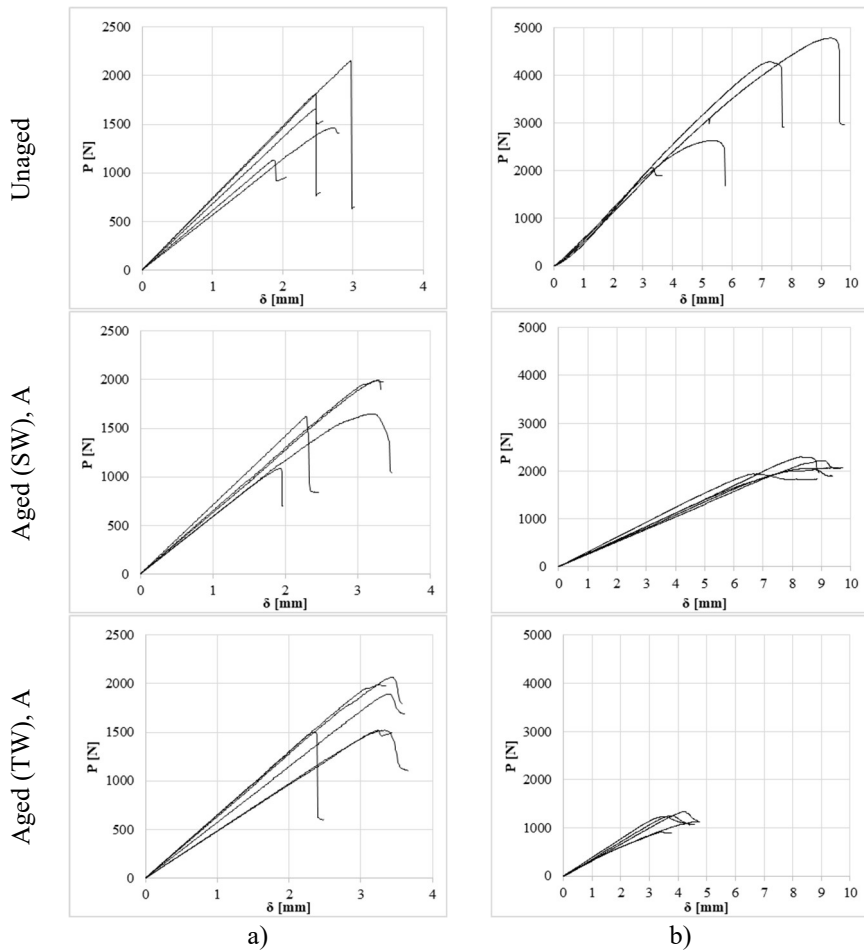


Figure 29. Experimental P- $\delta$  curves for unaged and aged specimens: a) SikaDur30; b) Araldite.

### 1.2.7. Further results relative to desorption phenomenon

Table 13 reports the average ( $\mu$ ) and standard deviation ( $\sigma^2$ ) values of the three mentioned loads P within both the corresponding vertical displacements  $\delta$  and the fracture energy values.

All the data recorded during the experimental program are in Appendix C and in Appendix D.

Table 13. Test results relating to the SLJ specimens (Araldite) after the desorption period.

		<i>End of Elastic Stage</i>			<i>End of Post-Elastic Stage</i>			<i>End of fracture propagation</i>		
		$P_{nl}$	$\delta_{nl}$	$G_{II, Pnl}$	$P_{max}$	$\delta_{max}$	$G_{II, Pmax}$	$P_u$	$\delta_u$	$G_{II, Pu}$
		[N]	[mm]	[N/mm]	[N]	[mm]	[N/mm]	[N]	[mm]	[N/mm]
<i>Unaged</i>	$\mu$	2053	3.30	0.59	3129	5.26	1.97	2941	6.68	4.11
	$\sigma^2$	0.03	0.03	0.10	0.10	0.11	0.37	0.11	0.11	0.34
<i>Aged SW,D</i>	$\mu$	1995	3.34	0.57	2378	4.18	1.11	2840	7.43	4.39
	$\sigma^2$	0.05	0.10	0.27	0.01	0.04	0.09	0.13	0.07	0.18
<i>Aged TW,D</i>	$\mu$	1663	2.92	0.42	2038	3.77	0.87	2636	8.11	4.74
	$\sigma^2$	0.00	0.00	0.00	0.00	0.01	0.02	0.06	0.02	0.12

D= continuous desorption

Figure 30 shows all the experimental P- $\delta$  curves for the unaged and aged specimens (desorbed). Matching the values reported in Table 13 and the curves reported in Figure 30, it is possible to observe that not only the strength but also the stiffness is almost recovered after the desorption period. In detail, the stiffness and strength of the SLJs were similar to those of the unaged condition. The degradation observed during the absorption period was probably due to plasticization more than to hydrolysis, considering the almost complete recovery of the mechanical properties in terms of the strength (SW 76%, TW 65%), the stiffness (SW 96%, TW 92%) and the fracture energy in mode II (SW 107%, TW 115%) respect to the unaged condition. As confirmed by current literature, an ageing at low temperatures (30°C) can lead to a plasticization characterized by reversible deformation [73].

Furthermore, the most significant variations in terms of fracture energy in mode II due to the desorption phenomenon are relative to the ultimate value (the conventional one) of the energy, called  $G_{II, Pu}$ . For the other two values ( $G_{II, Pnl}$  and  $G_{II, Pmax}$ ) the variation is negligible. Both in the case of sea water and tap water conditioning, the value of the fracture energy  $G_{II, Pu}$ , after desorption is greater than that of the unaged condition. This is an expected result considering that both the fracture energy is evaluated in function of the SLJs compliance which was almost completely recovered as previously described and the temperature of 30°C of the water where the SLJs were immersed activated a post-curing phase [74].

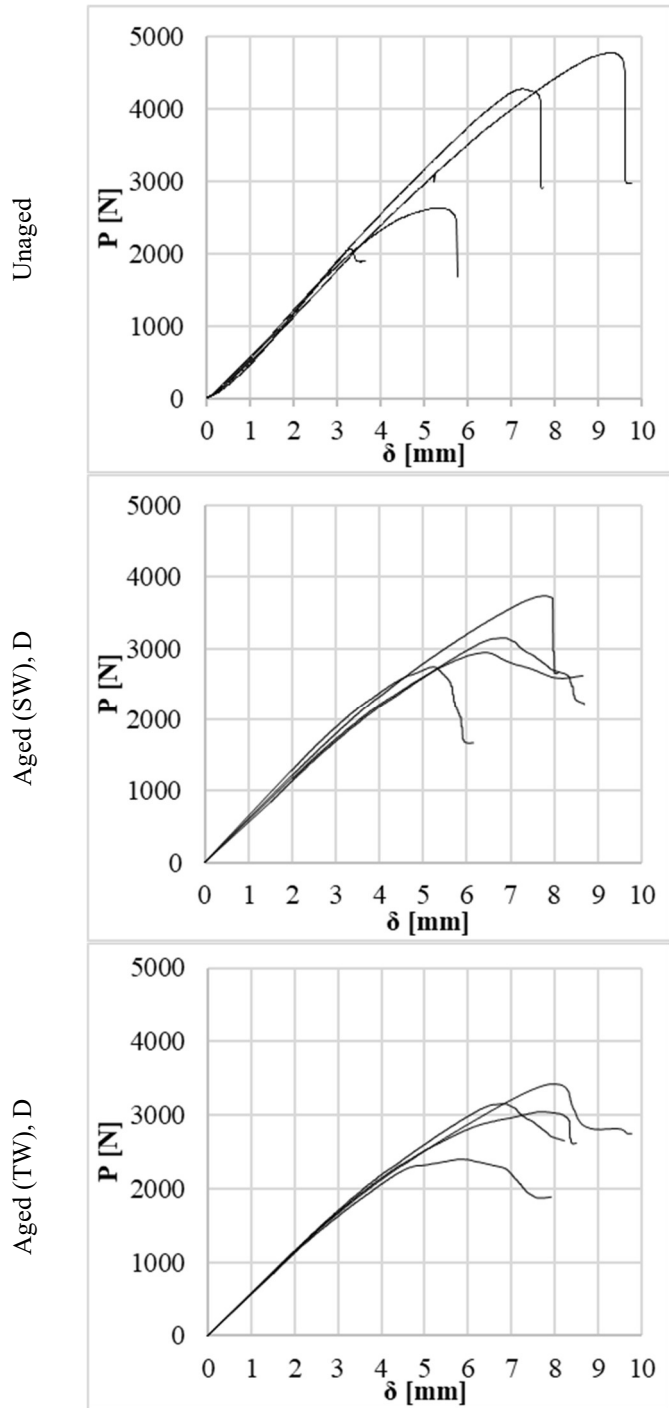


Figure 30. Experimental P- $\delta$  curves for unaged and aged specimens (Desorbed) with Araldite.

### 1.3. Conclusions

A large experimental program was developed comprising one hundred and seventy-seven single lap joints and six resin samples (three per each adhesive). The fracture energy was evaluated by adopting the End Notch Failure test while the absorption behaviour by evaluating the change in weight of the samples.

The two resins were preliminary studied by evaluating both the glass transition temperature ( $T_g$ ) and their curing degree (C.D.) by thermal analysis performed with the differential scanning calorimeter Mettler DSC 822 operating under nitrogen flow.

It resulted that the SikaDur 30 system manifests a value of  $T_g$  around 15°C, whereas the Araldite a higher value of about 45°C. Both resins were isothermally cured at Room Temperature, with values ranging between 23°C and 25°C, for seven days for the SikaDur30 based-system and 1 day for the Araldite based-system. Furthermore, the curing degree of the SikaDur 30 system results in a percentage of 82%, whereas that of the Araldite 97%.

For what concerns the fracture energy variation over the time (for the conditioning considered) it is possible to conclude that it is higher for Araldite respect to the SikaDur 30 resin due to the coupling effect of the curing degree and the water absorption.

Among the three different values of the fracture energy in mode II evaluated in this chapter ( $G_{II,P_{nl}}$ ,  $G_{II,P_{max}}$  and  $G_{II,P_u}$ ), corresponding respectively to the load for which the linearity is lost, to the maximum load and to the load for which the evolution crack stopped, only the first one is considered the most reliable for civil engineering application due to the circumstance that the adhesive is totally in elastic stage. Relative to  $G_{II,P_{nl}}$  values, the fracture energy reductions are limited in general making both resins suitable for civil engineering applications.

For what concerns the water absorption of resins, it is possible to conclude that SikaDur 30 final intakes were 0.71% and 0.78% for SW and TW, respectively (with a difference equal to 9%). While, for Araldite the final intakes were 3.54% and 4.06% for SW and TW, respectively (with a difference equal to 15%). In general, it is possible to conclude that water intake for Araldite is 5 times bigger than that of SikaDur 30 irrespective of the type of liquid.

Single lap joints present the same final water intake irrespective of adhesive used: about 3.0% for SikaDur 30 and 3.5% for Araldite. A further important result is that Sea Water (SW) reduces drastically the intakes at early stages making longer the period of immersion to reach the final intake respect to the

Tap Water (TW). Considering the results for joints with SikaDur 30, the final intake was reached for SW in five months instead of the three months for the case of TW.

The results obtained demonstrated that after the absorption period, the strength and stiffness of the resins decreased due to a plasticization phenomenon, while after the desorption period their mechanical properties become similar to those relative to the unaged condition.



# **CHAPTER II: The influence of the hygrothermal aging on the strength and stiffness of adhesives used for civil engineering applications with pultruded profiles: a numerical investigation**

## **2. Introduction**

The chapter aims to investigate, from a numerical point of view, the effect of the hygrothermal ageing on both the fracture energy in mode II as well as the strength and stiffness of two commercial epoxy resins experimentally studied in the Chapter 1. Finally, in view of a safe design of a bonded joint, limiting its behaviour to only the elastic field, a lower fracture energy value is presented in relation to the classical one.

More in detail, a Finite Element Model (FEM), by using the commercial Abaqus code, was built. It is capable of perfectly describing, on one hand, the End Notch Failure (ENF) test used to evaluate fracture energy in mode II as requested by current standards [24], while on the other, to evaluate the stiffness of the elastic and softening stages in the case of ageing.

### **2.1. Finite Element Model and simulation**

This section is organized into five subsections: in the first, a 2D model is introduced in order to reproduce the ENF experimental test; in the second subsection, the cohesive model assumptions are reported; in the third, the governing parameters are presented and their influence on the mechanical response of the ENF joint studied; in the fourth subsection, a numerical-experimental comparison in terms of P- $\delta$  curves is presented; in the last subsection, the effect of ageing as well as that of the absorption phenomenon on the interfacial bond law is evaluated.

#### **2.1.1. Mesh details and boundary condition of the 2D model used for ENF test**

In this sub-section, a numerical model of the single lap joint (suitable for ENF test) is built with the commercially available FEM code Abaqus. According to

the geometrical dimensions of the joint as previously reported, being the width of the adherents larger (2,5 times) than their thickness, the adhesive joint modelization could be simplified by taking into account the elastic-plastic plane strain problems (2D problem).

The scheme of the joint is presented in previous chapter where the adherents are pultruded profiles reinforced with glass fibres (GFRP). They are then classified as elements made of orthotropic transversally isotropic material. Consequently, the five mechanical parameters which describe their mechanical behaviour are reported in Table 14, where the plane 2-3 is one of isotropy. The values are referred to the unaged condition.

Table 14. GFRP mechanical parameters.

density [g/cm <sup>3</sup> ]	$E_1$ [MPa]	$E_2$ [MPa]	$\nu_{12}$ [-]	$\nu_{23}$ [-]	$G_{12}$ [MPa]
1.9	24000	7000	0.07	0.23	3000

Figure 31 shows a view of the 2D model. The GFRP components were modelled by four-node elements (CPS4R) with a 0.5 mm side length. The contact between the adhesive surfaces was modelled by cohesive laws (“surface to surface” interaction), in mode II only, while the contact between the GFRP elements, in the zone corresponding to the initial notch 80 mm long, was modelled by a “hard contact” formulation with no friction.

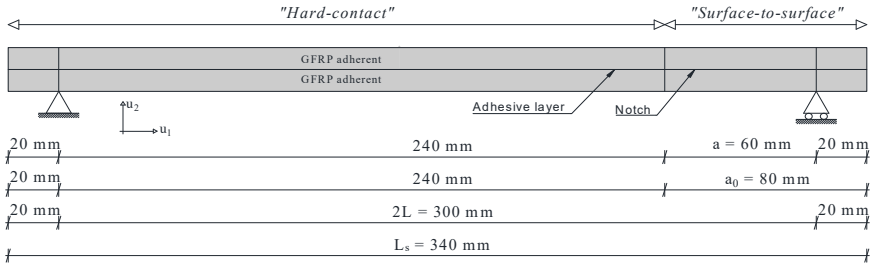


Figure 31. View of the 2D Model.

Preliminary, the choice to model the thickness of each adherent by 20 elements was validated by making a comparison between a FEM model and the closed form solution of a simply supported Timoshenko beam, whose geometrical dimensions are those of the SLJ joint of Figure 2.a. Within this purpose, the adhesive connection between the adherents was extended to the whole adherent length and it was considered perfectly rigid (“tie” interaction).

In Figure 32, the boundary conditions, relating to the scheme of a simply supported beam, are depicted (1 and 2 are the horizontal and vertical axis, respectively, while U is the displacement).

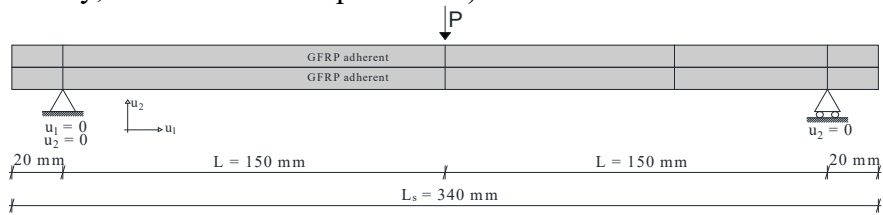


Figure 32. Boundary conditions of the 2D model.

The parameter selected for the convergence test, with results depicted in Figure 33, was the deflection at mid-span,  $U_2$ .

Furthermore, the number of elements along the longitudinal axis of the joints is 680, for a total of 13600 elements per each adherent.

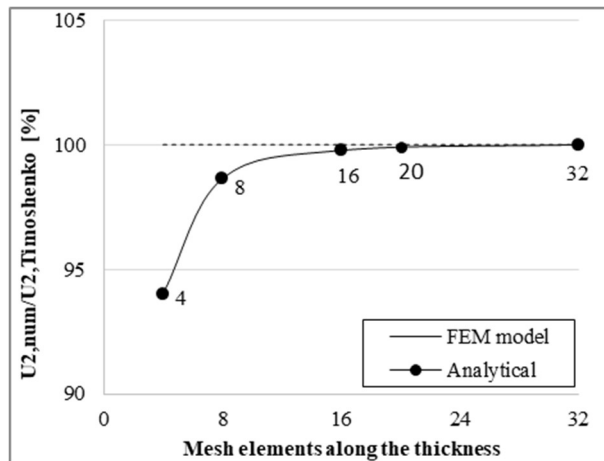


Figure 33. Convergence test: mid-span deflection vs number of elements along the thickness.

From Figure 33, it is possible to confirm that the number of 20 elements along the thickness of each adherent is the lowest value in order to obtain a correct solution.

### 2.1.2. Cohesive zone model assumption

The cohesive law adopted in this study is the bilinear one being the best and simplest law to model the behaviour of resins under investigations as shown in

[74]. Figure 34 shows the traction separation law in shear. The symbols introduced assume the following meanings:  $\tau_u$  is the ultimate shear stress,  $s_e$  is the sliding (relative horizontal displacement between adherents) at the limit elastic stage, while  $s_u$  is the sliding corresponding to the complete separation between adherents.

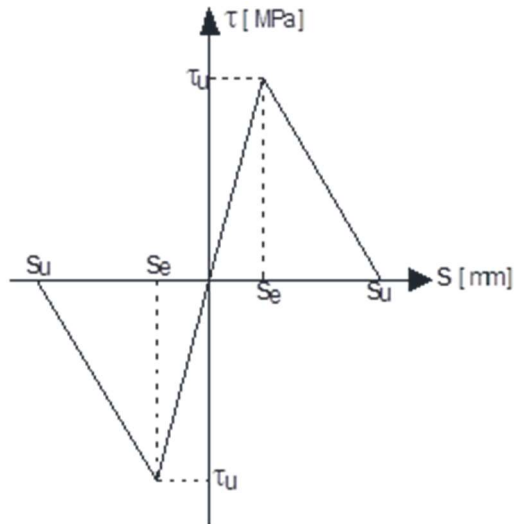


Figure 34. Traction-separation law in mode II.

The interfacial fracture energy can be expressed by the following formulation:

$$G_{II,P_u} = \int_0^{s_u} \tau ds = \frac{1}{2} \tau_u s_u \quad (16)$$

The displacement is supposed monotonically increased, then the interface begins to soften and to degrade, when the damage starts. The interfacial damage occurs when the quadratic nominal stress criterion is satisfied:

$$\left(\frac{\tau}{\tau_u}\right)^2 = 1 \quad (17)$$

The damage variable  $D$  assumes the following expression:

$$D = \frac{s_u (s - s_e)}{s (s_u - s_e)} \quad (18)$$

where  $s$  is the current sliding. From Eqn. (18), it is easy to verify that if  $s = s_e$ , the damage variable is equal to zero; while, if  $s = s_u$ , the damage variable is equal to 1 (corresponding to complete separation between adherents, which are no longer connected by the adhesive layer).

The latter condition ( $D = 1$ ) corresponds to satisfying the following linear fracture criterion here adopted:

$$\frac{G_{II}}{G_{II,P_u}} = 1 \quad (19)$$

The symbol  $G_{II}$  represents the work done by the traction (shear stress) and its conjugate relative displacement (sliding).

### 2.1.3. Load-bearing capacity and governing parameters

To faithfully reproduce the ENF experimental procedure, used to evaluate the fracture energy in mode II of the two resins under investigation, the numerical analyses were carried out using displacement control.

In order to build the typical load vs displacement curve of an ENF test (Figure 6), the following governing parameters were fixed: the adhesive fracture energy,  $G_{II,P_u}$ , and the shear limit stress,  $\tau_u$ , as material parameters for the adhesive layer and the modulus of elasticity,  $E_1$  (Table 14), of the adherents (which fibers are supposed to be parallel to the longitudinal axis) as the material parameter for the pultruded members.

A parametric study on the influence of each parameter on the load-bearing capacity of the SLJ joint was conducted. Based on the adhesives and GFRPs commonly used for civil engineering applications, the following ranges of values for the fracture energy, the ultimate shear stress and the modulus of elasticity along fiber direction were adopted:

$$0.5 \frac{N}{mm} \leq G_{II,P_u} \leq 10.0 \frac{N}{mm} \quad (20)$$

$$5.0 \frac{N}{mm^2} \leq \tau_u \leq 50.0 \frac{N}{mm^2} \quad (21)$$

$$10000.0 \frac{N}{mm^2} \leq E_1 \leq 30000.0 \frac{N}{mm^2} \quad (22)$$

In Figure 35, the maximum load ( $P_{max}$ ) vs limit shear stress ( $\tau_u$ ) curves are reported as the fracture energy increased. For low values of the fracture energies (0.5-1.5 N/mm), no significant differences in terms of load  $P_{max}$  are recorded when varying the shear strength. On the contrary, for high values of the fracture energy, significant differences in terms of load  $P_{max}$ , are recorded when varying the limit shear stress. Similar trends were found in [74]. Furthermore, in order to verify that the fracture energy in mode I had no effects on the results obtained, the graph of Figure 35 was replaced twice obtaining the same result:  $G_{I,P_u}$  was assumed equal to 1 N/mm and 100 N/mm.

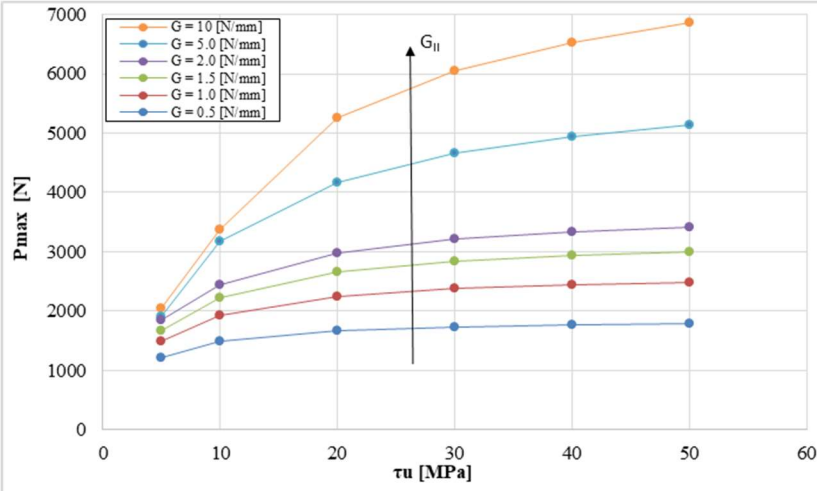


Figure 35. Maximum load vs limit shear stress curves varying the fracture energy.

Furthermore, the P- $\delta$  curves, for a fixed value of  $G_{II,P_u}$  and  $E_1$  varying the limit shear stress, are depicted in Figure 36; while the P- $\delta$  curves, for a fixed value of  $\tau_u$  and  $E_1$  and varying the adhesive fracture energy, are depicted in Figure 36. It is worth noting how the shear stress parameter governs the shape of the curve (Figure 36a) passing from a ductile behaviour for low values of  $\tau_u$  to an elastic behaviour for high values of it with a consequent increase of the maximum load in accordance with the results presented in Figure 35. The adhesive fracture energy influences the maximum load only (Figure 36b). Similar conclusions were presented in [74].

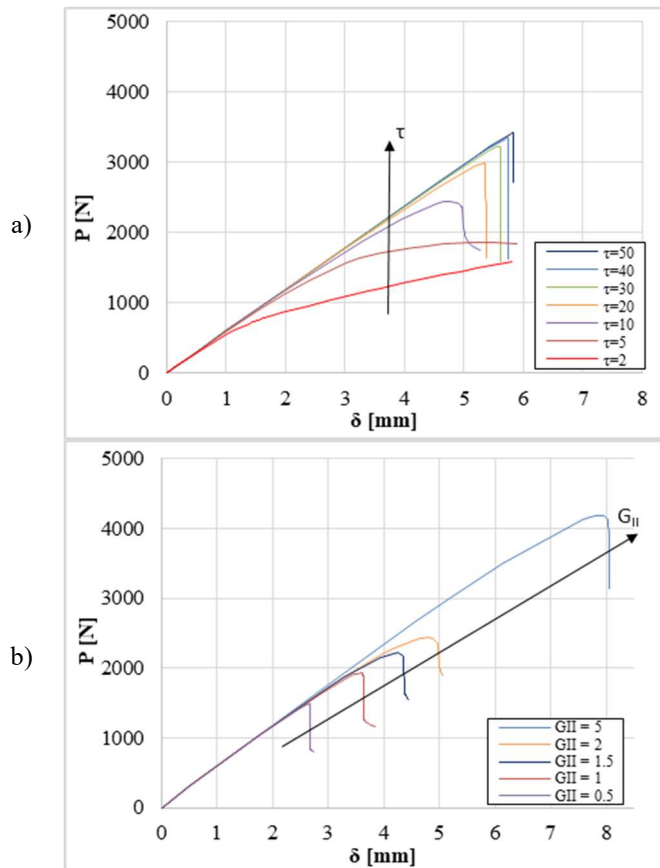


Figure 36. Numerical P- $\delta$  curves: a) influence of  $\tau_u$ ;  
b) influence of  $G_{II}$ .

In Figure 36 use  $E=24000$  MPa and in Figure 36.a  $G_{II,u} = 2$  N/mm while in Figure 36.b  $\tau=10$  MPa.

Regarding the influence of the GFRP material parameter, in Figure 37 the P- $\delta$  curves of a ENF test, for a fixed values of  $G_{II,P_u}$  and  $\tau_u$  varying the modulus of elasticity of the adherents, are depicted.

It is possible to conclude that the Young's modulus governs the stiffness of the P- $\delta$  curves: the higher the modulus is, the higher the stiffness and strength are.

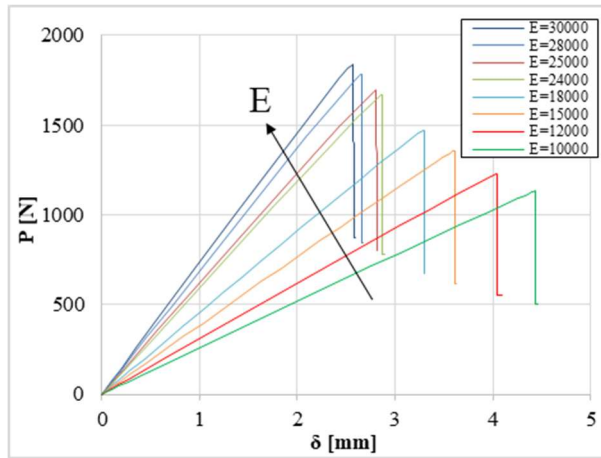


Figure 37. Numerical P- $\delta$  curves: influence of  $E_1$ .

In Figure 37 use  $\tau_u = 20$  MPa,  $G_{II,u} = 0.55$  N/mm

#### 2.1.4. P- $\delta$ curves: a comparison between numerical and experimental investigation

In this sub-section a comparison between the numerical and experimental results, in terms of P- $\delta$  curves, are presented and discussed. In detail, the comparison is referred, for each epoxy resin under investigation, to the unaged and aged ultimate condition (15 months for SikaDur 30 and 12 months for Araldite).

Relating to the unaged and aged condition, the following values for the governing parameters were considered to perform the numerical simulations (see Table 15).

Table 15. Values of the governing parameters for unaged and aged conditions.

	SikaDur 30			Araldite AV 5308		
	$G_{II,u}$	$\tau_u$	$E_1$	$G_{II,u}$	$\tau_u$	$E_1$
	[N/mm]	[MPa]	[MPa]	[N/mm]	[MPa]	[MPa]
Unaged	0.58	17	24000	4.11	9	24000
Aged SW,A	0.69	17	24000	3.28	7 (22%)	12000 (50%)
Aged TW,A	0.81	17	24000	0.92	7 (22%)	12000 (50%)
Aged SW,D	-	-	-	4,39	9	24000
Aged TW,D	-	-	-	4,74	9	24000

A= absorption, D= desorption, in ( ) the reduction in percentage respect to unaged condition

The values relative to the unaged condition are presented in the previous chapter for both the adhesives and the GFRP while those relative to the aged conditions were evaluated as follows:

- for SikaDur 30, no significant changes in terms of the stiffness ( $E_1$ ) and the shape ( $\tau_u$ ) of the P- $\delta$  curves were observed after ageing;
- for Araldite AV 5308, on the contrary, due to the aging conditioning the shape of P- $\delta$  curves changed from ductile to elastic (decrement of  $\tau_u$ ) and the stiffness of P- $\delta$  curves decreased (decrement of  $E_1$ );
- for both the adhesives, the values of the fracture energies were those experimentally obtained.

A further comment is needed in relation to the decrease of the modulus of elasticity in the case of Araldite only. Being the GFRP material the same for both types of the SLJs realized with SikaDur 30 and Araldite, the decrease of  $E_1$  could be expected to be the same in both circumstances. It is a function of the absorption capacity of the resin which was five times greater for Araldite than that of SikaDur 30. This means that the amount of water that penetrated into the adhesive degrades further the GFRP adherents, compared to the case of SikaDur 30, due to not only attacking by water through the ether surfaces but also through the bonded surfaces.

The degradation of the GFRP (about 50%), in terms of the modulus of elasticity, is in accordance with the previous results reported in current literature where the GFRP elements were immersed in seawater and tap water for a long time to evaluate the ageing influence on the mechanical properties [16, 18, 21, 17, 75, 76]. The reduction of the mechanical properties was attributed to the effects of swelling and plasticization of the matrix and degradation at the fiber/matrix interface, induced by prolonged immersion in water.

Regarding the shear strength reduction (22%), it was evaluated by matching the numerical results with the experimental ones.

Finally, regarding the values of the governing parameters referring to the aged conditions after desorption, based on the previous results, they were assumed equal to those of the unaged condition.

Figures 38 and 39 show the P- $\delta$  curves with the absorption phenomenon only, relative to the SLJs with SikaDur 30 and Araldite respectively. While, Figure 40 shows the P- $\delta$  curves with the desorption phenomenon, relating to the SLJs with Araldite only. The analytical P- $\delta$  curves are able to capture the stiffness, the trend and the ultimate load of the companion experimental curves.

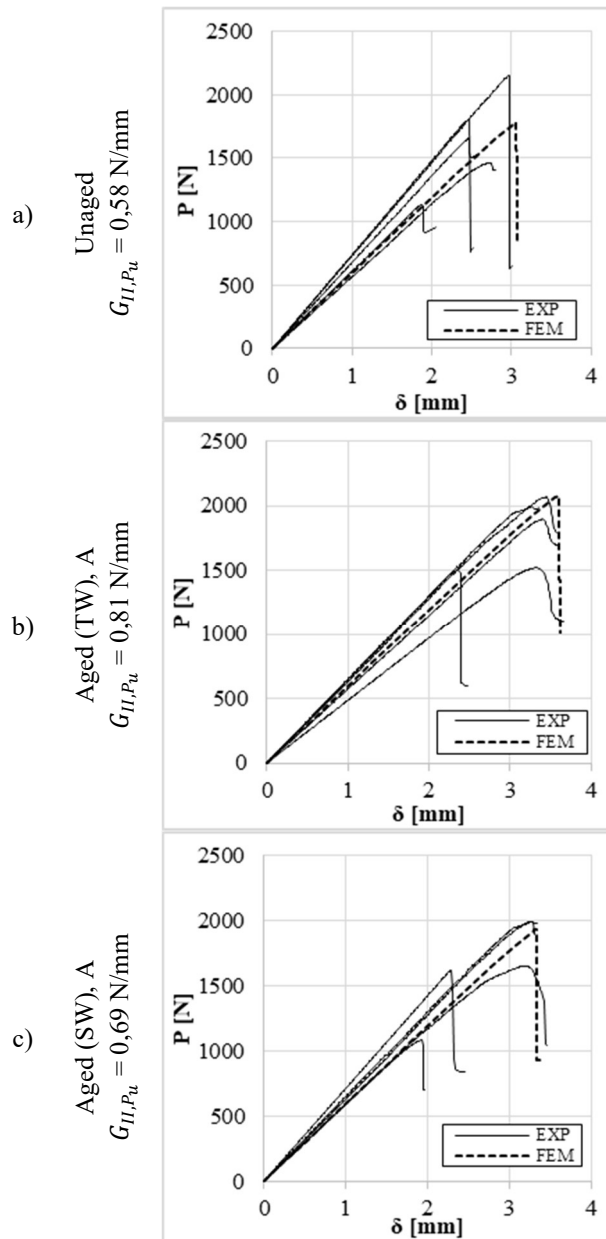


Figure 38. P- $\delta$  curves for SLJ with SikaDur30: a) unaged condition; b) aged condition in tap water (absorption only); c) aged condition in sea water (absorption only).

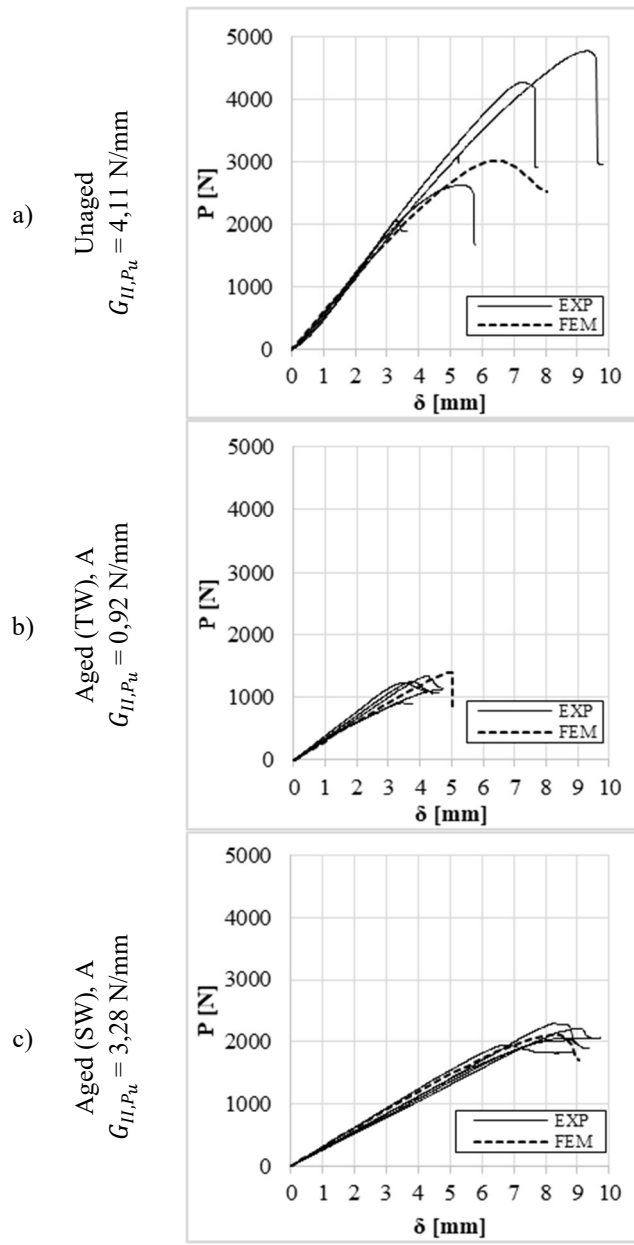


Figure 39. P- $\delta$  curves for SLJ with Araldite: a) unaged condition; b) aged condition in tap water (absorption only); c) aged condition in sea water (absorption only).

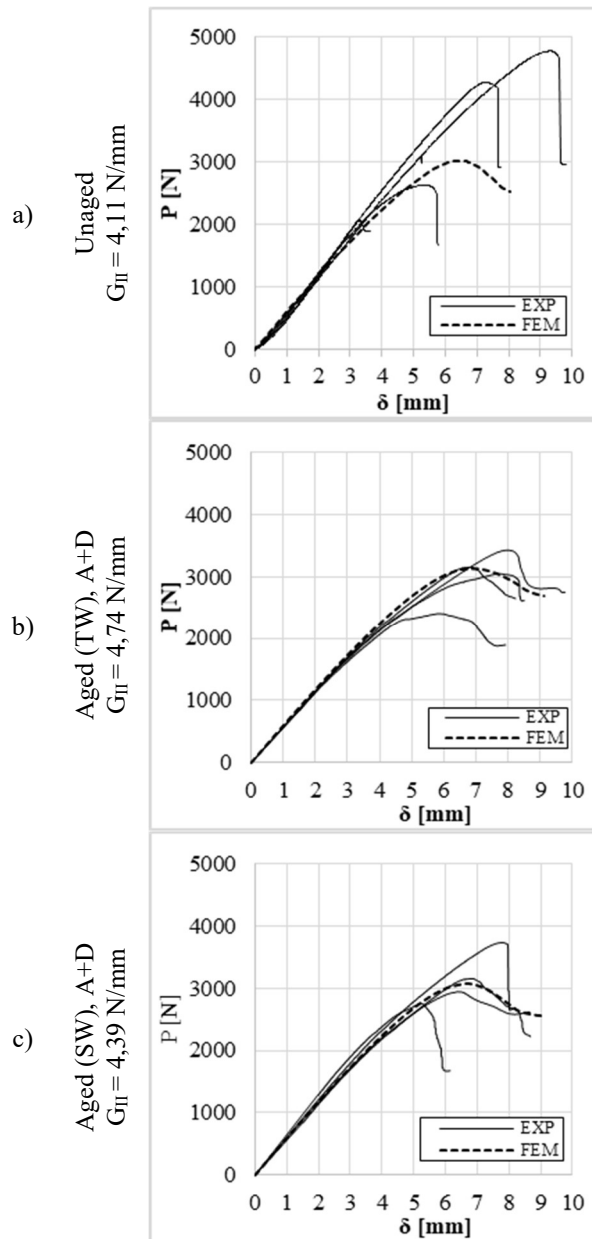


Figure 40. P- $\delta$  curves for SLJ with Araldite: a) unaged condition; b) aged condition in tap water (desorption); c) aged condition in sea water (desorption).

### 2.1.5. Interface slip and strength: fracture propagation and safe design

Considering the bilinear shape of the interface law introduced in section 2.1.2 and fixing the value of the fracture energy equal to the one experimentally obtained ( $G_{II,P_u}$ ), that of the shear strength ( $\tau_u$ ) equal to the yield strength furnished by the supplier, the ultimate slip ( $s_u$ ), which corresponds to the complete separation between the adherents, is easy to evaluate. This assumption about the shear strength is very common in the numerical simulations, given that the real relation between the shear strength and the yield strength is uncertain [74].

Nevertheless, the stiffness of the elastic branch is unknown if the slip corresponding to the shear strength is unknown. Through the FEM model previously described, all the values characterizing the interface law, corresponding to each fracture energy value in function of the conditioning type, were evaluated (Table 15). The fracture energy values relating to the absorption are only considered in the following.

Corresponding to the first point of the adhesive layer (notch side) of Figure 31, each interface law was built recording all the shear stress values increasing the displacement monotonically.

In Figure 41, all the interface laws for both the resins as well as for the unaged and aged condition are depicted.

It is worth noting that in general the slip corresponding to the shear strength is very little compared to the ultimate one (about 1/100).

Furthermore, in order to validate the FEM model in terms of the fracture propagation, a comparison between the experimental and numerical results was performed. Within this scope, referring to Figure 42, the trend of the maximum shear stresses was depicted in function of the adhesive layer length. For each kind of resin under investigation, referring also to the unaged condition, the part of the adhesive layer where shear stresses reached the limit value was investigated. It resulted 60 mm for SikaDur 30 (for a total of 120 mm) and 70 mm for Araldite (for a total of 140 mm). For several nodes (points P1-P5 of Figure 43) positioned inside this part of the adhesive layer, the conjugated interface laws were evaluated as depicted in Figure 44. As expected, corresponding to Point 5, for which the shear limit stress was not reached, the relative fracture energy was lower than the maximum one ( $G_{II,P_u}$ ). From Table 16, it is possible to observe a good agreement with the experimental results (CBBM method).

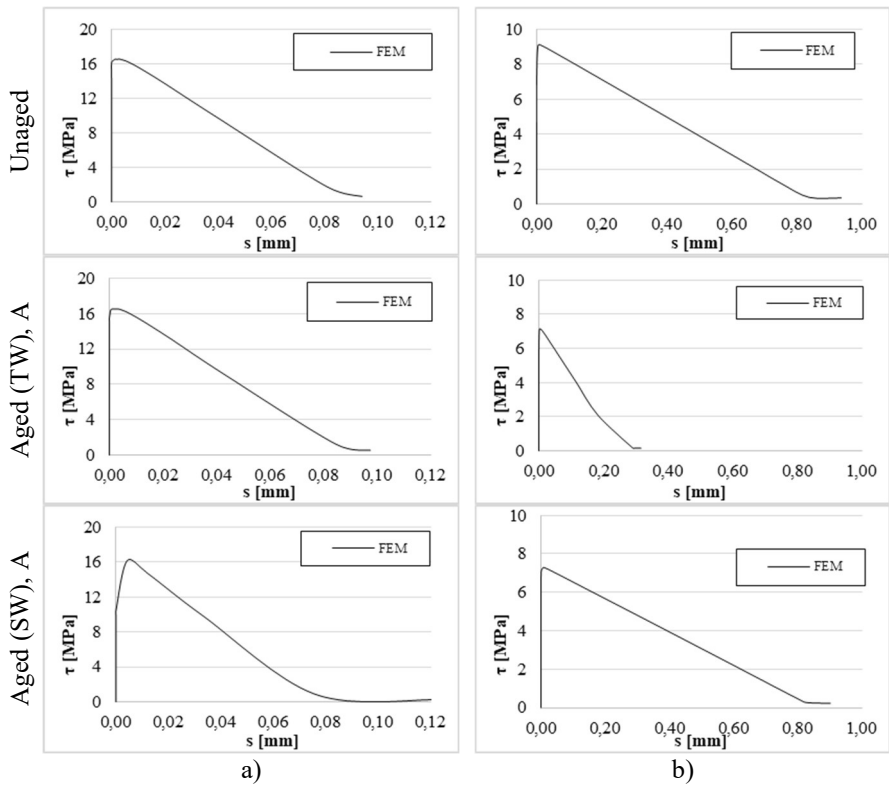
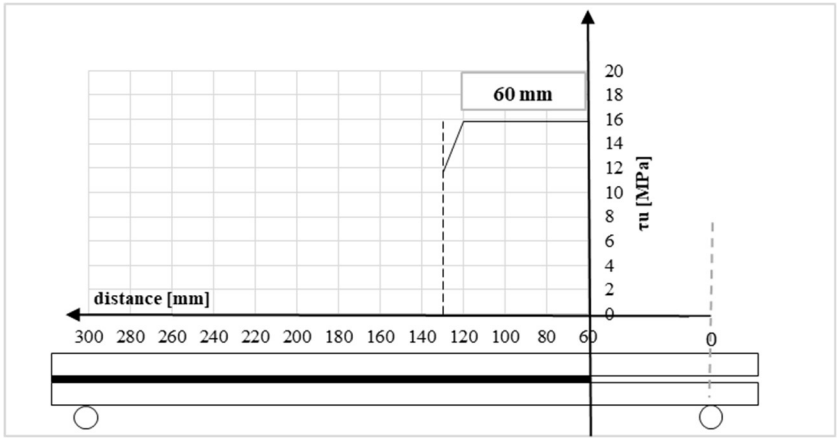
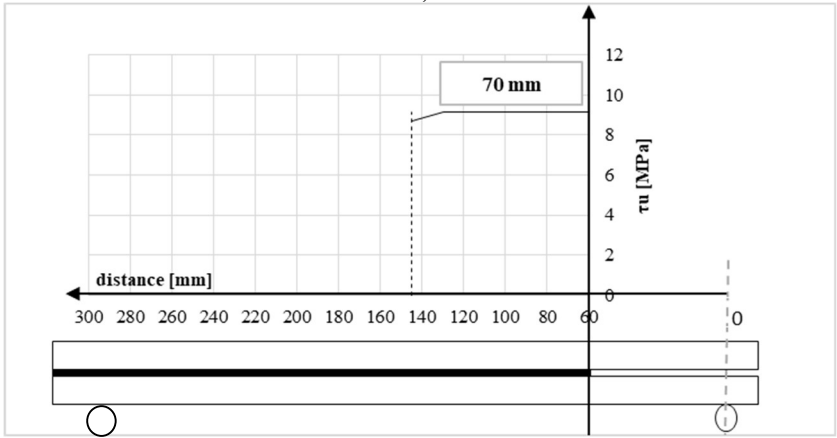


Figure 41. Complete interface law  $\tau$ - $s$  for the case of absorption: a) SikaDur30; b) Araldite.

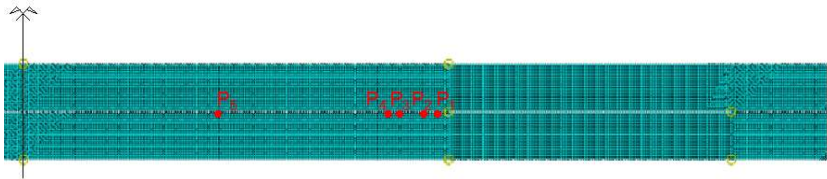


a)



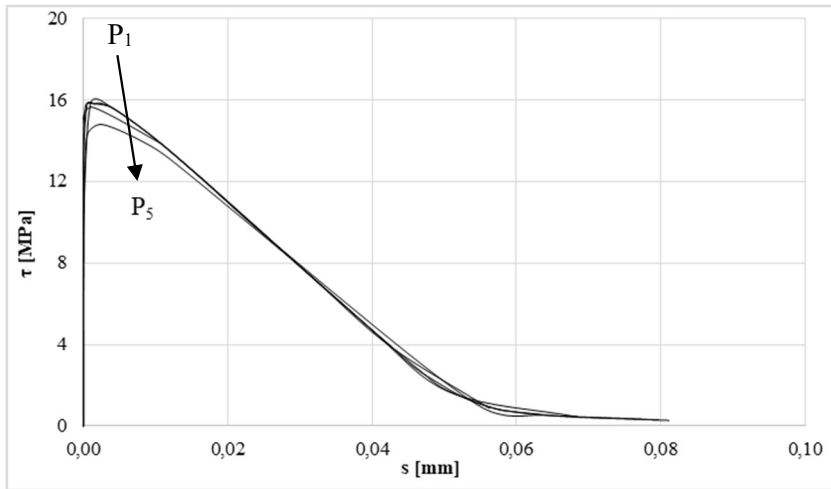
b)

Figure 42. Fracture propagation: a) SikaDur30; b) Araldite.

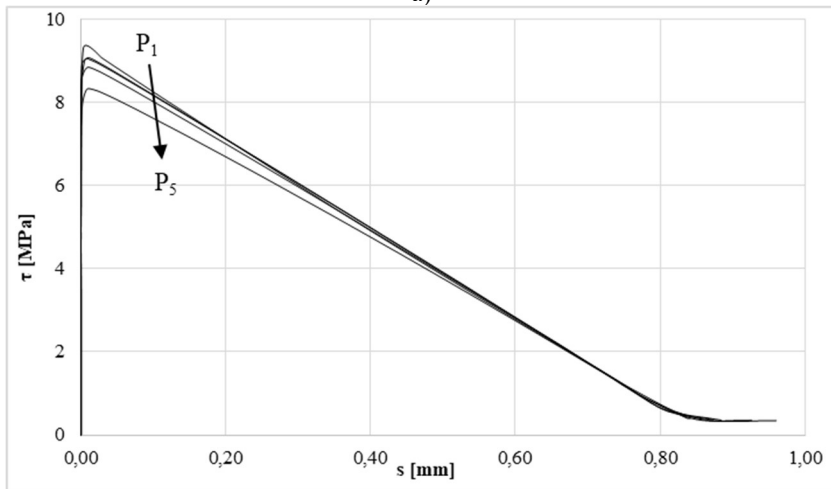


	P1	P2	P3	P4	P5
Distance [mm]	62	65	70	75	140

Figure 43. Points investigated corresponding to the reaching of the shear strength limit value.



a)



b)

Figure 44. Interface laws for all points were shear strength reached the limit value: a) SikaDur30; b) Araldite.

Table 16. Fracture propagation zone: experimental-numerical comparison.

	CBBM method		FEM	
	SikaDur30	Araldite	SikaDur30	Araldite
$a_{,eq}$ [mm]	95	115	120	140

As previously discussed, three different values of the fracture energy were experimentally determined. Among them, the value of the fracture energy

called  $G_{II,P_{nl}}$ , is the most interesting one since it represents the level of the fracture energy dissipated which corresponds a linear elastic behaviour of the P- $\delta$  curve of the ENF test. Furthermore, corresponding to this fracture energy value, it was demonstrated that when the equivalent crack length,  $a_e$ , coincides with the initial crack,  $a$ , then no damage occurred in the adhesive. This last circumstance is of absolute importance in view of structural applications in all the fields of engineering in general in that of civil engineering.

In order to design and verify a safe adhesive connection, it is necessary to known not only the aforementioned fracture energy,  $G_{II,P_{nl}}$ , but also the conjugated slip at the interface, called  $s_{nl}$ . Within this aim, an analytical expression, in function of  $G_{II,P_{nl}}$  and  $s_u$  only, is presented according to the symbols of Figure 45.

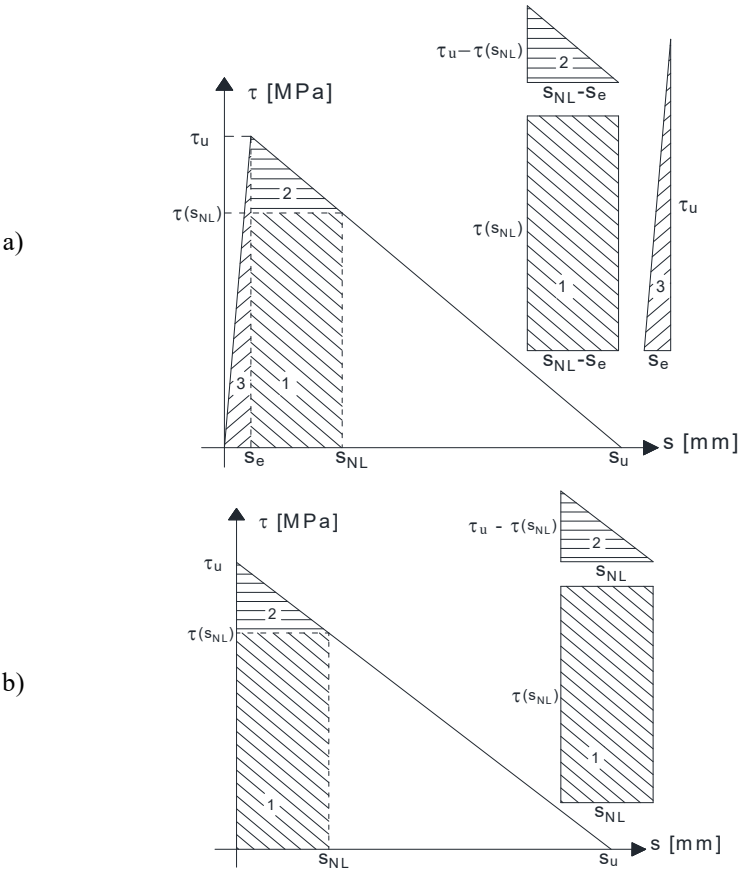


Figure 45. Evaluation of  $s_{nl}$ : a) bilinear law; b) simplified rigid-softening law.

Eqs. (23-25) refer to the case of the interface bilinear law. In this case, the unknown slip ( $s_{nl}$ ) is a function of: 1) the slip ( $s_e$ ) at the end of the elastic stage, 2) the ultimate slip ( $s_u$ ) and 3) the fracture energy  $G_{II,P_{nl}}$ . Considering the low values of the slip  $s_e$ , as already commented before ( $s_e \approx \frac{s_u}{100}$ ), it could be useful to refer to the simplified interface law of Figure 27b where the elastic stage is neglected. In this case, the unknown slip ( $s_{nl}$ ) is a function of the ultimate slip ( $s_u$ ) and the fracture energy  $G_{II,P_{nl}}$  only.

$$\tau(s) = \tau_u - \frac{\tau_u}{s_u - s_e}(s - s_e) \text{ if } s_e \leq s \leq s_u \quad (23)$$

$$\begin{aligned} G_{II,P_{nl}} &= G_{II,P_{nl}}^{(1)} + G_{II,P_{nl}}^{(2)} + G_{II,P_{nl}}^{(3)} = \\ &= \frac{s_e \tau_u}{2} + \tau_{s_{nl}} \cdot (s_{nl} - s_e) + \frac{(\tau_u - \tau_{s_{nl}})(s_{nl} - s_e)}{2} \end{aligned} \quad (24)$$

$$s_{nl} = s_u - \sqrt{(s_u - s_e) \left( s_u - 2 \frac{G_{II,P_{nl}}}{\tau_u} \right)} \quad (25)$$

$$\tau(s) = \tau_u - \frac{\tau_u}{s_u} s \text{ if } 0 \leq s \leq s_u \quad (26)$$

$$G_{II,P_{nl}} = G_{II,P_{nl}}^{(1)} + G_{II,P_{nl}}^{(2)} = \tau_{s_{nl}} \cdot s_{nl} + \frac{(\tau_u - \tau_{s_{nl}}) s_{nl}}{2} \quad (27)$$

$$s_{nl} = s_u - \sqrt{s_u \left( s_u - 2 \frac{G_{II,P_{nl}}}{\tau_u} \right)} \quad (28)$$

In Table 17, an evaluation of the slip  $s_{nl}$  is performed according to Eqn. (25) and (28) for both types of epoxy resin under investigation. It is worth remembering that the third column is relative to the ultimate slip,  $s_u$ , evaluated by dividing the fracture energy by the competent shear limit stress. It is possible to conclude that the choice of the simplified rigid-softening law is largely justified.

Table 17. Evaluation of the slip  $s_{nl}$  by Eqn (25) and (28).

SikaDur 30	$G_{II,P_{nl}}^{CBBM}$	$G_{II,P_u}^{CBBM}$	$s_u$	$s_{nl}^{(25)}$	$s_{nl}^{(28)}$
	[N/mm]	[N/mm]	[mm]	[mm]	[mm]
Unaged	0.38	0.58	0.05800	0.03378	0.03365
Aged (TW)	0.39	0.81	0.08100	0.02858	0.02829
Aged (SW)	0.31	0.69	0.06900	0.02256	0.02228
Araldite	$G_{II,P_{nl}}^{CBBM}$	$G_{II,P_u}^{CBBM}$	$s_u$	$s_{nl}^{(25)}$	$s_{nl}^{(28)}$
	[N/mm]	[N/mm]	[mm]	[mm]	[mm]
Unaged	0.59	4.10	0.82000	0.07138	0.06767
Aged (TW)	0.23	0.92	0.23000	0.03584	0.03470
Aged (SW)	0.59	3.28	0.82000	0.08895	0.08533

## 2.2. Conclusions

The experimental results obtained were compared with those of a numerical modelization where a bilinear interfacial law was adopted. The numerical model was able to consider the variation, in terms of shear strength and the relative displacement (sliding) between the adherents, due to absorption and desorption phenomenon.

Finally, in order to have a safe design of a bonded joint, a new lower value of the fracture energy was introduced with respect to the classical one. It refers to the end of the elastic stage in the load-displacement curve of the ENF test of the joint specimen. The corresponding sliding value was evaluated through a simple numerical equation proposed.

# **CHAPTER III: Study of the flexural and shear behaviour of the full beam-to-column adhesive connections with particular regards to the influence of the bonded area, the load condition and hygro-thermal aging**

## **3. Introduction**

In this chapter the experimental program, which involves the realization and laboratory testing of thirty full scale glass fiber reinforced polymer (GFRP) connections composed of a square hollow section, acting as a column, connected to a built-up beam made of two U-profiles by means of the epoxy resin, are presented and discussed. The influence of several parameters, such as the extension of the bonded area, the load condition and hygro-thermal aging on the global mechanical response of beam-to-column adhesive joints were studied with particular attention. The beam-column assembly formed an L-shaped frame tested by applying a point load at the beam free end (bending) and close to the column (shear), while the column was fixed at its base. Furthermore, five different bonded area configurations were considered and tested, with two different aging conditions being taken into account: conditioning in Tap Water and Sea Water for one year at the constant temperature of 30°C. All the tests were conducted at the STRuctural ENGeering Testing Hall (STRENGTH) Laboratory of the University of Salerno.

### **3.1. Experimental program**

In this experimental program, different joints configurations were studied. The reference configuration is characterized by the joining of Triglass<sup>®</sup> tubular column made of a GFRP profile with a square cross section (90mm × 90mm × 8mm) and two U-profiles (150mm × 45mm × 8mm) arranged together in the form of a built-up beam. Both the beam and the column are 500 mm long. Four angle profiles (60mm × 60mm × 5mm) were positioned at the bottom and the top of the two U-profiles in order to increase the bonded area in the connection zone only. Furthermore, to minimize the possible lateral buckling, the two U-profiles were also connected to each other

at their free ends by means of a 100 mm long square tube (90mm × 90mm × 8mm) inserted between the two profiles and bonded to them. All the GFRPs pieces, produced and furnished by Top Glass Industries S.p.A (Italy), are depicted in Figure 46a, while in Figure 46b, the assembled beam-to-column joint is presented. The adhesive thickness was typically 1 mm.

The goals of this experimental investigation were to evaluate the influence on the global mechanical response of the joint of:

- the bonded area extension;
- the type of the load;
- the hygro-thermal aging.

A total of thirty beam-to-column connections were realized and tested under quasi-static loads. The specimens were classified into 3 different groups as shown in Table 18. In the first group (A), the beam was subjected to bending and shear (the load is applied at the free end of the beam, see Figure 46c); in the second group (B), the beam was subjected to shear only (the load is applied as close as possible to the column, see Figure 46c); finally, in the third group (C), the connections were firstly conditioned and after tested under bending conditions only. In detail, the ageing was an immersion period of one year in Tap Water (TW) and Sea Water (SW) at a temperature of 30 °C. The latter was set according to the guidelines of CEN/TC 250 [9], where it is suggested considering an operating temperature of at least 20 degrees lower than the glass transition temperature ( $T_g$ ). In the case of the epoxy resin adopted, Araldite AV 5308 produced Huntsman Adv. Materials (Switzerland), the  $T_g$  was evaluated to be equal to 67°C [21].

Table 18. Experimental program

Group	#	Load	Ageing
A	17	Bending+Shear	-
B	4	Shear	-
C	3+3	Bending+Shear	TW - SW

Total 30

The epoxy resin Araldite was selected in order to characterize, from a mechanical point of view, the behavior of the above mentioned beam-to-column joints, similar to those previously fabricated and tested by means of SikaDur 30 resin [13]. The Araldite resin is characterized by an initial linear elastic behavior followed by a plastic zone leading to a global ductile behavior. On the contrary, the SikaDur30 presents a linear elastic behavior up to failure. Furthermore, the Araldite has a different curing degree with respect to the

SikaDur30, leading to a shorter curing step, certainly more suited to the needs of an application in the field of civil engineering.

Finally, the other symbols introduced in Figure 46c assumed the following meaning:  $b$  and  $h$  are the horizontal and vertical dimensions of the rectangular adhesive area, respectively;  $d_a$  and  $d_b$  are the distances between the load application points (relative to Group A and B, respectively) and the vertical centroid axis of the adhesive area (in the case of Figure 46c, it is coincident with the vertical centroid axis of the column).

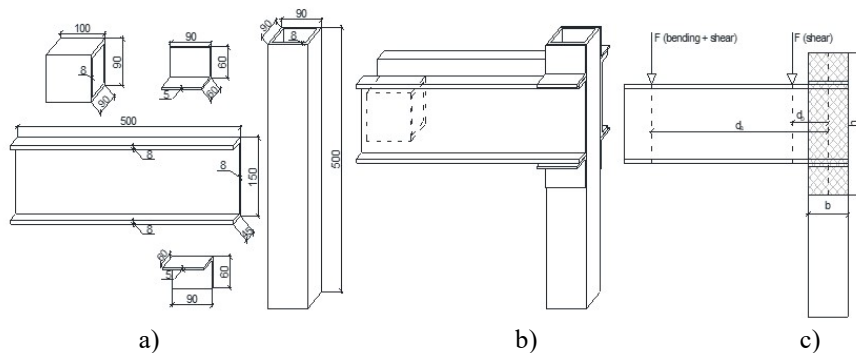


Figure 46. Specimen: a) dimension; b) assembly; c) load for type 1 and 2 and glued area.

### 3.1.1. Materials

In this experimental program it was used Araldite AV 5308 (Hardener HV 5309-1) [60] produced by Huntsman Adv. Materials (Switzerland) and furnished by the Emanuele Mascherpa SpA (Italy), for the characteristics see the subsection 1.1.1 of Chapter 1.

The curing step is fundamental when the epoxy resin is used for any kind of application. The mechanical properties, in terms of the strength and the stiffness, are function of the temperature and the time. In detail, for any curing temperature the corresponding maximum values of the mechanical properties are reported in the technical datasheet furnished by the supplier (Table 5). To reach the above mentioned maximum values is necessary a fixed curing time furnished by the supplier too (lower is the temperature, longer is the time). The two variables mentioned, the temperature and the time, have to be taken into consideration with respect to the field of application when the resin is chosen. In the present experimental program, which falls in the field of the civil engineering, the Araldite was chosen because it is a cold curing temperature resin, suitable for applications for which is not possible to cure the sample

inside a climate chamber (generally very high temperature are requested to reach to top of the performance, ranging between 40°C and 150°C). It has been set a temperature of 21°C ± 2°C, for which it is necessary a curing time of about 24 hours. This level of temperature simulates the real practice condition of an application during the spring/summer period. Finally, cold curing temperature resins are suitable for applications where it is allowed the contact with the water, as in the present experimental program, because of the water temperature, if higher than that of the curing step, activate a benefic post-curing step for the resin as shown in [69].

The Triglass<sup>®</sup> GFRP material used in this study is composed of a polyester matrix and glass fibers. The material was produced and furnished by Top Glass Industries S.p.A. (Italy) [77]. Its mechanical properties are summarized in Table 19 where the values have a tolerance of about 10% as declared by the supplier.

Table 19. Mechanical parameters of the Triglass® material.

Property	Regulations	Unit of measure	Average values
Specific weight	ASTM D792	g/cm <sup>3</sup>	1.75-1.90
Dielectric strength	ASTM D149	kV/mm	3-7
Water absorption	ISO 62	%	0.4
Surface electrical resistivity	EN 61340	Ω	1012
Loss Factor 50 HZ (tg d)	ASTM D150	-	0.05
Thermal class	-	CLASS	F
Coefficient of linear thermal expansion	ISO 11359-2	K <sup>-1</sup>	8-11 x 10 <sup>-6</sup>
Thermal conductivity	EN 12667 / EN 12664	W/mK	0.3
Longitudinal flexural strength	ASTM D790	MPa	300 – 500
Modulus of elasticity in longitudinal bending	EN 13706	GPa	22 – 28
Longitudinal tensile strength	ASTM D638	MPa	300 – 500
Modulus of elasticity with longitudinal traction	ASTIM D638	GPa	22 – 28
Longitudinal compressive strength	ASTM D695	MPa	180 – 300
Elastic module with longitudinal compression	ASTM D695	GPa	16 – 20
Fire resistant	UL 94	CLASS	HB
Shear resistance	ASTM D2344	MPa	30

### 3.1.2. Specimen designation and fabrication

The three different groups represented in Table 18 were further subdivided as described in detail below. Group A was divided into five sub-groups (from A.1 to A.5) in order to study the influence on the global mechanical response of the joint of the bonded area extension: 1) reducing the gluing area in terms of the base  $b$  only with GFRP elements having the same dimensions (Groups A.1, A.2 and A.3); 2) reducing the gluing area in terms of height  $h$  by neglecting the angles (Group A.4); 3) increasing the gluing area by considering a column with a bigger cross section dimension (120x120 mm) with respect to the reference configuration (Group A.5). For each subgroup, the corresponding joint configuration realized is depicted in Figure 47. Furthermore, photos of the specimen realized are in Figure 48. In detail, in Figures 47a-c, the height  $h$

of the bonded area was fixed and equal to 270 mm while the base  $b$  varied (90, 65 and 40 mm). The value of the arm  $d_a$  introduced in Figure 46, varied as highlighted in Figure 47a-c (it is worth to remember that  $d_a$  is the distance between the load application points and the vertical centroid axis of the adhesive area).

The joints in Figures 47d-e are those of Figure 47a (reference configuration) but without the angles and with a different column cross section, respectively. Group B was not subdivided since only the shear load condition was considered. The specimen configuration tested was the reference one with the load  $F$  applied as close as possible to the column.

Finally, Group C was divided into two subgroups so as to consider the two different ageing conditions: Tap Water (Group C1) and Sea Water (Group C.2). The type of the specimen tested was the reference one (Group A.1).

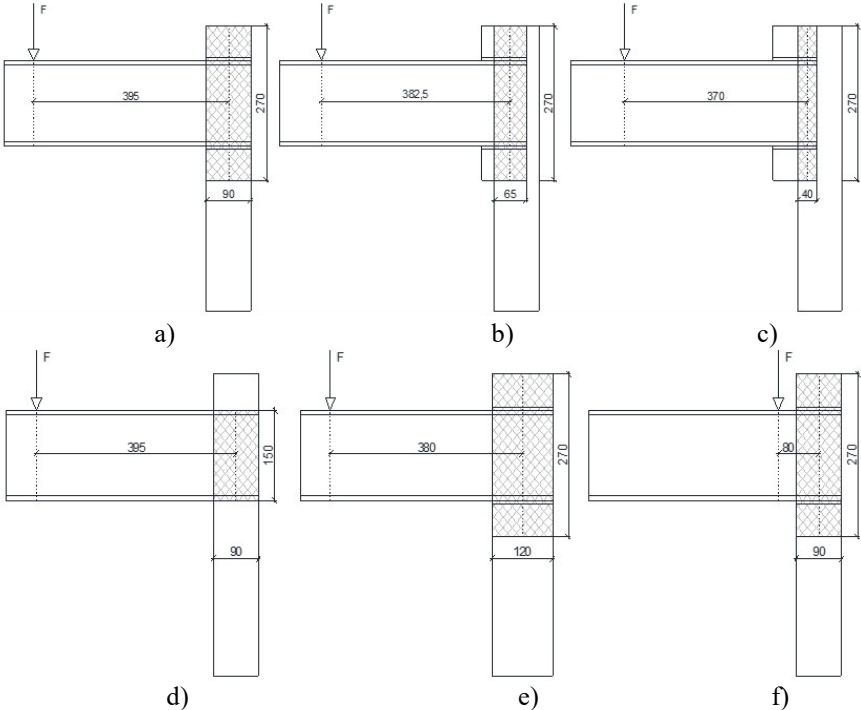


Figure 47. Variation specimens: a) Group A.1; b) Group A.2; c) Group A.3; d) Group A.4; e) Group A.5; f) Group B.

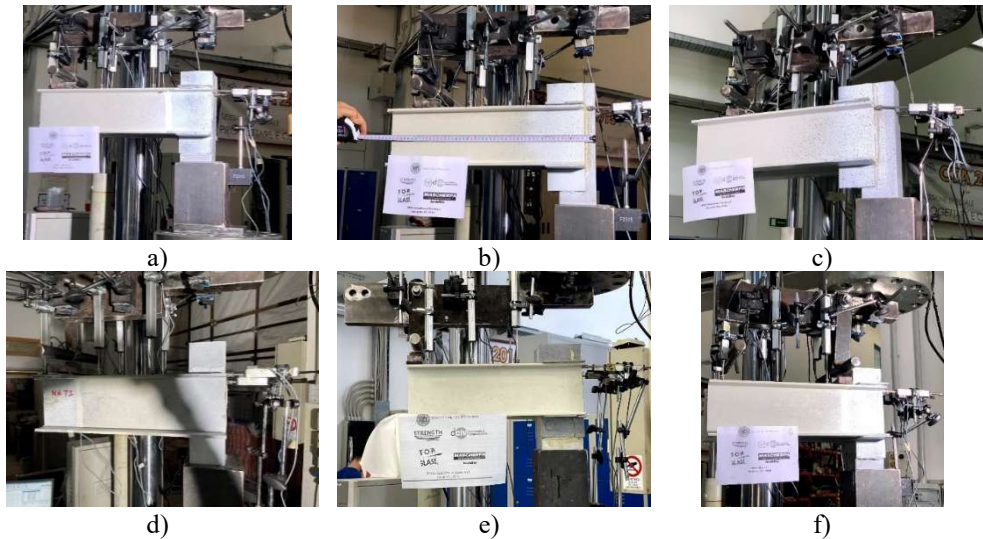


Figure 48. Photos of the specimens realized: a) type A.1; b) type A.2; c) type A.3; d) type A.4; e) type A.5; f) type B.

All the subgroups introduced are summarized in Table 20. The number of tests conducted, the dimensions ( $b$  and  $h$ ) of the rectangular bonded area, the type of load applied (in terms of stresses induced into the beam), the value of the arm  $d_a$  or  $d_b$  and the type of ageing considered are reported for each subgroup.

Table 20. Specimens designation.

Type	#	b [mm]	h [mm]	Type of load	$d_a$ ( $d_b$ ) [mm]	Ageing
A	A.1	4	90	Bending+Shear	395.0	-
	A.2	4	65	“	382.5	-
	A.3	4	40	“	370.0	-
	A.4	4	90	“	395.0	-
	A.5	4	120	“	380.0	-
B	-	4	90	Shear	(80.0)	-
C	C.1	3	90	Bending+Shear	395.0	TW
	C.2	3	90	“	395.0	SW
Total	30					

In Figure 49, all the steps relating to the fabrication of the specimens are reported. All the GFRP pieces and the bi-component resin are depicted in detail in Figure 49a. Figure 49b shows the part of the GFRP which was first grit blasted using a sandpaper and then degreased with acetone prior to the application of the adhesive. Figure 49c shows a photo of the gluing process. It is worth highlighting how all the GFRP pieces were glued to each other in the

same time interval in order to avoid both any significant variations in the environmental condition as well as inconsistencies between the different adhesive mixtures. Furthermore, the bond-line thickness was nominally 1 mm. Spacers (calibrated steel bars of 1 mm in diameter) were inserted between the adherents before the application of the adhesive in order to control the adhesive thickness (Figure 49d).

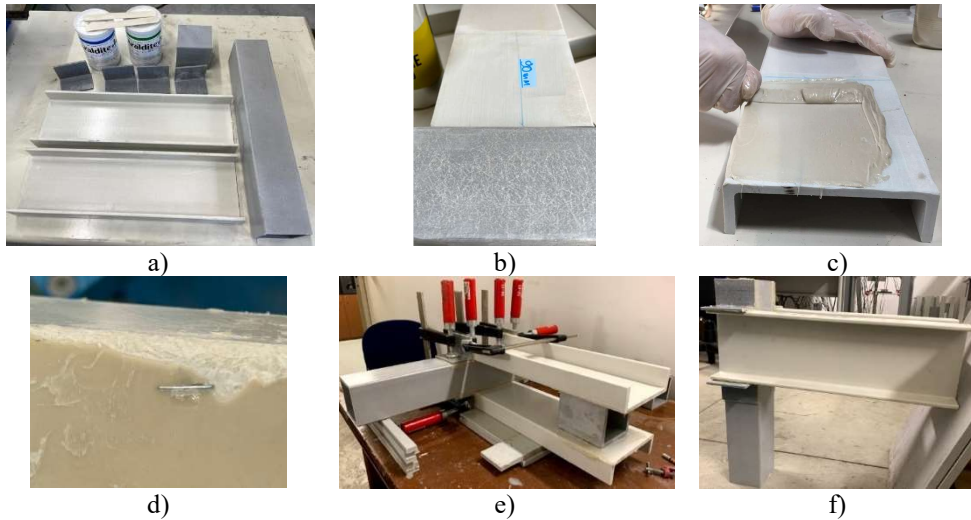


Figure 49. Specimen fabrication steps: a) resin and GFRP pieces; b) GFRP roughened and degreased; c) gluing process; d) steel bars spacers; e) checking the adherents alignment; f) specimen after curing ready to be tested.

After having checked the alignment between the adherents by means of clamps (Figures 49e), the specimens were cured for 24 hours at room temperature (RT, 23°C) according to the technical data sheet. Regarding the temperature of the curing stage, the room temperature was chosen to simulate as much as possible the conditions of real use.

Finally, Figure 49f shows the specimen at the end of the curing process ready to be tested.

### 3.1.3. Hygrothermal conditioning

The experimental apparatus used for conditioning the beam to column connection was the same introduced in chapter 1.1.4. for the SLJ. It consists of two separate plastic boxes containing Sea Water (SW) and Tap Water (TW) as depicted in Figure 50a, respectively, both at a constant temperature of about

30°C served by the immersion heater of Figure 50b. The salinity, temperature and pH of the seawater were continuously recorded by a redoximeter HI9829 (Figure 50c) and their distributions over the time are presented in Figure 51. For the sake of clarity, any oscillations in temperature and salinity are justified by the need to add cold water in order to maintain the salinity in the range 36-39 PSU (typical values) due to evaporation phenomenon.

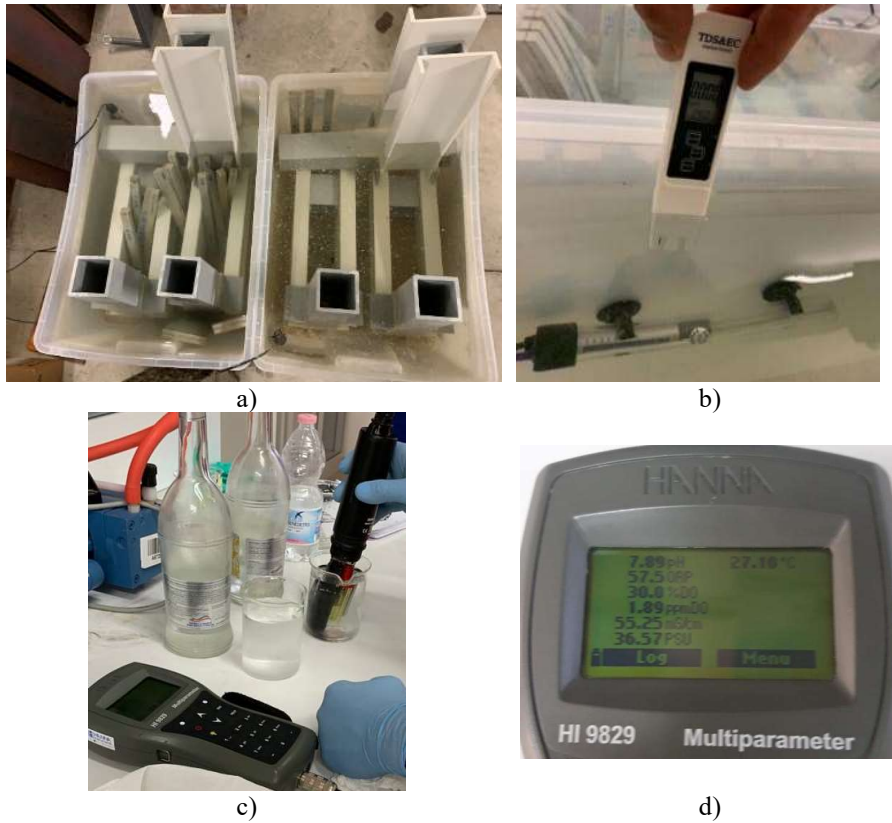


Figure 50. Photos of the environmental exposure set-up: a) plastic boxes for SLJ specimens; b) immersion heater and thermometer; c) redoximeter. d) values measurement redoximeter.

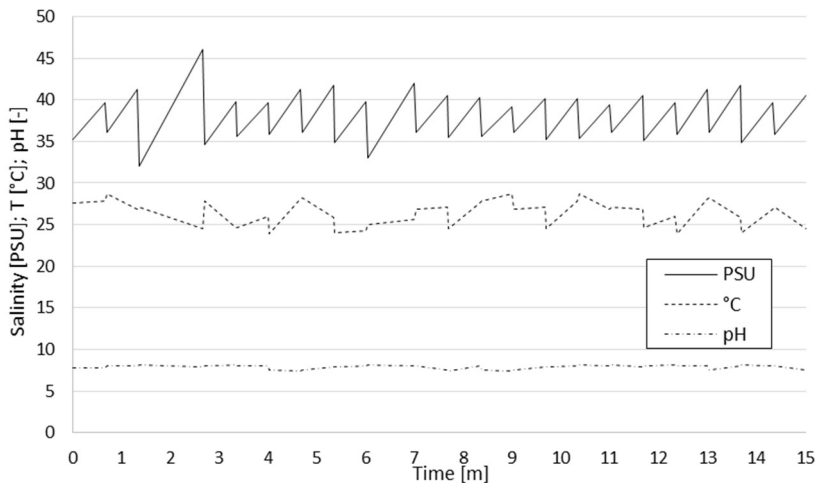


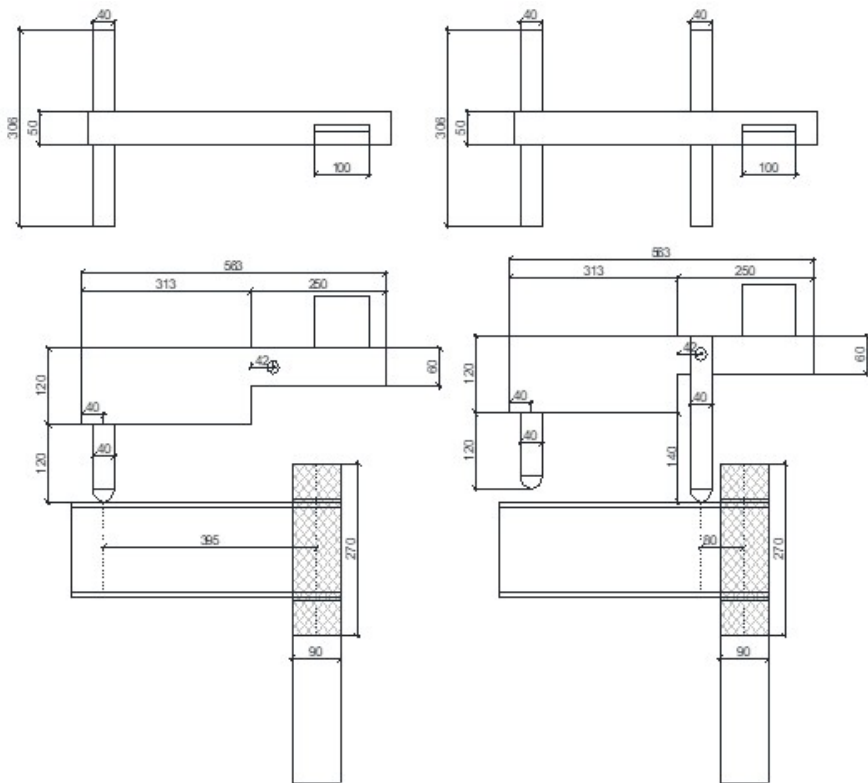
Figure 51. Sea water parameters. Graphs of the salinity (PSU), the temperature (°C) and the pH vs time.

Regarding the tap water, it was continuously monitored the temperature (average value of 27.95 °C) and the pH (average value of 7.72).

### 3.1.4. Experimental set-up

Each specimen was loaded by a point load applied close to the free end of its built-up beam (Group A) or close to the column (Group B) by means of a rigid steel arm clamped to the Schenck Hydropuls servo-hydraulic testing machine. The column was inserted into a steel jacket. Therefore, it can be assumed fixed at its basis, with its unsupported length being 300 mm. The static tests were performed in displacement control at a rate of 2 mm/s.

The test set-up is schematically illustrated in Figure 52 where it shows how the load was applied to the beam for both load conditions relating to Group A (Figure 52a) and to Group B (Figure 52b). The specimen illustrated in Figure 52a is the reference one (Group A.1). The vertical steel arm, bolted to the horizontal one in order to apply a shear force (Group B), was removed when the load had to be applied at the free beam end (Group A) as depicted in Figure 52.



a) b)  
 Figure 52. Steel rigid arm to apply the load: a) type A (bending+shear); b) type B (shear).

In Figure 53, there is a detailed description of the steel jacket. Its internal free dimensions are 120 mm x 120 mm (used in [71]). In order to insert in it the square column here adopted (90 mm x 90 mm), the other three steel elements of Figure 53 were added to the original system.

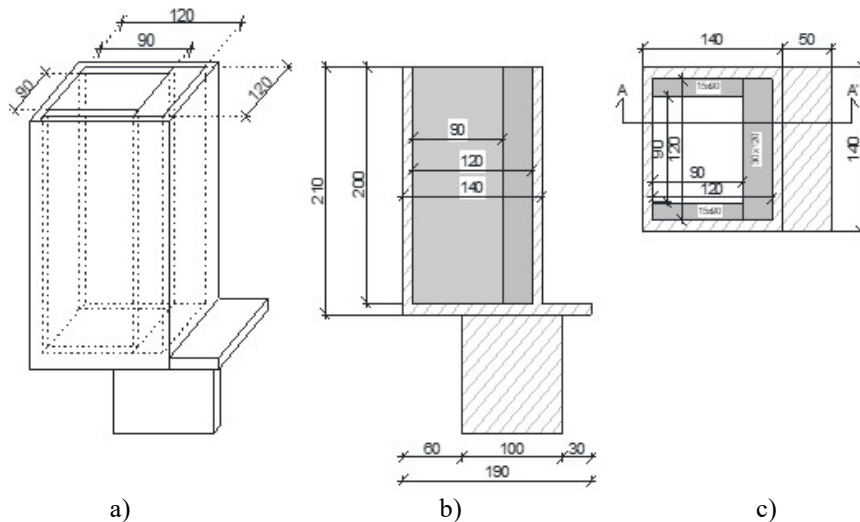


Figure 53. Steel jacket: a) 3D view; b) lateral view; c) top view.

In order to measure the vertical and horizontal displacements of the specimen nine linear variable displacement transducers (LVDT) were used. Six of them were placed on the built-up beam (three per each U-profile), as described in Figure 54a, in order to evaluate the vertical displacement of the beam (and its elastic deformation) as well as check the alignment between the U-profiles. An additional three LVDTs were placed horizontally as described in Figure 54b in order to evaluate the relative displacements between the column and the beams. The latter were divided by the beam height in order to evaluate the relative rotation between the column and each of the two U-profile. The final value of the beam-to-column relative rotation was the average one. Finally, shims were used in order to reduce the small gap (1 mm) between the column and the steel jacket steel.

Furthermore, a Digital Image Correlation (DIC) system was used (Figure 54c-d) to study the strain-stress rate at the bonded area for both load conditions and to check for possible intermediate fractures in the GFRP material. Speckle patterns were applied by spraying the specimen or component surface with contrasting paints (i.e. black, white and grey) as described in Figure 55.

Load cell data were automatically and continuously recorded by an automatic data acquisition system (System 5100 Vishay MM) with a frequency equal to 10 data per second, while the strains were recorded by a DIC-2D acquisition data system.



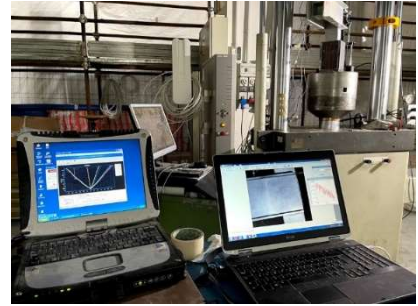
a)



b)



c)



d)

Figure 54. Experimental set-up: a) vertical LVDTs; b) horizontal LVDTs; c) DIC; d) data acquisition system.



Figure 55. Spackle pattern preparation.

### 3.2. Experimental results

This section discusses all the experimental results relating to the strength and the stiffness of the specimens tested. Two different types of graphs were considered: load–displacement ( $F-\delta$ ) and moment-rotation ( $M-\theta$ ).  $F$  is the force applied at the free end of the built-up beam,  $M$  is the corresponding bending moment evaluating the centroid vertical axis of the bonded area,  $\delta$  is the displacement evaluated at the same cross section where the load is applied and  $\theta$  is the rotation between the beam and the column.

Both the displacement  $\delta$  and the rotation  $\theta$  are the function of the adhesive layer only. The elastic deformation of the GFRP beam and column were neglected. In particular, the elastic deformation of the beam was experimentally evaluated by means of the vertical LVDTs (see section 3.1.4), while that of the column was analytically evaluated by considering the static scheme of a beam fixed at one end and subjected to a bending moment at the

free end. The validity of the static scheme was verified by comparing the analytical displacement at the free end of the beam with the displacement experimentally evaluated by means of the horizontal LVDT applied to the column (Figure 54b).

The section is subdivided into five subsections. In the first three subsections, the influence of the bonded area extension is studied. In the first one (3.2.1), the case in which the dimensions of the glued area varied in terms of the base  $b$  only with GFRP elements having the same dimensions is analysed. The results relating to the specimens of Groups A.1 (reference configuration), A.2 and A.3 are compared.

In the second subsection (3.2.2), the case in which the glued area was reduced (in terms of the height  $h$ ) by neglecting the angles is studied. The results relating to the specimens of Groups A.1 and A.4 are compared.

In the third subsection (3.2.3), the case in which the glued area was increased by considering a column with a bigger cross section with respect to that of the reference configuration is analyzed. The results relating to the specimens of the Groups A.1 and A.5 are compared.

In the fourth subsection (3.2.4), the influence of the load conditions (bending, shear) on the mechanical response of the joint is highlighted. The results relating to the specimens of Groups A.1 and B are compared.

Finally, in the last subsection (3.2.5), the influence of hygro-thermal conditioning on the strength and stiffness of the reference specimen (Group A.1) is presented. The results relating to the specimens of Groups A.1, C.1 and C.2 are compared.

### 3.2.1. Influence of the bonding area extension: variation of the bonded area in terms of the base $b$

This subsection discusses the influence of the glued area on the strength and stiffness of the beam-to-column joint under investigation. In this case, the variation of the glued area, as previously mentioned, consists of the variation of the base  $b$  only of the bonded area from 90mm to 45 mm passing through 65 mm (see Figures 47a-b-c).

As already introduced in the previous section, the results are presented in Figure 56 (graphs F- $\delta$  and M- $\theta$ ) and in Table 21. The following information is reported for each test:  $F_{\max}$  is the peak load,  $\delta$  is the corresponding relative displacement evaluated at the same cross section (see section 3.1.4),  $\mu$  are the average values,  $\sigma$  are the standard deviation values,  $d_a$  is the arm of the applied

force  $F$  with respect to vertical centroid axis of the bonding area,  $M_t$  is the bending moment ( $F \times d_a$ ),  $\theta$  is the relative rotation (see section 3.2) between the beam and the column.

From the graphs, it is possible to observe that in general the global behaviour of the joint could be considered linear elastic until failure as for GFRPs in general. At the end of each curve, a possible non-linear trend could be observed due to the non-linearity of the adhesive (non-linearity of GFRP was experimentally observed for a higher load level as reported in detail in the next section 3.2.4).

Furthermore, it is possible to observe that the stiffness is the same in all the cases under investigation, while the strength varied, being the function of the bonded area extension. The maximum strength decrement (15%), between Groups A.1 and A.3, was not linear with respect to that of the bonded area (50%).

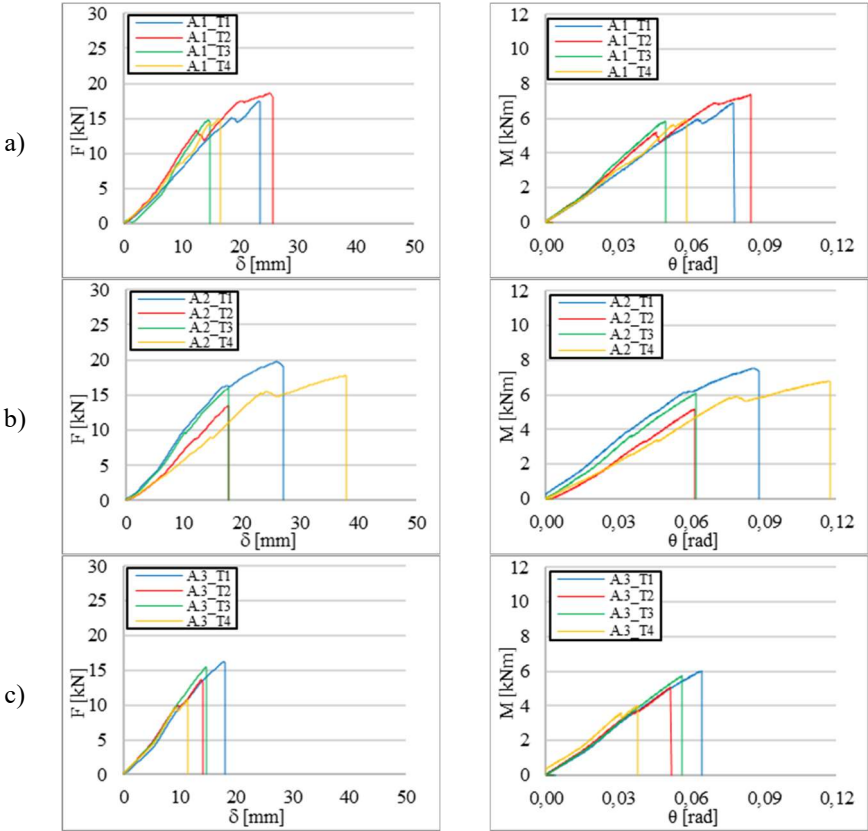


Figure 56.  $F$ -  $\delta$  and  $M$ -  $\theta$  graphs: a) and d) Group A.1; b) and e) Group A.2; c) and f) Group A.3.

Table 21. Results of Groups A.1, A.2 and A.3.

Group	Test	$F_{exp}$ [kN]	$\delta_{v,conn}^{exp}$ [mm]	$\mu$		$\sigma^2$		$M_{exp}$ [kNm]	$\theta_{v,conn}^{exp}$ [rad]	$\mu$		$\sigma^2$	
				$F_{exp}$ [kN]	$\delta_{v,conn}^{exp}$ [mm]	$F_{exp}$ [-]	$\delta_{v,conn}^{exp}$ [mm]			$M_{exp}$ [kNm]	$\theta_{v,conn}^{exp}$ [rad]	$M_{exp}$ [kNm]	$\theta_{v,conn}^{exp}$ [rad]
A.1	1	17.47	23.41					6.90	0.078				
	2	18.67	25.69	16.48	20.14	0.04	0.20	395	7.38	0.085	6.51	0.068	0.19
	3	14.77	14.77										
	4	15.03	16.71										
1	19.71	27.20											
A.2	2	13.54	17.63	16.73	25.12	0.07	0.45	383	5.18	0.061	6.40	0.082	0.31
	3	15.92	17.60										
	4	17.73	38.05										
	1	16.23	17.91										
A.3	2	13.68	14.14	14.06	14.53	0.09	0.10	370	5.06	0.052	5.20	0.053	0.13
	3	15.50	14.71										
	4	10.85	11.37										

$\mu$  (average);  $\sigma^2$  (standard deviation)

For the joint relating to Group A.1 (assumed as the reference joint), the failure was mixed between the adhesive and the GFRP material as reported in Figure 57 (starting in the adhesive and after propagating to the cover surface, mat, of the GFRP). The same happened for the joint relating to Group A.2 as shown in Figure 58.



Figure 57. Mixed failure between resin and GFRP for the joint configuration of Group A.1.



Figure 58. Mixed failure between resin and GFRP for the joint configuration of Group A.2.

For the joint configuration relating to Group A.3, on the contrary, the failure was mainly cohesive (in the resin) as depicted in Figure 59. This could be justified by considering that the influence on the adhesive layer behaviour by the bending moment is predominant with respect to the shear force as demonstrated in the next sections 3.2.4 and 3.3.



Figure 59. Cohesive failure (in the adhesive mainly) for the joint configuration of Group A.3.

### 3.2.2. Influence of the bonded area extension: reduction of the glued area in terms of height $h$ by neglecting the angles

This subsection discusses the influence of the glued area on the strength and stiffness of the beam-to-column joint under investigation but in this case the variation of the adhesive area, as already mentioned before, consists of neglecting the GFRP angles (see Figure 47d). The base  $b$  of the bonding area is fixed and equal to 90mm while its height  $h$  is equal to 150mm.

The results are reported in Figure 60 in terms of the  $F$ - $\delta$  and  $M$ - $\theta$  curves as well as in Table 22 by comparing the results with those relating to the reference joint configuration (Group A.1) where angles were present. The structure of Table 22 is the same as Table 21. From Figure 60, it is possible to observe that the stiffness is not sensitive to the presence of the angles themselves, while the strength decreases almost linearly (from 16 kN to 8 kN) with the decrease of the height  $h$  (from 270mm to 150mm) of the bonded area.

This interesting result is commented at the end of section 3.2.4.

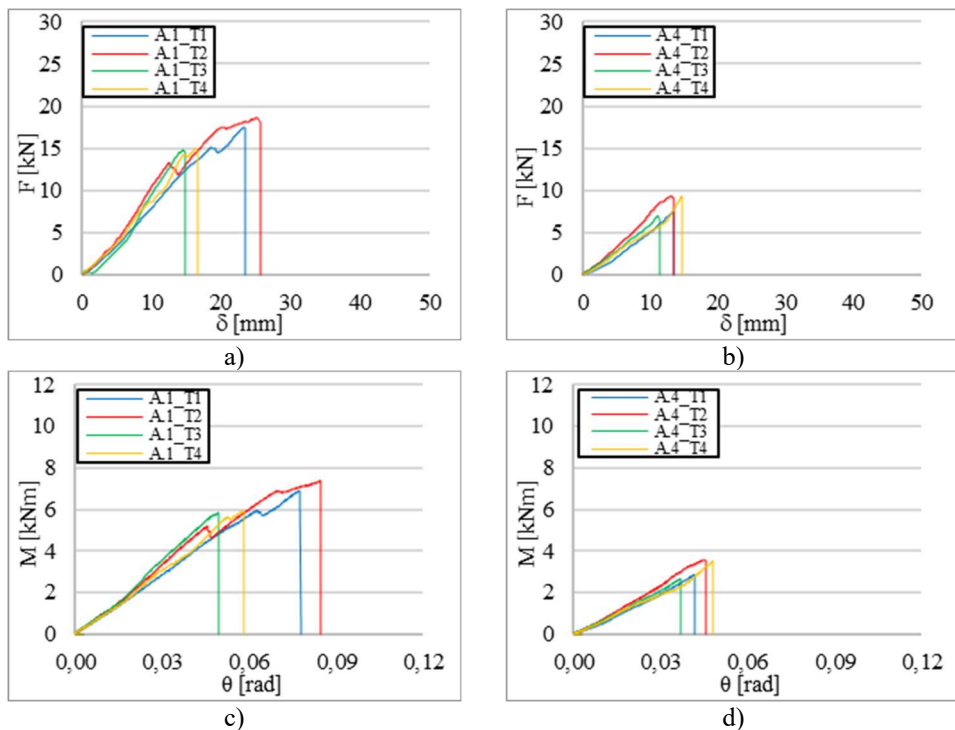


Figure 60.  $F$ - $\delta$  and  $M$ - $\theta$  graphs: a) and c) Group A.1; b) and d) Group A.4.

Table 22. Results of the Groups A.1 and A.4.

Group	Test	$\mu$		$\sigma^2$				$M_{exp}$	$\theta_{v,conn}^{exp}$	$\mu$		$\sigma^2$	
		$F_{exp}$	$\delta_{v,conn}^{exp}$	$F_{exp}$	$\delta_{v,conn}^{exp}$	$F_{exp}$	$\delta_{v,conn}^{exp}$			$\theta_{v,conn}^{exp}$	$\delta_{v,conn}^{exp}$	$\theta_{v,conn}^{exp}$	$\delta_{v,conn}^{exp}$
		[kN]	[mm]	[kN]	[mm]	[-]	[-]	[mm]	[kNm]	[rad]	[kNm]	[rad]	[rad]
A.1	1	17.47	23.41					6.90	0.078				
	2	18.67	25.69					7.38	0.085				
	3	14.77	14.77	16.48	20.14	0.04	0.20	395	5.83	0.049	6.51	0.068	0.19
	4	15.03	16.71						5.93	0.058			
A.4	1	7.47	13.39					2.95	0.042				
	2	9.34	13.45					3.69	0.046				
	3	6.94	11.40	8.25	13.21	0.07	0.03	395	2.74	0.037	3.26	0.043	0.04
	4	9.26	14.59						3.66	0.048			

$\mu$  (average);  $\sigma^2$  (standard deviation)

Furthermore, the failure was mainly cohesive (in the adhesive) as reported in Figure 61, while the GFRP was involved only at the edges of the bonding area.



Figure 61. Cohesive failure (in the adhesive mainly) for the joint configuration of Group A.4.

### 3.2.3. Influence of the bonded area extension: increasing of the glued area by considering a column with a bigger cross section with respect to that of the reference configuration

The last modification in terms of the extension of the bonded area included the increasing of the column section (hollow profile 120mm x 120mm) in order to have an increase of the base  $b$  (120mm) of the adhesive layer (see Figure 47e) with respect to the reference configuration (90 mm).

The results are reported in Figure 62 in terms of the  $F$ - $\delta$  and  $M$ - $\theta$  curves as well as in Table 23 by comparing the results of Group A.5 with those relating to the reference joint configuration (Group A.1). From Figure 62, it is confirmed that the stiffness did not vary in function of the glued area extension (33%) but rather, as expected, the strength increased (54%).

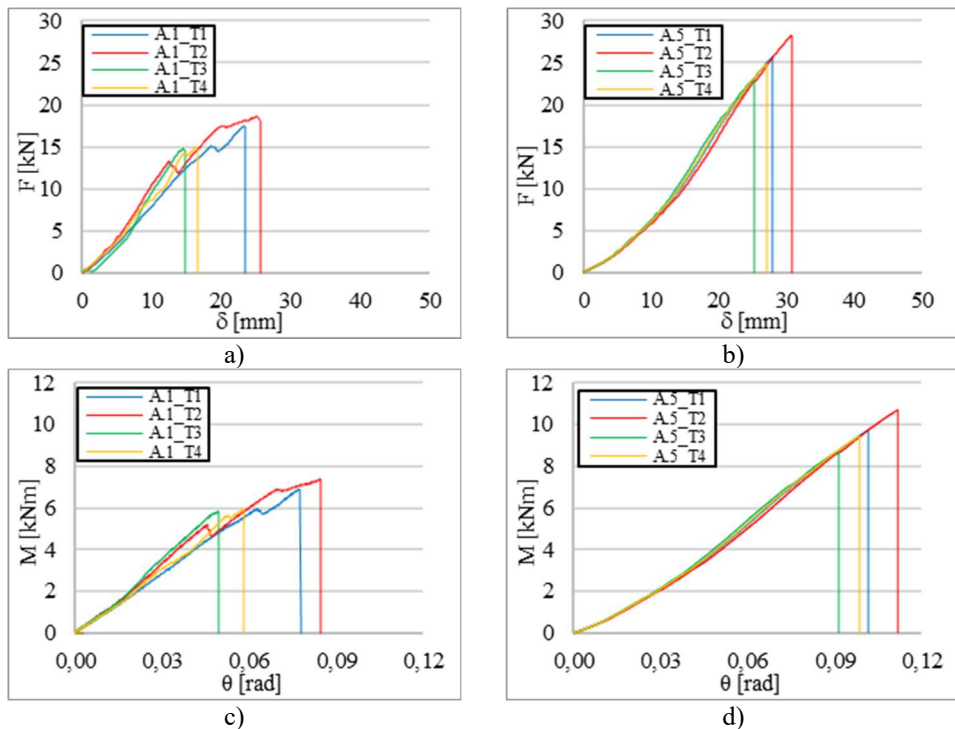


Figure 62.  $F$ - $\delta$  and  $M$ - $\theta$  graphs: a) and c) Group A.1; b) and d) Group A.5.

Table 23. Results of Groups A.1 and A.5.

Group	Test	$\mu$		$\sigma^2$				$M_{exp}$	$\theta_{v,conn}^{exp}$	$\mu$		$\sigma^2$	
		$F_{exp}$	$\delta_{v,conn}^{exp}$	$F_{exp}$	$\delta_{v,conn}^{exp}$	$F_{exp}$	$\delta_{v,conn}^{exp}$			$d$	$M_{exp}$	$\theta_{v,conn}^{exp}$	$\theta_{v,conn}^{exp}$
		[kN]	[mm]	[kN]	[mm]	[-]	[-]	[mm]	[kNm]	[rad]	[kNm]	[rad]	[rad]
A.1	1	17.47	23.41						6.90	0.078			
	2	18.67	25.69						7.38	0.085			
	3	14.77	14.77	16.48	20.14	0.04	0.20	395	5.83	0.049	6.51	0.068	0.19
	4	15.03	16.71						5.93	0.058			
A.5	1	25.66	13.03						9.75	0.102			
	2	28.22	14.33						10.72	0.112			
	3	23.09	11.72	25.46	12.93	0.02	0.02	380	8.77	0.091	9.86	0.101	0.02
	4	24.89	12.64						9.46	0.098			

$\mu$  (average);  $\sigma^2$  (standard deviation)

Finally, the failure was mixed as in the case of Group A.1. This experimental evidence was expected.

### 3.2.4. Influence of the load condition

This section discusses the influence of the load condition. Parallel to the reference configuration where the load is applied at the free end of the beam (with an arm  $d_a$  equal to 395mm), a second load condition was considered where the load was applied as close as possible to the column (with an arm  $d_b$  equal to 80mm). In the second load condition, the beam was only subjected to a shear force. The results are reported in Table 24, and in terms of only the F- $\delta$  curves in Figure 63. It is worth to underlined that the displacement  $\delta$  (for the Figure 63a) was evaluated by means of the vertical couple of LVDTs close to the column (Figure 54a), located at the quite same cross section where the shear load is applied in order to make the comparison reasonable with the case of the Figure 63b where the displacement was evaluated as always (at the same cross section where the load is applied).

In contrast to all the other previous Tables, Table 24 presents the values of the force F relating to the first crack observed in the GFRP material as better clarified in the following.

The influence of the load condition on the mechanical response of the joint is the main and most interesting of all the other influences produced by the several parameters considered.

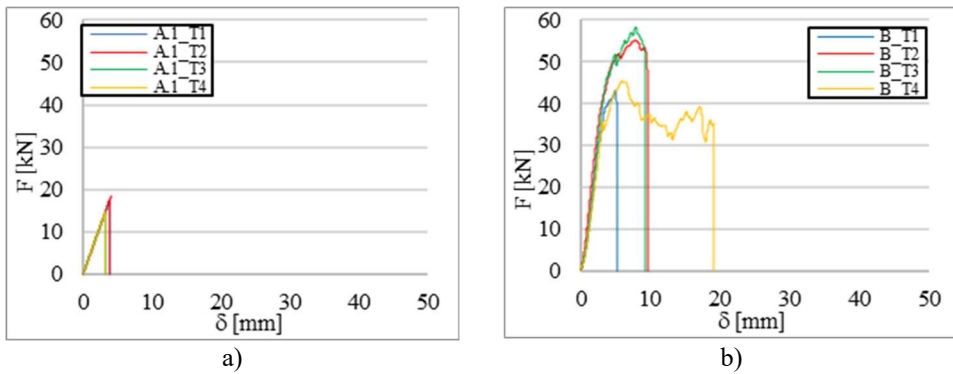


Figure 63. F- δ graphs: a) Group A.1; b) Group B.

Both the strength and stiffness increased significantly when the beam was subjected to shear force only. In detail, the stiffness increased by 84% (from 4.62 kN/mm to 8.49 kN/mm by considering the average values), while the strength increased by 190% (from 16.48 kN to 47.87 kN). Furthermore, the most interesting result relates to the failure mode which involved only the GFRP material. Figure 64 shows how the failure was localized to the connection between the flange and the web of the U-profile from different point of views.

From the last results, it is clear that the adhesive layer under the shear load condition is characterized by a shear stress distribution much lower than that of the case of Group A.1 (bending and shear). Thanks to this low stress distribution, the strength and the stiffness of the joint increased.

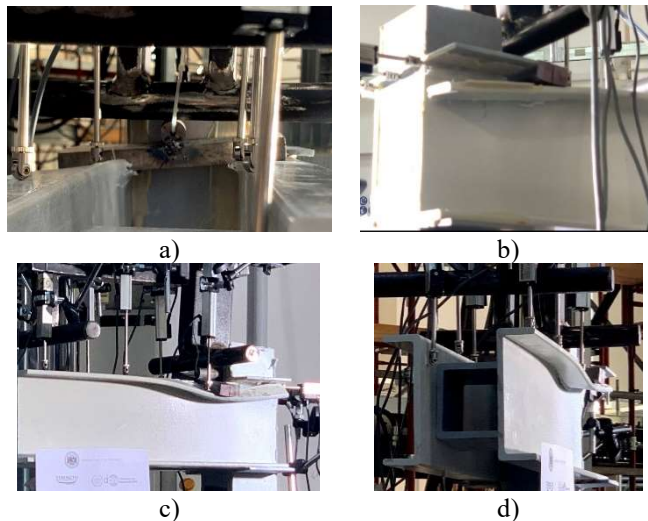


Figure 64. GFRP failure.

Table 24. Results of Groups A.1 and B.

Group	Test	$F_{exp}$ [kN]	$\delta_{v,conn}^{exp}$ [mm]	$\mu$		$\sigma^2$		$d$ [mm]	$M_t$ [kNm]	$\frac{\mu}{M_t}$ [kNm]
				$F_{exp}$ [kN]	$\delta_{v,conn}^{exp}$ [mm]	$F_{exp}$ [-]	$\delta_{v,conn}^{exp}$ [-]			
A.1	1	17.47	3.84						6.90	
	2	18.67	3.96	16.48	3.56	0.04	0.05	395	7.38	6.51
	3	14.77	3.22						5.83	
	4	15.03	3.23						5.93	
<hr/>										
B	1	43.02	5.17						3.44	
	2	51.83	5.28	47.87	5.64	0.03	0.03	80	4.15	3.83
	3	51.51	5.62						4.12	
	4	45.10	6.49						3.61	
<hr/>										

$\mu$  (average);  $\sigma^2$  (standard deviation)

From the results presented in this section, it is possible to conclude that in the case of the load applied at the free end of the beam, the bending moment and the shear force, acting on the beam, produce torsion and shear stresses in the adhesive, respectively. The tangential stresses due to the shear, acting on the adhesive layer in the vertical direction, are irrelevant with respect to those produced by torsion (acting on the adhesive layer in the horizontal direction also) which have to be considered responsible of the adhesive failure as presented for all the joint configurations of Groups A.

The main influence of the tangential stresses along the horizontal direction could justify the highest decrease of the joint strength of the Group A.4 (without angles) with respect to that of Group A.1 (with angles). When the angles are present, the moment produced by the internal tangential stresses due to torsion is higher than that in the case of the absence of the angles.

### 3.2.5. Influence of the hygro-thermal conditioning

This subsection discusses the influence of hygro-thermal conditioning. The results are collected in terms of load-displacement and moment-rotation curves (see Figures 65 and Table 25). The specimens aged in SW and TW were tested immediately after being taken out of the tanks in order to avoid the benefic contribution of the desorption as shown in Chapter 1.

The main result concerned the effect of the aging which influenced the strength of the joint (limitedly) and the stiffness of the connection (noticeably). In detail, the strength of Group C.1 (TW aging) was reduced by about 14%, while

that of Group C.2 by about 19%. Furthermore, the stiffness (evaluated at the load level of 8 kN – elastic stage) was reduced by about 72% for both Groups C.1 and C.2.

The decrease of the strength and the stiffness is due to plasticization more than hydrolysis phenomenon considering to the aging at low temperature (30°C) as shown in Chapter 1. Furthermore, the higher decreasing in terms of the stiffness than strength was due to the fact that the Araldite presents a ductile behavior and a high water uptake. Furthermore, the shear strength variation is to only 22%. This circumstance justifies the higher decrease in terms of stiffness than strength.

Finally, it is worth highlighting how the two tests (T3 for Group C.1 and T1 for Group C.2) were discarded in the evaluation of the average values reported in Table 25. These specimens failed prematurely as shown in Figure 65.

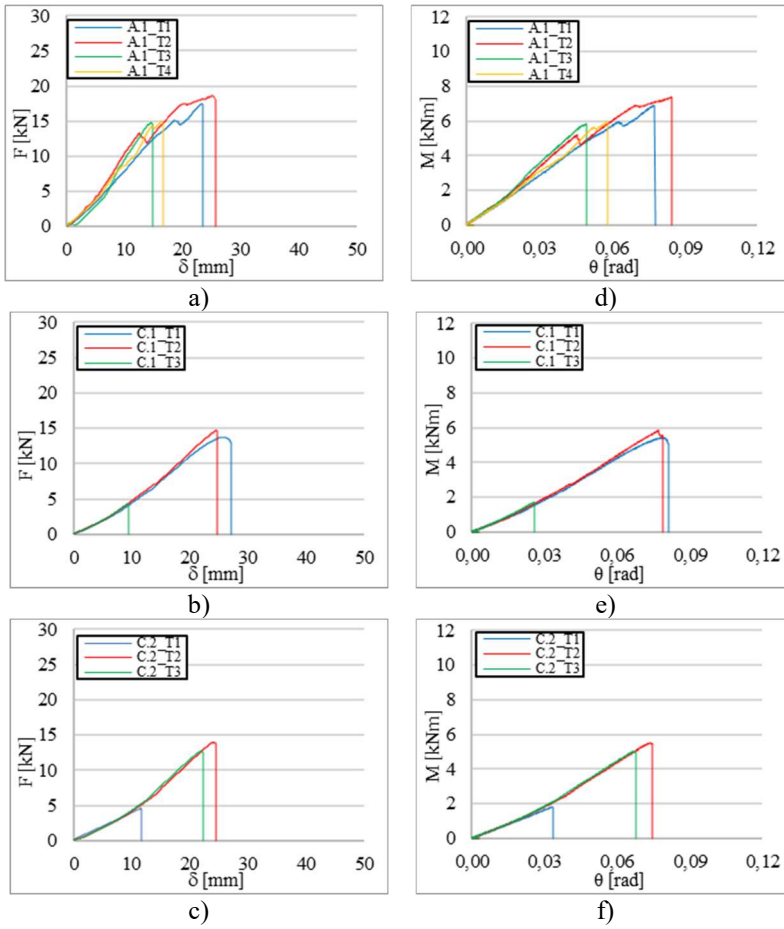


Figure 65. F-  $\delta$  and M-  $\theta$  graphs: a) and d) Group A.1 (Unaged); b) and e) Group C.1 (Tap Water); c) and f) Group C.2 (Sea Water).

Table 25. Results of Groups A.1, C.1 and C.2.

Group	Test	$\mu$		$\sigma^2$				$M_{exp}$	$\theta_{v,conn}^{exp}$	$\mu$		$\sigma^2$	
		$F_{exp}$	$\delta_{v,conn}^{exp}$	$F_{exp}$	$\delta_{v,conn}^{exp}$	$F_{exp}$	$\delta_{v,conn}^{exp}$			$d$	$M_{exp}$	$\theta_{v,conn}^{exp}$	$M_{exp}$
		[kN]	[mm]	[kN]	[mm]	[-]	[-]	[mm]	[kNm]	[rad]	[kNm]	[rad]	[rad]
A.1	1	17.47	23.41						6.90	0.078			
	2	18.67	25.69						7.38	0.085			
	3	14.77	14.77	16.48	20.14	0.04	0.20	395	5.83	0.049	6.51	0.068	0.19
	4	15.03	16.71						5.93	0.058			
C.2	1	13.76	27.08						5.44	0.081			
	2	14.75	24.66	14.26	25.87	-	-	395	5.83	0.079	5.63	0.080	-
	3*	-	-						-	-			
C.3	1*	-	-						-	-			
	2	13.95	24.49	13.31	23.37	-	-	395	5.51	0.075	5.26	0.072	-
	3	12.68	22.26						5.01	0.068			

$\mu$  (average);  $\sigma^2$  (standard deviation); \*(discarded)

### 3.3. Stress-strain distribution by DIC

In order to qualitatively analyse the shear deformation and tangential stress distribution relating to the bonded area, a DIC system was also adopted. The latter was also useful to evaluate the role played by the shear stresses moving from the bending load to the shear load condition and to capture the local cracks in the GFRP material when the shear load condition was investigated (section 3.2.4). The DIC system was used in all the tests presented in this chapter but for the sake of brevity the results presented are limited to the joint configurations of Group A.1 (reference) and Group B.

An example of the results produced by the DIC system are reported in Figure 66 with reference to test 1 of Group A.1. Based on the capacity of the DIC system used, a square area of 120mm x 120mm was investigated (the spackle pattern was applied to the web of the U-profile). The portion of the U-profile in correspondence to the bonded area is purple, while the portion of the U-profile not bonded is yellow/red. Each colour corresponds to a specific level of strain/stress as depicted on the right of Figure 66.

The stress distributions (normal and tangential) were evaluated for all the specimens along the two directions, vertical and horizontal of Figure 66, corresponding to the centroid axes of the adhesive area.

The results of Test 1 of Group A.1 are collected in Figure 67. In detail, the normal stresses  $\sigma_x$  and  $\sigma_y$  (strictly related to the GFRP material), and the

tangential stress  $\tau_{xy}$  (related to both the GFRP material and the adhesive layer also) are reported for each direction with reference to the load level of 8 kN which corresponds to an elastic behaviour of the connection (see Figure 56a). It is worth noting that the x and y directions correspond to the horizontal and vertical ones, respectively.

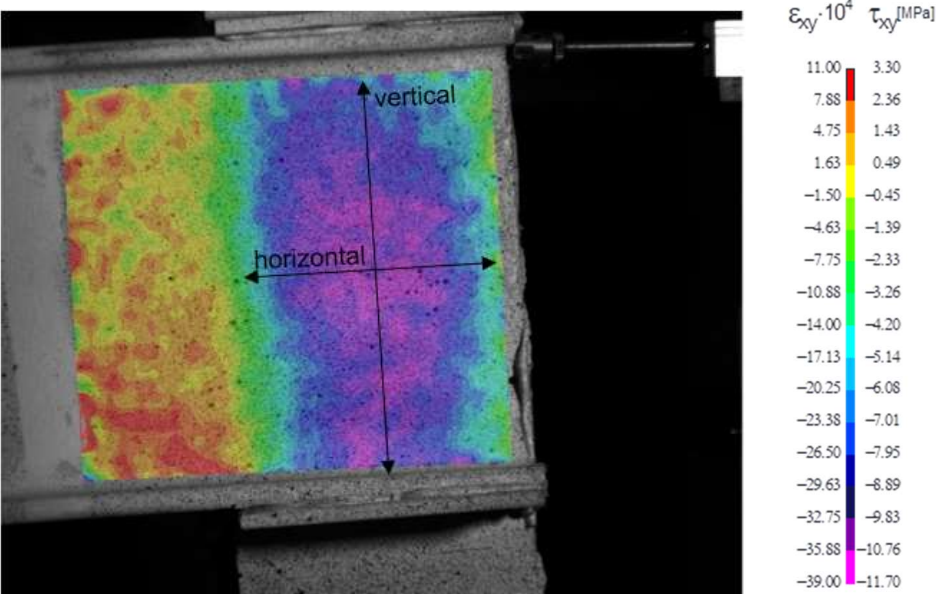


Figure 66. Strain/stress distribution evaluated by DIC (test 1, Group A.1).

All the tests of Group A.1 were subjected to a vertical force applied at the free end of the beam which was then subjected to a bending moment and a shear force. As shown in Figure 67, the normal stress distribution  $\sigma_x$  along the vertical axis had a classical bending moment trend (moment applied along x direction), with values much lower than the limit ones of the GFRP; the same stress distribution along the horizontal axis was equal to zero (neutral axis). Furthermore, the experimental set-up was thought to apply the bending moment only along x direction (horizontal direction) and consequently the stress distribution  $\sigma_y$  was correctly equal to zero along both directions. Finally, the shear stress distribution (along the vertical axis in particular) presents peak values equal or superior to the adhesive limit strength (9 MPa, Table 5) at the edges, while the same stresses outside the bonded area have a magnitude much lower than the GFRP limit shear strength (30 MPa, Table 19). This justifies the experimental failure observed and described in section 3.2.1.

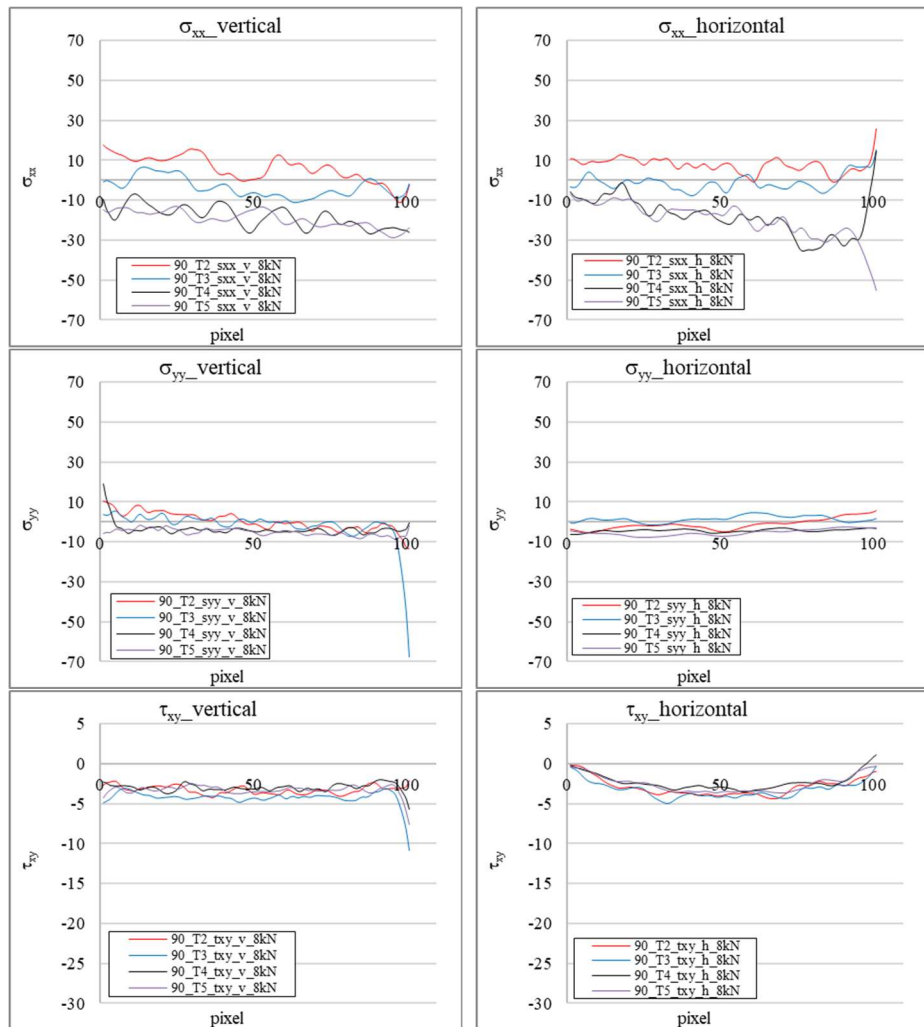


Figure 67. Result by DIC, stress distribution along the vertical and horizontal direction for Test 1 of Group A.1.

In order to better understand the stress distribution inside the bonded area for the shear load condition, the results of Test 2 of Group B are collected in Figure 68.

Considering the non-linear behaviour presented by all the beam-to-column connections relating to Group B and then also by Test 2 (Figure 63b), all the curves of Figure 68 related to four different load levels: 8 kN and 13 kN for a comparison with the similar joint under bending whose strength was 15 kN, 40 kN (elastic limit) and 55 kN (peak load for Test 2).

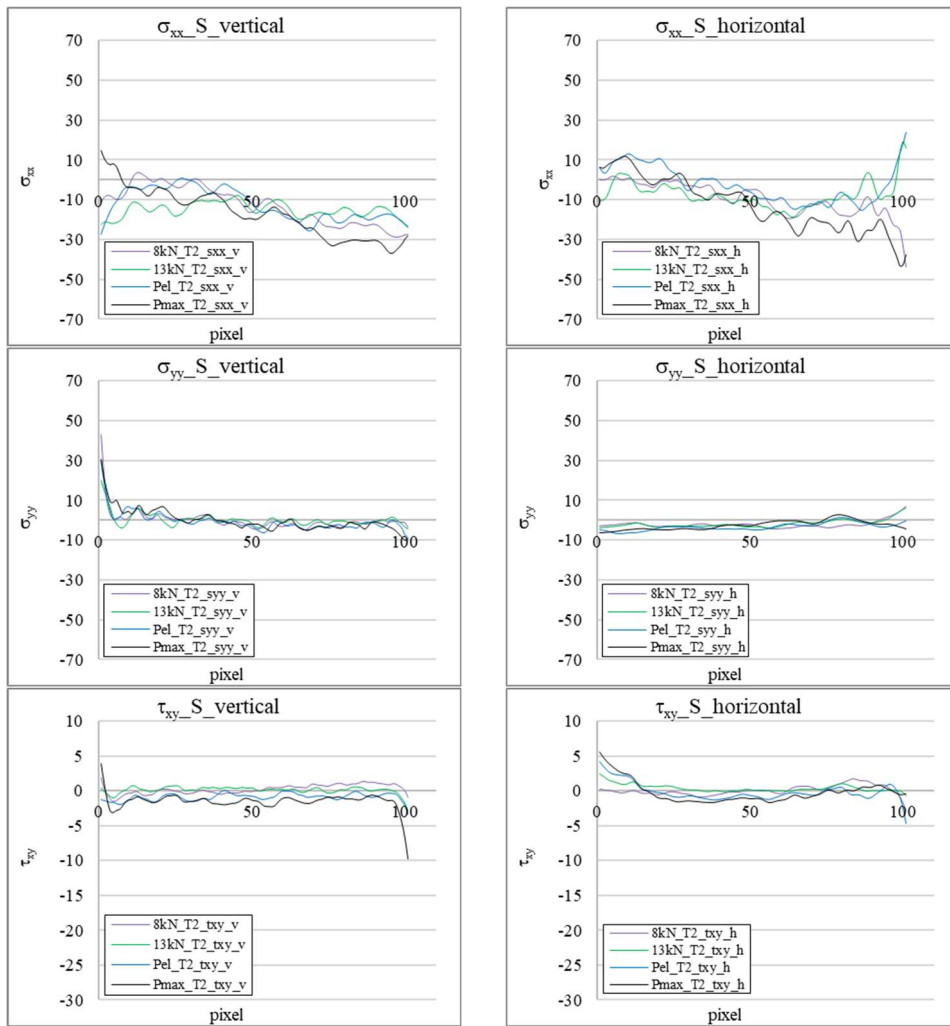


Figure 68. Result by DIC, stress distribution along the vertical and horizontal direction for Test 2 of Group B.

All the values of the normal stresses  $\sigma_x$  and  $\sigma_y$  were much lower than the GFRP material as already highlighted for the specimen of Group A, while the values of the tangential stresses for all the load levels under investigation were lower than the adhesive shear strength. The latter circumstance justifies why the failure of the shear load condition was not localized in the adhesive layer.

### 3.4. Further considerations about the failure modes

According to the experimental results presented in the previous section, it was possible to conclude that the tangential stresses, acting on the bonded area along the horizontal direction when the adhesive layer is subjected to torsion (bending moment in the beam), are responsible for the joint failure. The tangential stresses, due to the shear load condition, did not have any influence on the adhesive layer as shown by the experimental results (section 3.2.4).

Two different types of failure were experimentally observed: a mixed failure involving the adhesive layer and the GFRP mat and a failure at the interface between the GFRP and adhesive layer. The mixed failure was observed for the joints of Groups A.1, A.2, A.4 and A.5, where the horizontal dimension of the bonded area was 90mm (A.1, A.2 and A.4) or 120mm (A.5).

The failure at the interface between the GFRP and adhesive layer was experimentally observed for the joints of Group A.3, where the horizontal dimension of the bonded area was 45mm (the lowest one).

It is possible to conclude that the development of the horizontal length of the bonded area is a key parameter. The mixed failure was observed for specimens with the horizontal length equal or greater than 90mm, while the failure at the interface was observed when the length was over 45mm. It is possible to believe that 45mm is a value of the horizontal length lower than the “effective bonded length” of an adhesive joint whose axis is considered aligned with the beam axis. This means that the shear stresses in the adhesive layer were not completely transferred from one adherent to another, leading to a failure mainly concentrated in the adhesive.

Consequently, the values of the horizontal length of 90mm and 120mm could be considered greater than the “effective bonded length” of the joint. In this case, the shear stresses are completely transferred between the adherents leading to the failure of the mat. In practice, the shear stresses moved from the column to the U-profiles attacking the mat in its plane.

The in-plane shear strength of the mat is generally two-three times lower than that of the profile (about 13-20MPa in this case). This strength is compatible with the values of the shear stresses recorded by VIC.

### 3.5. Conclusions

A total of thirty full scale joints were realized and tested under a monotonically increased quasi-static loading up to failure. The results of the study support the following conclusions:

- In all the cases, the mechanical response of the joint was linear elastic up to failure due to the GFRP linear elastic behaviour. Some nonlinearities were due to the adhesive whose behaviour is non-linear;
- In the case of the load applied at the free end of the beam, the bending moment and the shear force, acting on the beam, produce torsion and shear in the adhesive, respectively;
- The tangential stresses due to the shear, acting on the adhesive layer in the vertical direction, are irrelevant with respect to those produced by torsion (acting on the adhesive layer in the horizontal direction also) which have to be considered responsible for the adhesive failure.
- The main influence of the tangential stresses along the horizontal direction could justify the high decrease of the joint strength when the height of the adhesive was reduced (the moment produced by the internal tangential stresses due to torsion was consequently reduced);
- The aging conditions influenced both the strength and stiffness of the joint by about 15% and 70%, respectively.

## **CHAPTER IV: Mechanical models and closed form solutions for the evaluation of the strength and the stiffness of a beam-to-column adhesive connection between pultruded profiles**

### **4. Introduction**

Based on a large database, presented in the previous chapter 3, performing several full scale experimental tests relative to the mechanical behaviour of full adhesive beam-to-column joints between pultruded profiles, there are here presented two mechanical models with closed form solutions in order to predict both the strength and the stiffness of such a connection. The comparison with experimental results available in the literature made it possible to verify the effectiveness of the proposed formulation which involves only a few geometric and mechanical parameters as better described below.

Current literature presents the results of several research about the evaluation of the stress and deformation states inside an adhesive joint following the two following approaches: 1) linear elasticity [78-85]; 2) fracture mechanic principles [86-92].

Mechanical models and closed form solutions were presented in the past in literature in relation to joints which mainly transfer normal stress. For a beam-to-column connection, for which the stress regime is much more complex, the literature in terms of mechanical predicting models is relatively poor [93-97] since most of the research carried out focuses on the global mechanical response from an experimental point of view.

#### **4.1. Phenomenological interpretation of the mechanical behaviour of the beam-column connection**

According to the experimental results, the tangential stresses inside the adhesive layer (rectangular cross section) due to torsion have a trend as depicted in Figure 69.

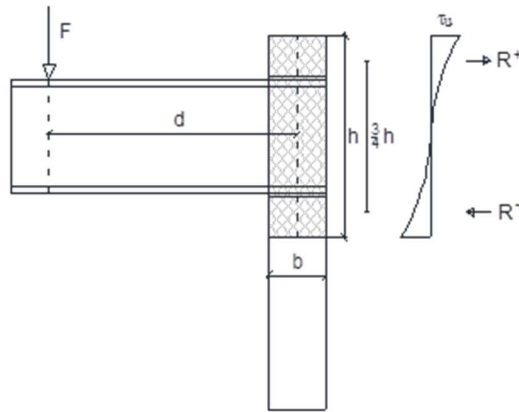


Figure 69. Tangential stresses trend inside the adhesive layer due to torsion.

The relation between the applied force  $F$  and the resultants of the shear stresses ( $R^+$  in traction or  $R^-$  in compression) could be found by the rotational equilibrium balance reported in Eqn.(29)

$$M_e = M_i \quad (29)$$

where

$$M_e = F \cdot d \quad (30)$$

$$M_i = 2 \cdot R^+ \cdot \frac{3}{4} \cdot h = 2 \cdot R^- \cdot \frac{3}{4} \cdot h \quad (31)$$

By equating Eqs. (30) and (31) it is possible to obtain the following equation:

$$F = \frac{3}{2} \cdot \frac{h}{d} \cdot R^+ = \frac{3}{2} \cdot \frac{h}{d} \cdot R^- \quad (32)$$

The number “2” in the Eqn. (31) was inserted to consider both the adhesive layers of the connection under investigation.

Due to the superior influence of the horizontal tangential stresses (along the axis of the beam) with respect to the vertical ones, the main idea is to evaluate the strength of the beam-to-column connection by considering the scheme of Figure 70 relative to a single lap joint characterized by a bonded length  $b_{SLJ}$  (equal to the dimension  $b$  of the bonded area), by a thickness  $t$  (equal to the

thickness of the GFRP U-profile) and subjected to a traction force (equal to the resultant  $R^+$  of Figure 69).

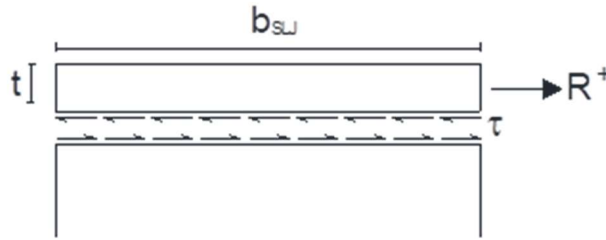


Figure 70. Single lap joint scheme.

#### 4.1.1. Hypothesis of the mechanical model

The mechanical model, based on the scheme of the single lap joint subjected to a traction force before introduced, is characterized by the following hypotheses:

1) The adhesive layer is modelled by a continuous set of independent springs, placed parallel to the axis of the joint in order to contrast the relative axial displacements ( $s$ ) of the adherents in contact. The constitutive law of the springs is depicted in Figure 71 where  $\tau$  denotes the adherent/adhesive interaction per surface unit and  $s$  denotes the relative axial displacement between the adherents.

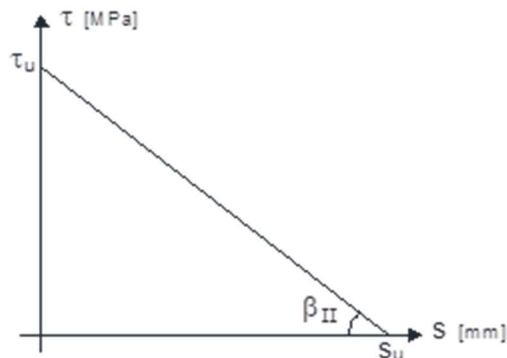


Figure 71. Softening rigid bond.

The softening law could be analytically expressed as follows:

$$\tau(s) = \begin{cases} \beta_{II} \cdot (s_u - s) & \text{if } s < s_u \\ 0 & \text{if } s > s_u \end{cases} \quad (33)$$

The assumption that the elastic stage of the constitutive law is negligible is realistic considering that the elastic relative displacement is about 100 times lower than that of the ultimate one ( $s_u$ ) as demonstrated in [57]. In Figure 71, the further symbol  $\tau_u$  is the adhesive shear strength.

2) The trend of the tangential stresses is supposed constant through the width of the joint [24]. For this reason, the parabolic distribution of Figure 69 is transformed into an equivalent constant distribution as depicted in Figure 72a. It is worth noting that the application points of the resultants  $R^+$  and  $R^-$  are still the same. Consequently, the final scheme of the joint is reported in Figure 72b.

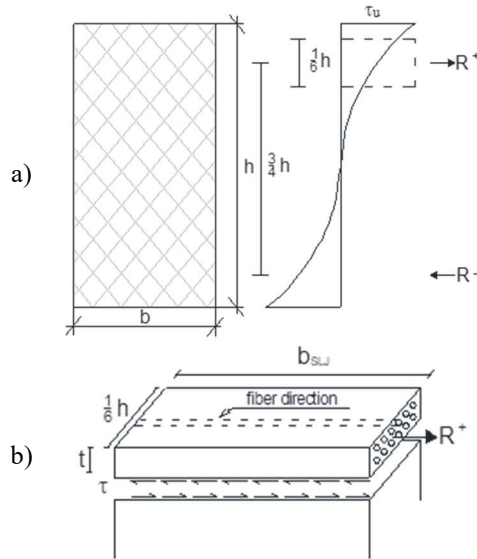


Figure 72. Correction for the length of the joint width: a) Equivalent tangential stresses distribution; b) final joint scheme.

3) The column is supposed infinitely rigid. This assumption is realistic by considering that the applied load  $F$  is parallel to the column fibers direction. For this direction the strength of the GFRP material is in general at least four times bigger than that of orthogonal direction.

4) The adhesion between the adherents is supposed to be perfect.

### 4.1.2. Governing equations

In Figure 73.a the equilibrium problem of a single lap-joint with FRP adherent subject to normal stresses (N) is represented. The adherent is modelled according to the beam technical theory assuming the hypothesis of conservation of the plane sections.

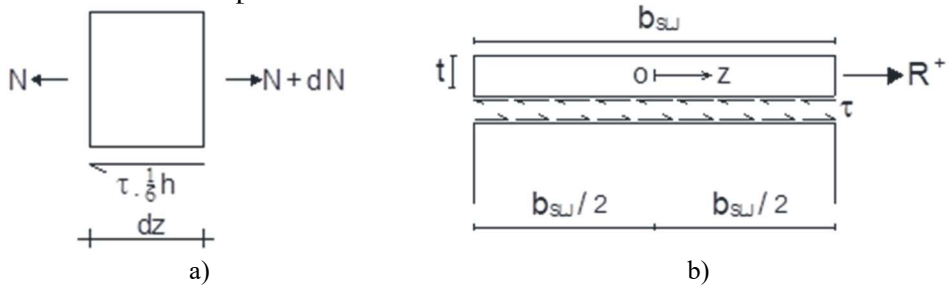


Figure 73. Governing equation: a) Equilibrium problem of a single lap joint subjected to the normal stresses; b) Reference system.

The indefinite equilibrium equation in the longitudinal direction of the adherent can be expressed as follows:

$$\frac{dN}{dz} - \tau(s) \cdot \frac{1}{6}h = 0 \quad (34)$$

The normal stress can be written as reported in Eqn. (34) by considering the corresponding constitutive law:

$$N = E \cdot A \cdot \frac{ds}{dz} \quad (35)$$

where  $A(= t_{layer} \cdot h/6)$  is the surface where the tangential stresses are defined and  $E(= E_{GFRP})$  is the GFRP elastic modulus along fibers direction. Substituting Eqn. (35) into Eqn. (34) it is possible to obtain:

$$E \cdot t_{layer} \cdot \frac{d^2s}{dz^2} - \tau(s) = 0 \quad (36)$$

Substituting the Eqn. (33) into Eqn. (36) it possible to finally obtain the following second order differential equation:

$$\frac{d^2s}{dz^2} - \omega_s^2 \cdot (s_u - s) = 0 \text{ where } \omega_s^2 = \frac{\beta_{II}}{E \cdot t_{layer}} \quad (37)$$

The solution of Eqn. (37) assumes the following form:

$$s(z) = s_u + A \cdot \cos(\omega_s \cdot z) + B \cdot \sin(\omega_s \cdot z) \quad (38)$$

The axial coordinate  $z$  is defined in the following interval as depicted in Figure 73b:

$$-\frac{b_{SLJ}}{2} \leq z \leq \frac{b_{SLJ}}{2} \quad (39)$$

Consequently, the constants  $A$  and  $B$  could be obtained by considering the following boundary conditions:

$$\left\{ \begin{array}{l} E \cdot A \cdot \frac{ds}{dz} \Big|_{z=-\frac{b_{SLJ}}{2}} = 0 \\ E \cdot A \cdot \frac{ds}{dz} \Big|_{z=\frac{b_{SLJ}}{2}} = R^+ \end{array} \right. \quad (40.a)$$

$$\left\{ \begin{array}{l} E \cdot A \cdot \frac{ds}{dz} \Big|_{z=\frac{b_{SLJ}}{2}} = R^+ \\ R^+ \end{array} \right. \quad (40.b)$$

$$\left\{ \begin{array}{l} A = -\frac{R^+}{2 \cdot \sin\left(\frac{\omega_s \cdot b_{SLJ}}{2}\right) E \cdot t_{layer} \cdot \omega_s} \\ R^+ \end{array} \right. \quad (41.a)$$

$$\left\{ \begin{array}{l} B = \frac{R^+}{2 \cdot \cos\left(\frac{\omega_s \cdot b_{SLJ}}{2}\right) \cdot E \cdot t_{layer} \cdot \omega_s} \\ R^+ \end{array} \right. \quad (41.b)$$

Then, the solutions in terms of  $s(z)$  and  $\tau(z)$  could be written as follows, respectively:

$$s(z) = s_u - \frac{R^+}{E \cdot t_{layer} \cdot \omega_s} \cdot \frac{\cos\left[\omega_s \cdot \left(z + \frac{b_{SLJ}}{2}\right)\right]}{\sin(\omega_s \cdot L)} \quad (42.a)$$

$$\tau(z) = \beta \frac{R^+}{E \cdot t_{layer} \cdot \omega_s} \cdot \frac{\cos\left[\omega_s \cdot \left(z + \frac{b_{SLJ}}{2}\right)\right]}{\sin(\omega_s \cdot L)} \quad (42.b)$$

Having to be  $s(z) \leq s_u$  (according to Eqn. (33)), the following relation must be verified:

$$0 \leq \omega_s \cdot \left( z + \frac{b_{SLJ}}{2} \right) \leq \pi/2 \quad (43)$$

Through some algebras, the Eqn. (39) could be transformed as follows (multiplying for  $\omega_s$  and adding the quantity  $(b_{SLJ}/2 \cdot \omega_s)$  to each term:

$$0 \leq \omega_s \cdot \left( z + \frac{b_{SLJ}}{2} \right) \leq b_{SLJ} \cdot \omega_s \quad (44)$$

Matching the Eqn. (43) and (44), it is possible to conclude that:

$$0 \leq \omega_s \cdot \left( z + \frac{b_{SLJ}}{2} \right) \leq b_{SLJ} \cdot \omega_s \leq \pi/2 \quad (45)$$

Then, it is possible to define the maximum value ( $b_{eff}$ ) of b as follows:

$$b_{eff} = \frac{\pi}{2 \cdot \omega_s} \quad (46)$$

It is worth to remember that the symbol  $b_{eff}$  represents the well known “effective stress transfer length (development length)” which is defined as the distance from the loaded end where the axial effects (Mode II) can be considered extinct, as if the length of the joint were infinite.

Finally, the length  $b_{SLJ}$  of the single lap-joint could assumes the following values:

$$b_{SLJ} = b \quad (b \leq b_{eff}) \quad (47.a)$$

$$b_{SLJ} = b_{eff} \quad (b > b_{eff}) \quad (47.b)$$

In Figure 74, the graphs of the relative displacement  $s(z)$  and the coupled shear stress  $\tau(z)$  are depicted for the case  $b_{SLJ} = b$  (Figure 74a) and  $b_{SLJ} = b_{eff}$  (Figure 71b).

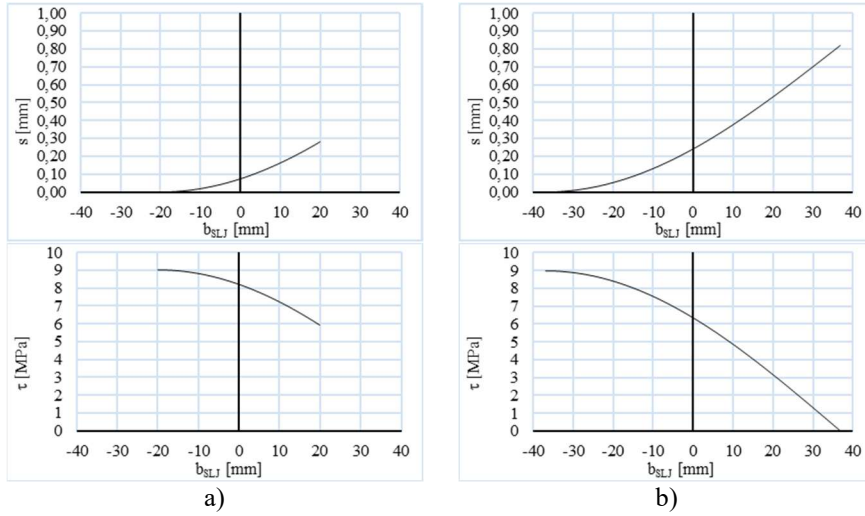


Figure 74. Numerical model results in terms of relative displacement  $s(z)$  and conjugated shear stress  $\tau(z)$ : a)  $b_{SLJ}=b$ ; b)  $b_{SLJ}=b_{eff}$ .

It is possible to understand that only if the joint length  $b$  is almost equal to  $b_{eff}$  the traction force applied to the upper adherent could be transferred totally to the bottom adherent (in fact the slip at a distance equal to  $b_{eff}$  from point application load is equal to zero).

Consequently, the final expression of the tangential stress resultants  $R^+$  (or  $R^-$ ) it is obtainable by Eqn. (42a) by imposing that the relative displacement at  $z = -b_{SLJ}/2$  has to be zero (no sliding) as below reported:

$$b_{SLJ} = b \quad R^+ = R^- = \frac{1}{6} h \cdot \sqrt{s_u \cdot \tau_u \cdot E_{GFRP} \cdot t_{layer} \cdot \sin(\omega_s \cdot b)} \quad (48.a)$$

$$b_{SLJ} = b_{eff} \quad R^+ = R^- = \frac{1}{6} h \cdot \sqrt{s_u \cdot \tau_u \cdot E_{GFRP} \cdot t_{layer}} \quad (48.b)$$

Finally, substituting the expression of  $R^+ (= R^-)$  into Eqn. (32) it is possible to obtain the final expression of the joint strength in terms of the load  $F$ :

$$\begin{aligned}
b_{SLJ} = b \quad & F = \frac{1}{4} \cdot \frac{h^2}{d} \cdot \sqrt{s_u \cdot \tau_u \cdot E_{GFRP} \cdot t_{layer} \cdot \sin(\omega_s \cdot b)} \\
& F = \frac{1}{4} \cdot \frac{h^2}{d} \cdot \sqrt{2 \cdot G_{II} \cdot E_{GFRP} \cdot t_{layer} \cdot \sin(\omega_s \cdot b)}
\end{aligned} \tag{49.a}$$

$$\begin{aligned}
b_{SLJ} = b_{eff} \quad & F = \frac{1}{4} \cdot \frac{h^2}{d} \cdot \sqrt{s_u \cdot \tau_u \cdot E_{GFRP} \cdot t_{layer}} \\
& F = \frac{1}{4} \cdot \frac{h^2}{d} \cdot \sqrt{2 \cdot G_{II} \cdot E_{GFRP} \cdot t_{layer}}
\end{aligned} \tag{49.b}$$

In Eqn. (49a-b) the term  $G_{II}$  represents the fracture energy in Mode II (the area under the graph of Figure 71).

#### 4.1.3. Further considerations about the mechanical model

The mechanical model presented in the previous subsections presents the following two limitations:

1) The maximum joint strength is function of the effective stress transfer length  $b_{eff}$ . Experimentally, it was shown that for the values of bonded length  $b$  greater than  $b_{eff}$ , the strength of the joint increased and the trend was more than linear. According to the results presented in Table 23, it is possible to conclude that increasing the length  $b$  (from 90mm of the Group A.1 to 120mm of the Group A.5 and considering that the  $b_{eff}$  for the Araldite resin is equal to 73.45mm), the glued area increased by 33% while the strength increased by 54%;

2) The tangential stresses along the vertical direction (along  $h$ ) even if negligible with respect to those in the horizontal direction are not zero.

In order to take into account both the above-mentioned circumstances, a corrective factor for the closed form solution of Eqn. (48a-b) it is here presented.

Relating to the first point, if the bonded length  $b$  greater than  $b_{eff}$ , the relative correction factor is the ratio  $b/b_{eff}$  (which value is greater than one). In the opposite case ( $b < b_{eff}$ ), the aforementioned ratio assumes the unitary value. Furthermore, regarding the tangential stresses along the vertical direction (shear stresses,  $\tau^S$ ), the relative correction factor here proposed is the ratio

between the maximum tangential stress (due to torsion,  $\tau^M$ ) and the maximum total tangential stress (due to the sum of the shear and the torsion,  $\tau^S + \tau^M$ ). Finally, the correction factor,  $\gamma$  proposed assumes the expression below reported in Eqs. (50a-b):

$$b_{SLJ} = b \quad \gamma = \frac{\tau_M}{\tau_S + \tau_M} \quad (50.a)$$

$$b_{SLJ} = b_{eff} \quad \gamma = avg \left( \frac{\tau_M}{\tau_S + \tau_M}; \frac{b}{b_{eff}} \right) \quad (50.b)$$

The joint strength (in terms of the force F) assumes the following expressions:

$$b_{SLJ} = b \quad F = \frac{1}{4} \cdot \frac{h^2}{d} \cdot \gamma \cdot \sqrt{2 \cdot G_{II} \cdot E_{GFRP} \cdot t_{layer} \cdot \sin(\omega_s \cdot b)} \quad (51.a)$$

$$b_{SLJ} = b_{eff} \quad F = \frac{1}{4} \cdot \frac{h^2}{d} \cdot \gamma \cdot \sqrt{2 \cdot G_{II} \cdot E_{GFRP} \cdot t_{layer}} \quad (51.b)$$

#### 4.1.4. About the tangential stresses due to shear and torsion

In order to evaluate the factor  $\gamma$  of Eqn. (50a-b), the maximum values of the tangential stresses due to shear and torsion respectively, could be evaluated by classical formulas of the structural mechanics as below reported:

$$\tau_{max}^{Shear} = \frac{3(F/2)}{2A_{glued}} = \frac{3(F/2)}{2 \cdot b \cdot h} \quad (52)$$

$$\tau_{max}^{Torsion} = \alpha \cdot \frac{(F \cdot d)/2}{h \cdot b^2} = \left( 3 + 1,8 \frac{b}{h} \right) \cdot \frac{(F \cdot d)/2}{h \cdot b^2} \quad (53)$$

In Eqn. (52) and (53), the load F applied at the free end of the beam and then the torque moment ( $F \cdot d$ ) inside the adhesive layer are divided by the factor 2 to take into account the two adhesive layers characterizing the joint under investigation.

The maximum values of the tangential stresses above introduced were collected in Table 26.

Table 26. Tangential stresses in the adhesive layer due to Shear and Torsion.

Type #	$b$ [mm]	$h$ [mm]	$F$ [kN]	$d$ [mm]	$F \cdot d$ [kNm]	$\alpha$ [-]	$\tau_{max}^{Shear}$ [N/mm <sup>2</sup> ]	$\tau_{max}^{MTorsion}$ [N/mm <sup>2</sup> ]	$\tau^S + \tau^M$ [N/mm <sup>2</sup> ]		
A.1	90	270	1		17.47		6.90	0.54	5.68	6.22	
			2		18.67	395	7.38	3.60	0.58	6.07	6.65
			3		14.77		5.83		0.46	4.80	5.26
			4		15.03		5.93		0.46	4.88	5.35
A.2	65	270	1		19.71		7.54	0.84	11.35	12.19	
			2		13.54	382.5	5.18	3.43	0.58	7.79	8.37
			3		15.92		6.09		0.68	9.16	9.84
			4		17.73		6.78		0.76	10.20	10.96
A.3	40	270	1		16.23		6.01	1.13	22.71	23.83	
			2		13.68	370	5.06	3.27	0.95	19.13	20.08
			3		15.50		5.74		1.08	21.69	22.77
			4		10.85		4.01		0.75	15.18	15.93
A.4	90	150	1		7.47		2.95	0.42	4.95	5.37	
			2		9.34	395	3.69	4.08	0.52	6.20	6.72
			3		6.94		2.74		0.39	4.60	4.99
			4		9.26		3.66		0.51	6.14	6.65
A.5	120	270	1		25.66		9.75	0.59	4.76	5.36	
			2		28.22	380	10.72	3.80	0.65	5.24	5.89
			3		23.09		8.77		0.53	4.29	4.82
			4		24.89		9.46		0.58	4.62	5.20
C.1	90	270	1		13.76		5.44	0.42	4.47	4.90	
			2		14.75	395	5.83	3.60	0.46	4.80	5.25
			3*		4.32		1.71		0.13	1.40	1.54
C.2	90	270	1*		4.59		1.81	0.14	1.49	1.63	
			2		13.95	395	5.51	3.60	0.43	4.53	4.96
			3		12.68		5.01	0.39	4.12	4.51	

\*(discarded)

## 4.2. Adhesive layer deformability (evaluation of the vertical displacement corresponding to the force F)

In this section the analytical formulations of the vertical displacement of the beam,  $\delta_v$  (at the same cross section where the load F is applied), and the beam-to-column relative rotation,  $\theta_{conn}$ , are furnished considering the adhesive layer deformability. The latter was modelled by a rotational spring located at the beam-to-column connection as depicted in Figure 75.

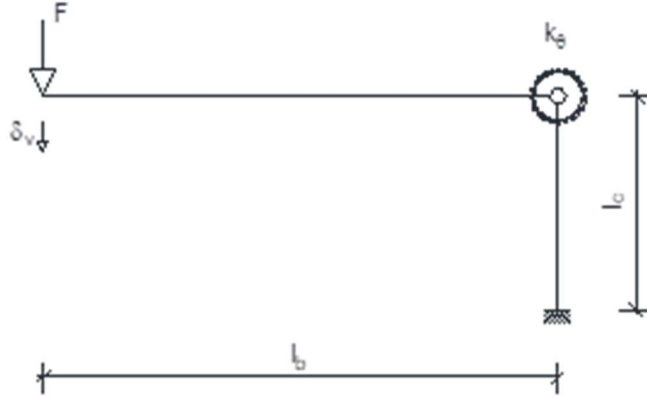


Figure 75. Rotational spring for evaluating the adhesive layer deformability.

The above mentioned expressions are reported in Eqn. (54) and Eqn. (55), respectively. The meaning of the symbols introduced is the following:  $l_b$  is the beam length;  $l_c$  is the column length;  $I_b$  and  $A_b$  are the second moment of inertia and the area of the cross section of the beam, respectively;  $I_c$  and  $A_c$  are the second moment of inertia and the area of the cross section of the column, respectively;  $E$  and  $G$  are the longitudinal and shear modulus of elasticity of the GFRP, respectively;  $F$  is the load applied at the free end of the beam;  $K_\theta$  is the stiffness of the rotational spring. Furthermore, in Eqn. (55) the term  $\varphi_c = \delta_h / l_c$  represents the column rotation in correspondence of the beam-to-column connection evaluated by means of the horizontal column displacement  $\delta_h$  which expression is reported in Eqn. (56).

$$\delta_v = \frac{F \cdot l_b^3}{3E \cdot I_b} + \frac{\chi \cdot F \cdot l_b}{G \cdot A_b} + \frac{F \cdot l_b^2 \cdot l_c}{E \cdot I_c} + \frac{F \cdot l_c}{E \cdot A_c} + \frac{F \cdot l_b^2}{K_\theta} \quad (54)$$

$$\theta_{conn} = \varphi_b - \varphi_c = \frac{\delta_v}{l_b} - \frac{\delta_h}{l_c} \quad (55)$$

$$\theta_{conn} = \frac{F \cdot l_b^2}{3E \cdot I_b} + \frac{\chi \cdot F}{G \cdot A_b} + \frac{F \cdot l_c}{E \cdot A_c \cdot l_b} - \frac{F \cdot l_b \cdot l_c}{2E \cdot I_c} + \frac{F \cdot l_b}{K_\theta}$$

$$\delta_h = \frac{F \cdot l_b \cdot l_c^2}{2E \cdot I_c} \quad (56)$$

Once the load  $F$  and the corresponding displacement  $\delta_v$  are known the stiffness of the joint could be evaluated.

#### 4.2.1. Formula proposal for the evaluation of $K_\theta$

In this sub-section a formula for the evaluation of  $K_\theta$  is proposed. To this scope, by assuming for  $F$  and  $\delta_v$  the experimental values collected in Tables 21-25, all the corresponding values of  $K_\theta$  were evaluated by means of Eqn. (57) and summarized in Table 27 ( $K_\theta^{exp}$ ).

Table 27.  $K_\theta$  evaluation.

Group	Test	$F^{exp}$ [kN]	$\delta_v^{exp}$ [mm]	$d$ [mm]	$M_{exp}$ [kNm]	$\theta_{Conn}^{exp}$ [rad]	$K_\theta^{exp}$ [Nmm]	$\mu(K_\theta^{exp})$ [Nmm]	$K_\theta^{num}$ [Nmm]
A.1	1	17.47	23.41	395	6.90	0.078	$1.16 \cdot 10^8$	$1.32 \cdot 10^8$	$9.72 \cdot 10^7$
	2	18.67	25.69		7.38	0.085	$1.13 \cdot 10^8$		
	3	14.77	14.77		5.83	0.049	$1.56 \cdot 10^8$		
	4	15.03	16.71		5.93	0.058	$1.40 \cdot 10^8$		
A.2	1	19.71	27.20	383	7.54	0.088	$1.06 \cdot 10^8$	$1.05 \cdot 10^8$	$9.72 \cdot 10^7$
	2	13.54	17.63		5.18	0.061	$1.12 \cdot 10^8$		
	3	15.92	17.60		6.09	0.062	$1.32 \cdot 10^8$		
	4	17.73	38.05		6.78	0.117	$6.82 \cdot 10^7$		
A.3	1	16.23	17.91	370	6.01	0.064	$1.24 \cdot 10^8$	$1.33 \cdot 10^8$	$9.72 \cdot 10^7$
	2	13.68	14.14		5.06	0.052	$1.32 \cdot 10^8$		
	3	15.50	14.71		5.74	0.056	$1.44 \cdot 10^8$		
	4	10.85	11.37		4.01	0.038	$1.31 \cdot 10^8$		
A.4	1	7.47	13.39	395	2.95	0.042	$8.70 \cdot 10^7$	$9.74 \cdot 10^7$	$9.72 \cdot 10^7$
	2	9.34	13.45		3.69	0.046	$1.08 \cdot 10^8$		
	3	6.94	11.40		2.74	0.037	$9.50 \cdot 10^7$		
	4	9.26	14.59		3.66	0.048	$9.90 \cdot 10^7$		
A.5	1	25.66	13.03	380	9.75	0.102	$2.84 \cdot 10^8$	$2.84 \cdot 10^8$	$1.30 \cdot 10^8$
	2	28.22	14.33		10.72	0.112	$2.84 \cdot 10^8$		
	3	23.09	11.72		8.77	0.091	$2.84 \cdot 10^8$		
	4	24.89	12.64		9.46	0.098	$2.84 \cdot 10^8$		
B	1	43.02	5.17	80	3.44	-	-	-	-
	2	51.83	5.28		4.15	-	-	-	-
	3	51.51	5.62		4.12	-	-	-	-
	4	45.10	6.49		3.61	-	-	-	-
C.1	1	13.76	27.08	395	5.44	0.081	$7.93 \cdot 10^7$	$8.63 \cdot 10^7$	$9.72 \cdot 10^7$
	2	14.75	24.66		5.83	0.079	$9.33 \cdot 10^7$		
	3*	4.32	9.47		1.71	0.026	$7.12 \cdot 10^7$		
C.2	1*	4.59	11.76	395	1.81	0.034	$6.09 \cdot 10^7$	$8.89 \cdot 10^7$	$9.72 \cdot 10^7$
	2	13.95	24.49		5.51	0.075	$8.89 \cdot 10^7$		
	3	12.68	22.26		5.01	0.068	$8.89 \cdot 10^7$		

It is worth highlighting that the vertical experimental displacements of Table 27 are relative to the adhesive layer deformability only. Then, in the Eqn. (54) only the last term was taken into account.

In the last column of the Table 27 are also reported all the  $K_\theta$  values by adopting the proposed formula below reported.

$$K_\theta = E_{resin} \cdot h_{GFRP} \cdot b_{GFRP} \cdot t_{resin} \quad (57)$$

In Eqn. (57) the stiffness of the rotational spring (which represents the adhesive layer deformability) is function of: 1) the elastic modulus of the resin; 2) the total thickness of the resin (counting all the adhesive layers); 3) the adhesive layer geometry which is defined by the overlapping area between the beam and the column. In details,  $h_{GFRP}$  and  $b_{GFRP}$  are the height of the cross section of the beam and the width of the column, respectively.

#### 4.3. Validation of the mechanical model by comparing the numerical results with the experimental ones

In this section a comparison between the numerical and experimental results is presented. In detail, the numerical results are relative to the evaluation of the joint strength (in terms of the force  $F$  of Figure 75) and joint stiffness (in terms of the slope of the  $F - \delta_v$  and  $M - \theta_{conn}$  curves). The strength was evaluated by adopting the Eqn. (51a-b) while the vertical displacement  $\delta_v$  and the rotation  $\theta_{conn}$  by using the last term only of the Eqn. (54) and (55) (in order to take in account the adhesive layer deformability only as assumed in the experimental program).

All the values of the geometrical and mechanical parameters involved in the above mentioned formulas are summarized in Table 28. The meaning of the geometrical parameters is depicted in Figure 76.

Table 28. Values of the geometrical and mechanical parameters of resin and GFRP material.

Resin										
Group	$\tau_u$ [MPa]	$s_u$ [mm]	$G_{II}$ [N/mm]	$\beta$ [N/mm <sup>3</sup> ]	$t_{layer}$ [mm]	$E_{resin}$ [GPa]	$\omega_s$ [1/mm]	$\gamma$ [-]	$b_{eff}$ [mm]	$b_{SLJ}$ [mm]
A.1								1.07		73.45
A.2								0.93		65.00
A.3	9.00	0.82	4.10	10.98	1.00	2.00	0.021	0.95	73.45	40.00
A.4								1.07		73.45
A.5								1.26		73.45
C.1										58.89
C.2	7.00	0.82	3.28	8.54	1.00	2.00	0.027	1.22	58.89	58.89

GFRP										
	$E_{GFRP}$ [GPa]	$G_{GFRP}$ [GPa]	$d = l_b$ [mm]	$h$ [mm]	$b$ [mm]	column			beam	
						$l_c$ [mm]	$I_c$ [mm <sup>4</sup> ]	$A_c$ [mm <sup>2</sup> ]	$I_b$ [mm <sup>4</sup> ]	$A_b$ [mm <sup>2</sup> ]
A.1			395	270	90					
A.2			383	270	65					
A.3	24.00	3.00	370	270	40	165	$2.97 \cdot 10^6$	2624	$1.05 \cdot 10^7$	3584
A.4			395	150	90					
A.5			380	270	120					
C.1										
C.2	12.00	3.00	395	270	90	165	$2.97 \cdot 10^6$	2624	$1.05 \cdot 10^7$	3584

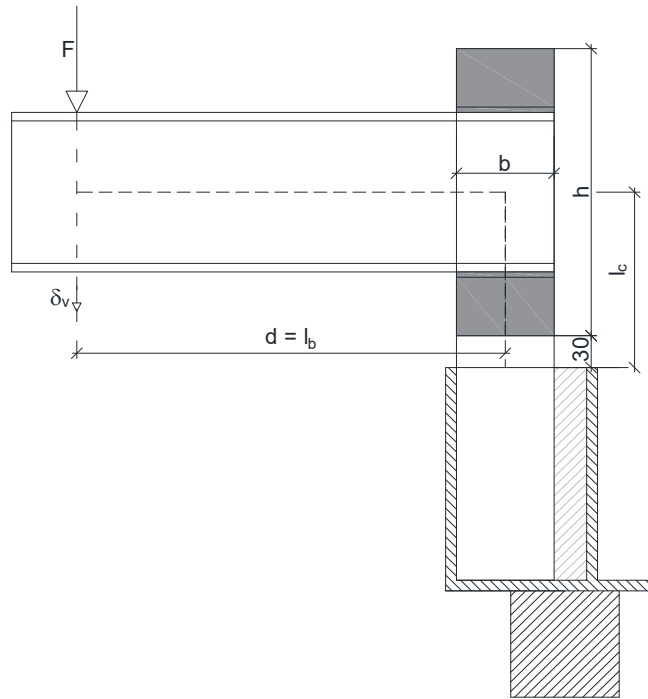


Figure 76. Geometrical parameters involved in the mechanical model.

All values of the joint strength, predicted by the mechanical model here presented, are collected in the Table 29 while all values, relative to both the vertical displacement  $\delta_v$  and the beam-to-column relative rotation  $\theta_{conn}$ , are reported in Table 30.

Table 29. Joint strength prediction (in terms of force F and bending moment M).

		A.1	A.2	A.3	A.4	A.5	C.1	C.2
$F^{num}$	[kN]	20.76	18.36	14.91	6.44	25.46	14.78	14.78
$M^{num}$	[kNm]	8.20	7.02	5.52	2.54	9.68	5.84	5.84
$F_{Gnl}^{num}$	[kN]	8.30	7.34	5.96	2.57	10.18	6.70	6.70
$F_{CEN}^{num}$	[kN]	12.37	10.40	8.81	3.84	15.17	5.28	5.28

Table 30. Joint stiffness prediction (in terms of the slope of  $F-\delta_v$  and  $M-\theta_{conn}$  curves).

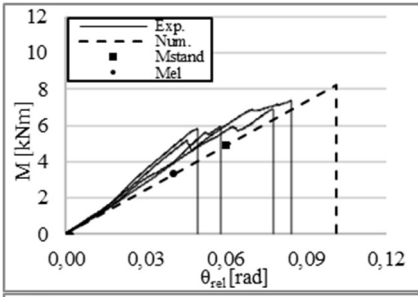
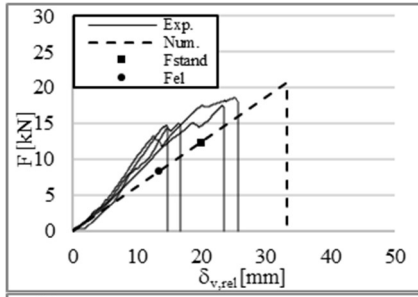
		A.1	A.2	A.3	A.4	A.5	C.1	C.2
$\delta_v^{num}$	[mm]	33.33	27.64	21.00	10.33	28.37	23.73	23.73
$\theta_{conn}^{num}$	[rad]	0.101	0.090	0.070	0.031	0.089	0.082	0.082
$\delta_{v,Gnl}^{num}$	[mm]	13.33	11.05	8.40	4.13	11.34	10.76	10.76
$\delta_{v,CEN}^{num}$	[mm]	19.86	16.47	12.51	6.16	16.90	8.48	8.48

In Figure 77 the comparison between numerical and experimental results is reported in terms of  $F - \delta_v$  and  $M - \theta_{conn}$  curves.

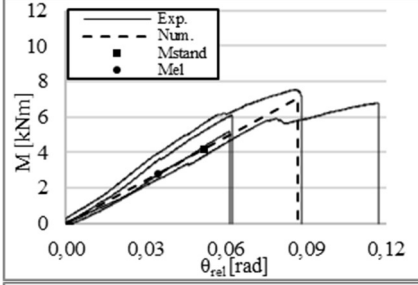
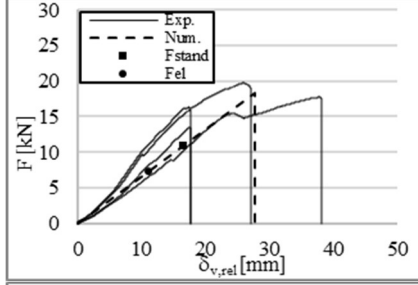
In general, both the strength and the stiffness of the joint is well captured. Furthermore, the following comments about the model capabilities could be addressed:

- It is able to consider the variation of the joint strength in function of the dimension  $b$  (length of the adhesive joint). In particular, with respect to the joint scheme of the Group A.1, which is the reference one, reducing the width  $b$  (from 90 mm to 65mm for the Group A.2 and to 45mm for the Group A.3), the strength decreases as experimentally observed. On the contrary, increasing the width  $b$  of the joint (from 90mm to 120mm for the Group A.5), the joint strength increases accordingly as experimentally already observed;
- It is also able to take into account the variation of joint strength in function of the dimension  $h$  (height of the adhesive layer, sum of the height of the beam and that one of the angles if present). In detail, decreasing the value of  $h$  (from 270mm for the Group A.1 to 150mm for the Group A.4), the joint strength decreases sensibly as experimentally observed;
- It is able to take into account the variation of the mechanical properties of the resin and the GFRP material. In detail, considering the reduction values of the fracture energy and the Young modulus of elasticity due to the hygro-thermal aging, the strength of the joint is very well captured as demonstrated in Figure 77 (Group C.1 and C.2).

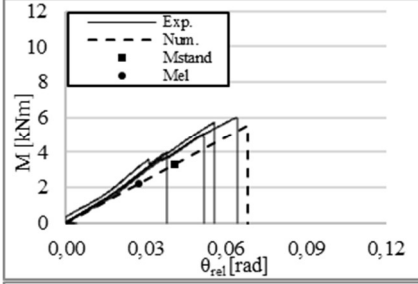
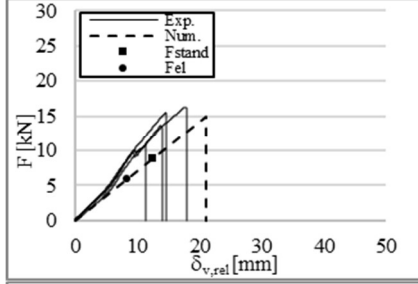
A.1)



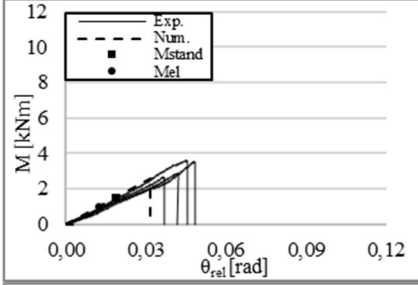
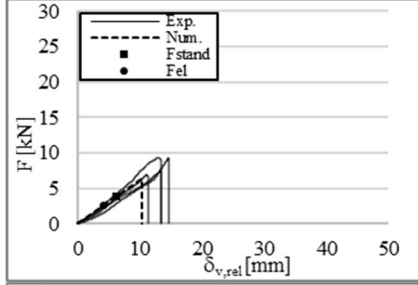
A.2)



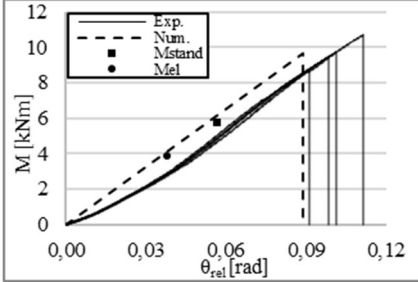
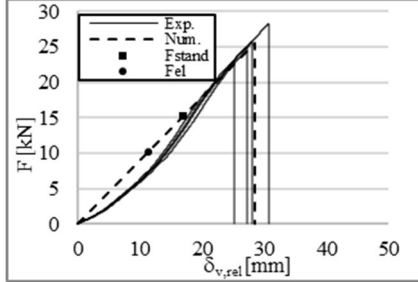
A.3)



A.4)



A.5)



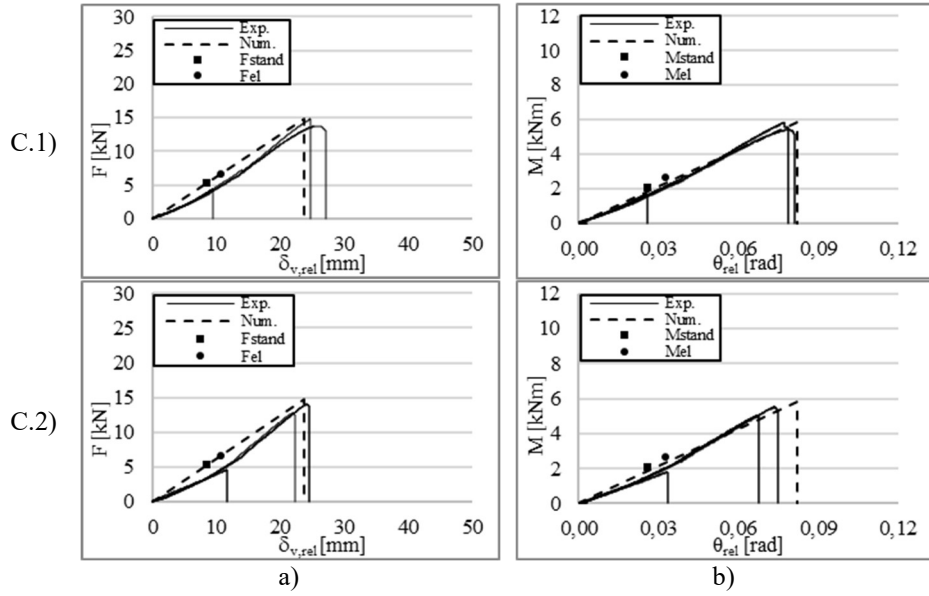


Figure 77. Numerical-Experimental comparison: a)  $F$ - $\delta_v$  curve; b)  $M$ - $\theta_{conn}$  curve.

#### 4.3.1. Further considerations

In Figure 77, other two different design values of the joint strength, in terms of failure load, are reported. The first one, indicated as  $F_{el}$  in Figure 77, is function of the elastic fracture energy only of the resin. The latter is evaluated by means of the force-displacement curve (Figure 78a), obtained by End Notch Failure Test of Figure 78b, by adopting the *Compliance-Based Beam Method* (CBBM) which analytical expression is below reported.

$$G_{II,nl}^{CBBM} = \frac{9 P_{nl}^2 C_{c0} a_0^{\frac{2}{3}}}{2 B (3 a_0^3 + 2 L^3)} \quad (58)$$

$$C_{c0} = C_o - \frac{3 L}{10 G_{13} B h} \quad (59)$$

$$C_o = \frac{\delta}{P_{nl}} \quad (60)$$

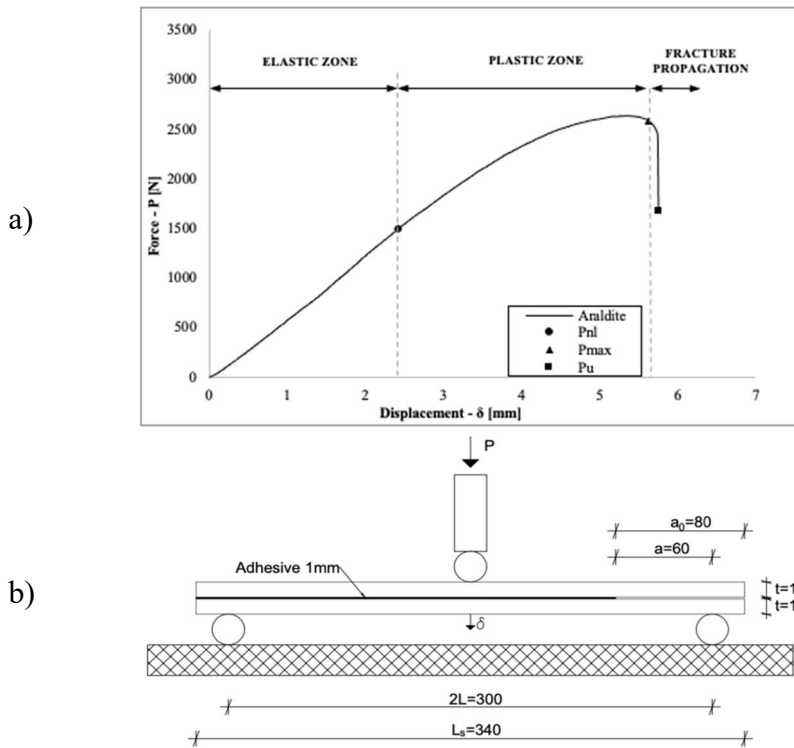


Figure 78. ENF test procedure: a) force-displacement curve for Araldite resin; b) geometry of the ENF tests for the adhesive layer characterization (dimensions in mm).

In Eqs. (58-60) the symbols assume the following meaning:  $P_{nl}$  is the load level  $P$  corresponding to the loss of linearity (nl stands for non-linear) as depicted in Figure 78a;  $\delta$  is the corresponding displacement at the end of the elastic stage;  $C_o$  is the measured initial compliance;  $a_o$  is the initial crack length (Figure 78b);  $B$  is the specimen width;  $L$  is the half of the distance between the supports (distance  $2L$  of Figure 78b) and  $G_{13}$  is the shear modulus of the adherents.

By substituting the elastic fracture energy  $G_{II,nl}^{CBBM}$  into Eqs (51a and 51b) it is possible to evaluate the design value before introduced ( $F_{el}$ ).

Furthermore, the second design value, indicated as  $F_{Stand}$  in Figure 77, is obtained following the instruction of the CEN-TC 250 European Standard [9]. The design strength  $F_{Stand}$  is furnished by the following expression:

$$F_{Stand} = \frac{\eta_c}{\gamma_{M,ac}} F_k \quad (61)$$

In Eqn. (61),  $F_k$  is the characteristic strength value of the adhesive beam-to-column connection (values of Table 26),  $\eta_c$  is conversion factor for taking into account the temperature and moisture effects, which expression is below reported and  $\gamma_{M,ac}$  is the partial factor for adhesive connections.

$$\eta_c = \eta_{ct} \cdot \eta_{cm} \quad (62)$$

In Eqn. (62), the terms  $\eta_{ct}$  is the conversion factor for temperature effects, which value is obtainable by the following formulation:

$$\eta_{ct} = \min \left\{ 1.0 - 0.25 \frac{T_s - 20}{T_g - 20}; 1.0 \right\} \quad (63)$$

where symbols introduced assume the following meanings:  $T_s$  is the maximum temperature in service conditions while  $T_g$  is the glass transition temperature. Values of the conversion factor  $\eta_{cm}$  are summarized in Table 31.

Table 31. Values of for unprotected composite materials and epoxy adhesives.

Exposure classes	Conversion factor	Influence of moisture
I	1.00	Indoor exposure of composite material
II	0.85	Outdoors exposure of composite material without continuous exposure to water, or permanent immersion in water, or permanent exposure to a relative humidity higher than 80%, or combined UV-radiation and frequent freeze-thaw cycles
III	0.60	Continuous exposure of composite material to water (or seawater), or permanent immersion in water (or seawater), or permanent exposure to a relative humidity higher than 80% (material temperature up to 25 °C)

The values of the partial factor  $\gamma_{M,ac}$  are collected in Table 32.

Table 32. Partial factors for adhesive connection resistance.

Inspection and access	Fully controlled application	Partially controlled application
Connection subjected to periodic inspection and maintenance; adhesive connection accessible	1.5	2.0
Connection subjected to periodic inspection and maintenance; limited accessibility	1.7	2.2
Connection not subjected to periodic inspection and maintenance	2.0	2.5

The value of  $T_g$  for the Araldite resin is  $67^\circ\text{C}$  as reported in Table 5 while the value set for  $T_s$  was  $30^\circ\text{C}$  in the case of hygrothermal aging as fixed in the experimental program and  $40^\circ\text{C}$  in the case of unaged connections. The choice of  $40^\circ$  is justified by the fact that such a temperature value represents a realistic outdoor temperature condition in the summer period.

By using the Eqn. (63) the value of the conversion factor  $\eta_{ct}$  assumes the value 0.89 and 0.95 for  $T_s$  equal to  $40^\circ\text{C}$  and  $30^\circ\text{C}$ , respectively. The conversion factor  $\eta_{cm}$  for unaged and aged specimens was set equal to 1.00 and 0.60, respectively. Finally, the values of the partial factor  $\gamma_{M,ac}$  was set equal to 1.50. From Figure 77 it is possible to observe that in all the cases considered the values of  $F_{el}$  and  $F_{Stand}$  are quite similar. This means that the strength design value obtained by standard [20] could be considered a design value corresponding to the adhesive elastic fracture energy only. This circumstance confirms what already stated in the Introduction of the thesis relating to the idea that the adhesive technique is the best one to connect GFRP profiles to each other but limiting their applicability to the linear elastic stage to as o preserve their integrity, while avoiding the classical brittle failure.

#### 4.3.2. Importance of the adhesive layer deformability

In Figure 79 the importance to consider accurately the adhesive layer deformability is demonstrated by comparing the slope of the  $F - \delta_v$  and  $M - \theta_{conn}$  numerical curves (with and without the adhesive layer deformability) with that one of the corresponding experimental curves. Obviously, the experimental curves take into account all the beam and the column elastic deformations. For the sake of brevity, the comparison is limited to Group A.1 only (reference joint configuration).

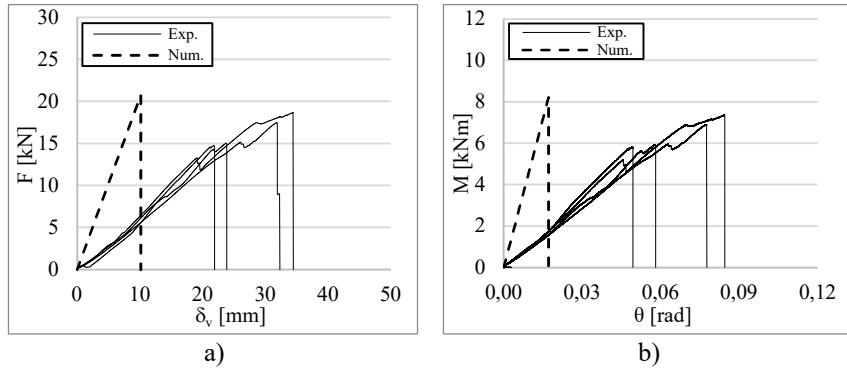


Figure 79. Influence of the adhesive layer deformability (comparison between the experimental and numerical results of the Group A.1: a)  $F$ - $\delta_v$  curve; b)  $M$ - $\theta_{\text{conn}}$  curve.

It is evident that stiffness of the numerical curve, in absence of the adhesive layer deformability (last term of Eqs. 54 and 55), is overestimated (by a 77%).

#### 4.4. Further comparisons with other experimental results

In this section, further comparisons with the experimental results of Razaqpur et al. [13] and Peng et al. [45] are presented and discussed. The two comparisons are pertinent being the joint configuration examined in [13] and in [45]. In detail, in [13] the joint scheme is the same (Figure 80a) but with different geometrical dimensions of the GFRP members as well as different mechanical parameters of both the GFRP and resin elements (the values are reported in Table 33). While in [45], the joint scheme is characterized by a built-up beam analogous and by two hollow columns bonded to each other as depicted in Figure 80b. The connection between the beam and the column is further characterized by steel bolts. The values of all the geometrical and mechanical parameters involved are presented Table 33.

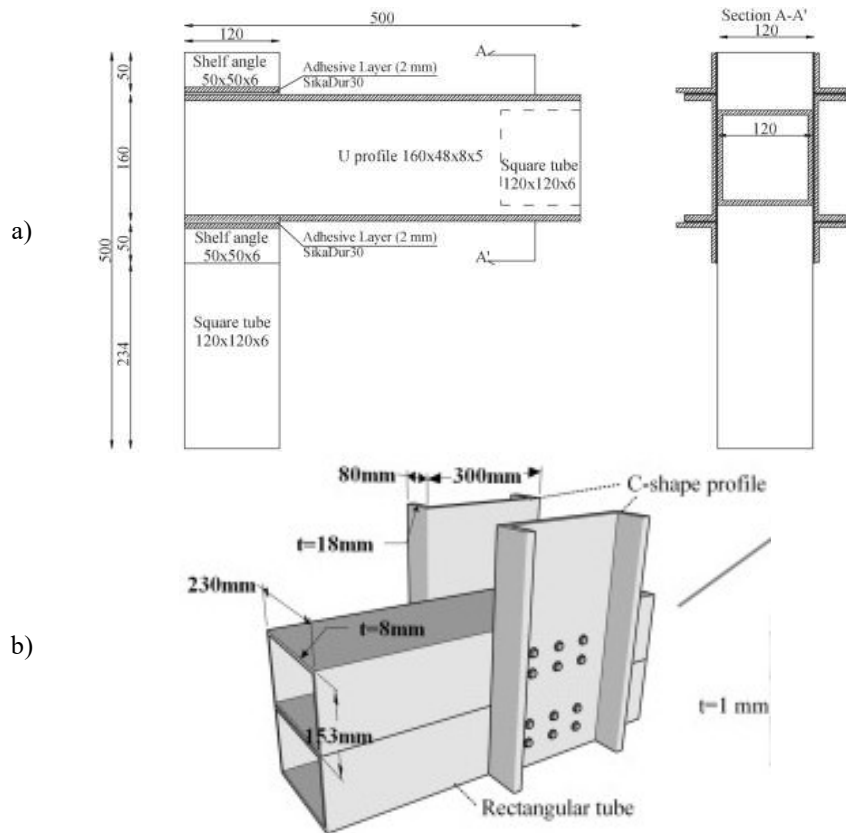


Figure 80. Beam-to-column configuration: a) Razaqpur et al. [13]; b) Peng et al. [45].

The comparison is developed in terms of the joint strength (evaluation of the force  $F$ ) and the joint stiffness (in terms of the slope of the  $F - \delta_v$  and  $M - \theta_{conn}$  curves). The load,  $F$ , was evaluated by adopting Eqn. (51b), while the vertical displacement  $\delta_v$  and the rotation  $\theta_{conn}$  by using Eqn. (54) and Eqn. (55), respectively.

Table 33. Values of the geometrical and mechanical parameters of resin and GFRP material.

Resin										
Group	$\tau_u$ [MPa]	$s_u$ [mm]	$G_{II}$ [N/mm]	$\beta$ [N/mm <sup>3</sup> ]	$t_{layer}$ [mm]	$E_{resin}$ [GPa]	$\omega_s$ [1/mm]	$\gamma$ [-]	$b_{eff}$ [mm]	$b_{SLJ}$ [mm]
Razaqpur et al. [13]	16.00	0.058	0.46	275.86	1.00	11.20	0.107	4.54	14.65	14.65
Peng et al. [45]	13.00	0.040	0.26	325.00		50.00	0.089	9.07	17.69	17.69
GFRP										
	$E_{GFRP}$ [GPa]	$G_{GFRP}$ [GPa]	$d = l_b$ [mm]	$h$ [mm]	$b$ [mm]	column			beam	
						$l_c$ [mm]	$I_c$ [mm <sup>4</sup> ]	$A_c$ [mm <sup>2</sup> ]	$I_b$ [mm <sup>4</sup> ]	$A_b$ [mm <sup>2</sup> ]
Razaqpur et al. [13]	24.00	3.00	404	260	120	170	$5.94 \cdot 10^6$	2736	$1.14 \cdot 10^7$	2976
Peng et al. [45]	41.21		500	300	306	500	$1.14 \cdot 10^8$	8320	$1.70 \cdot 10^8$	15264

All predicted values of the joint strength and stiffness are collected in Table 34.

Table 34. Predicted values of the joint strength and stiffness.

	Razaqpur et al. [13]	Peng et al. [45]
$F$ [kN]	28.36	59.75
$M$ [kNm]	11.46	29.87
$\delta_v$ [mm]	16.04	4.44
$\theta_{conn}$ [rad]	0.033	0.009

In Figures 81 and 82, the comparisons with Razaqpur et al. [13] (in terms of  $F$ - $\delta_v$  and  $M$ - $\theta_{conn}$  curves) and with Peng et al. [45] (in terms of  $M$ - $\theta_{conn}$  curves) are depicted, respectively.

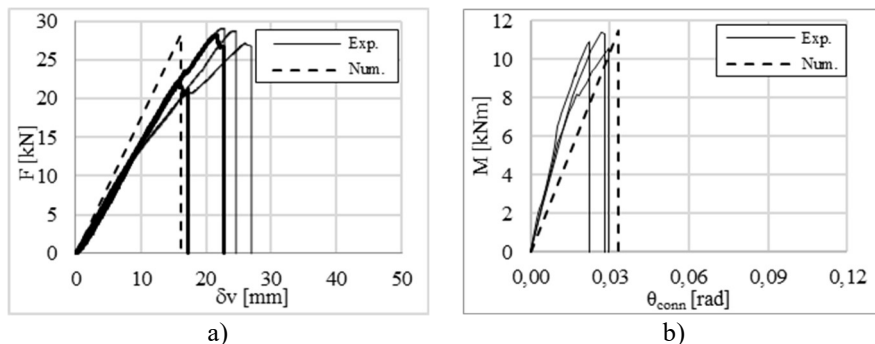


Figure 81. Comparison with Razaqpur [13] e al.: a)  $F$ - $\delta_v$  curves, b)  $M$ - $\theta_{conn}$  curves.

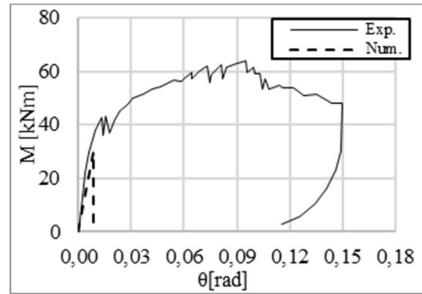


Figure 82. Comparison with Peng [45] e al.:  $M-\theta_{\text{conn}}$  curves.

It is possible to observe a very good correlation between the results with respect to both the strength and stiffness. In particular, regarding the comparison of Figure 81, it is worth highlighting how the formula proposed, for the evaluation of adhesive layer deformability, is able to capture the different influences of the two completely different Young Moduli of the resins adopted (11.2 GPa for SikaDur 30 and 2.0 GPa for Araldite). Furthermore, with reference to the comparison of Figure 82, it is worth highlighting that the comparison is valid when only limited to the initial linear stage (up about 30 kN) relating to the adhesive layer response. As commented in [45], the non-linear behaviour (from 30 kN up to about 60 kN) was due to the plasticization of the steel bolts which was activated only after the adhesive failure.

#### 4.5. Conclusion

Two mechanical models with closed form solutions in order to predict the strength and stiffness of a beam-to-column connection between GFRP profiles are presented. This type of connection is supposed to be subjected to a vertical force applied at the free end of the beam. The bending moment and the shear force, acting on the beam, produce torsion and shear in the adhesive, respectively. From an experimental point of view, it was shown that the tangential stresses due to the shear, acting on the adhesive layer in the vertical direction, are irrelevant with respect to those produced by torsion (acting on the adhesive layer in the horizontal direction also) which have to be considered responsible for the adhesive failure.

Due to the greater influence of the horizontal tangential stresses with respect to the vertical ones, the main idea was to evaluate the strength of the beam-to-column connection by considering the mechanical model of a single lap joint subjected to a traction force (the resultant of the tangential stresses due to

torsion). The mono-dimensional problem previously introduced presents a closed form solution.

Regarding the stiffness, a simple formula to evaluate the adhesive layer deformability is proposed. By means of the Principle of the Virtual Power, the vertical displacement (coupled with the load applied at the free end of the beam) is evaluated and, consequently, the stiffness of the joint is predicted.

The comparison with experimental results available in current literature made it possible to verify the effectiveness of the proposed formulation.



## **PART II: Hybrid GFRP/steel connection suitable for fiber reinforced composite materials**

Object of this Part II of the thesis is the study of an innovative dissipative hybrid beam-to-column connection between pultruded profiles suitable for large scale structures.

The joint was firstly designed and produced, and after tested through a wide experimental program composed of more than seventy full scale specimens.

This topic was developed in collaboration with Professor Luciano Feo from the University of Salerno and with Professors Raffaele Landolfo and Mario D'Aniello from the University of Naples "Federico II".

Thanks to the excellent and encouraging results obtained, the inventors decided to apply for a national/international patent. Because the procedure is still in progress, the author of this Thesis cannot publish any drawing or result about the invention. Consequently, in Chapter V a general description of the invention is only presented underlying the main features.



## **CHAPTER V: The design, production and testing of a dissipative hybrid beam-to-column connection for large scale structures**

Based on the full adhesive beam-to-column connection investigated from an experimental and mechanical point of view in the Part I of this Thesis, a companion hybrid connection was designed, produced and tested. The concept behind this new connection is that fiber reinforced members have to be bonded (in order to preserve the fiber continuity) to steel ones while steel members are bolted each other as usually happened in practice.

The two main scopes of this innovative connection are: 1) to furnish ductility to the system by the introducing of a steel core; 2) to localize the failure in a specific steel element (like a fuse) which could be easily repaired and/or substitute with a new one anticipating and then preventing the failure in the adhesives (which are not easily repairable as is well known).

The connection was tested through a wide experimental program conducted at the Strength Laboratory of the University of Salerno comprises of more than seventy full scale specimens. The quasi-static tests in displacement control were performed using an universal testing machine. The key parameters till now investigated were: 1) the extension of the bonded area between GFRP elements and steel ones; 2) the thickness of the “fuse”.

The results till now obtained are encouraging and the experimental program will continue in the next few months by performing cyclic tests.



## **APPENDICES to the PART I**

### **Appendix A.**

In this appendix all measurement data about absorption are summarized. In particular, the data relative to Araldite and SikaDur 30 resins are collected in Table 35 and Table 36 while data relative to SLJs with Araldite and SikaDur 30 are collected in Tables 37-38. Finally, in Table 39 the data of single GFRP adherents are collected.

Table 35. Data absorption, average and standard deviation values of the resin Araldite.

Time [h]	Tap Water					Sea Water				
	A4	A5	A6	$\mu$	$\sigma^2$	B4	B5	B6	$\mu$	$\sigma^2$
0	0,00	0,00	0,00	0,00	0,00	0,00	0,00	0,00	0,00	0,00
0,5	0,18	0,13	0,19	0,17	0,03	0,34	0,20	0,15	0,23	0,15
1	0,35	0,26	0,36	0,33	0,02	0,54	0,34	0,28	0,39	0,09
2	0,56	0,41	0,59	0,52	0,02	0,82	0,55	0,44	0,60	0,08
4	0,66	0,49	0,72	0,62	0,03	0,94	0,63	0,52	0,70	0,07
8	0,84	0,62	0,91	0,79	0,02	1,14	0,80	0,64	0,86	0,06
24	1,41	1,05	1,52	1,33	0,02	1,67	1,33	1,10	1,37	0,04
28	1,53	1,16	1,69	1,46	0,02	1,95	1,48	1,19	1,54	0,05
32	1,57	1,25	1,80	1,54	0,02	2,00	1,61	1,27	1,63	0,04
48	2,02	1,52	2,14	1,89	0,02	2,43	1,93	1,55	1,97	0,04
52	2,15	1,62	2,28	2,02	0,02	2,56	2,01	1,62	2,07	0,04
72	2,44	1,89	2,58	2,30	0,02	2,71	2,27	1,87	2,28	0,02
80	2,48	1,97	2,68	2,37	0,02	2,85	2,35	1,91	2,37	0,03
96	2,65	2,12	2,85	2,54	0,01	3,02	2,54	2,12	2,56	0,02
102	2,76	2,21	2,92	2,63	0,01	3,09	2,57	2,15	2,60	0,02
170	3,21	2,79	3,33	3,11	0,01	3,57	2,95	2,56	3,02	0,01
195	3,35	2,93	3,42	3,23	0,00	3,63	3,03	2,61	3,09	0,01
220	3,47	3,04	3,46	3,32	0,00	3,67	3,08	2,68	3,14	0,01
245	3,54	3,11	3,54	3,40	0,00	3,73	3,10	2,70	3,18	0,01
270	3,61	3,15	3,60	3,46	0,00	3,78	3,14	2,76	3,23	0,01
340	3,81	3,32	3,69	3,60	0,00	3,78	3,17	2,85	3,27	0,00
365	3,84	3,36	3,76	3,65	0,00	3,81	3,19	2,88	3,29	0,00
390	3,90	3,42	3,79	3,70	0,00	3,84	3,27	2,96	3,36	0,00
415	3,94	3,45	3,83	3,74	0,00	3,86	3,28	2,98	3,37	0,00
440	3,94	3,45	3,88	3,75	0,00	3,88	3,28	2,99	3,38	0,00
510	4,03	3,58	4,00	3,87	0,00	3,96	3,32	3,04	3,44	0,00
535	4,08	3,62	4,02	3,91	0,00	3,96	3,35	3,07	3,46	0,00
560	4,09	3,70	4,05	3,95	0,00	3,99	3,39	3,08	3,49	0,00
585	4,13	3,74	4,08	3,98	0,00	4,00	3,40	3,09	3,50	0,00
610	4,15	3,77	4,10	4,01	0,00	4,02	3,42	3,11	3,52	0,00
680	4,17	3,80	4,13	4,03	0,00	4,02	3,43	3,13	3,53	0,00
705	4,19	3,82	4,15	4,05	0,00	4,03	3,45	3,14	3,54	0,00
730	4,19	3,83	4,15	4,06	0,00	4,02	3,45	3,14	3,54	0,00
755	4,19	3,83	4,15	4,06	0,00	4,02	3,45	3,15	3,54	0,00
780	4,19	3,83	4,15	4,06	0,00	4,02	3,45	3,14	3,54	0,00
850	4,19	3,83	4,15	4,06	0,00	4,03	3,45	3,15	3,54	0,00

$\mu$  = average values;  $\sigma^2$  = standard deviation

Table 36. Data absorption, average and standard deviation values of the resin SikaDur 30.

Time [h]	Tap Water					Sea Water				
	A1	A2	A3	$\mu$	$\sigma^2$	B1	B2	B3	$\mu$	$\sigma^2$
0	0,00	0,00	0,00	0,00	0,00	0,00	0,00	0,00	0,00	0,00
0,5	0,20	0,07	0,05	0,11	0,40	0,06	0,04	0,07	0,06	0,04
1	0,23	0,10	0,07	0,13	0,28	0,10	0,11	0,09	0,10	0,01
2	0,23	0,11	0,07	0,14	0,25	0,10	0,13	0,09	0,11	0,03
4	0,33	0,14	0,11	0,19	0,25	0,13	0,15	0,12	0,13	0,01
8	0,34	0,14	0,11	0,20	0,26	0,13	0,16	0,14	0,14	0,00
24	0,38	0,20	0,18	0,25	0,12	0,21	0,21	0,20	0,21	0,00
28	0,42	0,22	0,20	0,28	0,13	0,23	0,23	0,25	0,23	0,00
32	0,46	0,24	0,23	0,31	0,12	0,24	0,25	0,32	0,27	0,02
48	0,47	0,25	0,23	0,32	0,11	0,25	0,28	0,34	0,29	0,02
52	0,48	0,27	0,25	0,33	0,10	0,26	0,31	0,35	0,30	0,01
56	0,49	0,28	0,27	0,35	0,08	0,28	0,32	0,36	0,32	0,01
72	0,51	0,30	0,30	0,37	0,07	0,29	0,37	0,43	0,36	0,02
80	0,54	0,32	0,31	0,39	0,08	0,33	0,38	0,46	0,39	0,02
96	0,63	0,37	0,31	0,44	0,10	0,43	0,48	0,50	0,47	0,00
102	0,66	0,39	0,37	0,47	0,08	0,45	0,51	0,52	0,49	0,00
170	0,70	0,42	0,40	0,50	0,07	0,49	0,52	0,54	0,51	0,00
195	0,71	0,50	0,43	0,55	0,05	0,52	0,57	0,62	0,57	0,00
220	0,74	0,52	0,46	0,57	0,05	0,56	0,58	0,67	0,60	0,01
245	0,75	0,56	0,48	0,59	0,04	0,60	0,62	0,69	0,64	0,00
270	0,75	0,60	0,52	0,62	0,02	0,62	0,64	0,71	0,66	0,00
340	0,77	0,67	0,57	0,67	0,01	0,63	0,64	0,72	0,67	0,00
365	0,78	0,68	0,59	0,68	0,01	0,65	0,64	0,73	0,67	0,00
390	0,78	0,69	0,59	0,69	0,01	0,67	0,65	0,73	0,69	0,00
415	0,77	0,71	0,61	0,70	0,01	0,70	0,65	0,74	0,70	0,00
440	0,77	0,72	0,62	0,71	0,01	0,72	0,66	0,75	0,71	0,00
510	0,78	0,83	0,63	0,75	0,01	0,70	0,66	0,75	0,70	0,00
535	0,78	0,83	0,66	0,76	0,01	0,70	0,67	0,75	0,70	0,00
560	0,78	0,83	0,68	0,76	0,01	0,70	0,67	0,76	0,71	0,00
585	0,78	0,83	0,71	0,77	0,00	0,70	0,67	0,76	0,71	0,00
610	0,78	0,83	0,72	0,78	0,00	0,70	0,68	0,75	0,71	0,00
680	0,78	0,83	0,73	0,78	0,00	0,70	0,67	0,75	0,71	0,00
705	0,78	0,83	0,73	0,78	0,00	0,70	0,68	0,76	0,71	0,00
730	0,78	0,83	0,73	0,78	0,00	0,70	0,67	0,76	0,71	0,00
755	0,78	0,83	0,73	0,78	0,00	0,70	0,68	0,76	0,71	0,00
780	0,78	0,83	0,73	0,78	0,00	0,70	0,67	0,76	0,71	0,00
850	0,78	0,83	0,73	0,78	0,00	0,70	0,68	0,76	0,71	0,00
900	0,78	0,83	0,73	0,78	0,00	0,70	0,67	0,76	0,71	0,00

$\mu$  = average values;  $\sigma^2$  = standard deviation

Table 37. Data absorption, average and standard deviation values of the SLJs with Araldite.

Time [d]	Tap Water					Sea Water				
	1	2	3	$\mu$	$\sigma^2$	1	2	3	$\mu$	$\sigma^2$
0	0,00	0,00	0,00	0,00	0,00	0,00	0,00	0,00	0,00	0,00
1	0,69	0,76	0,72	0,72	0,00	0,53	0,30	0,36	0,40	0,06
2	0,99	1,04	0,98	1,00	0,00	0,65	0,42	0,42	0,49	0,05
3	1,22	1,25	1,28	1,25	0,00	0,79	0,48	0,50	0,59	0,06
4	1,41	1,49	1,45	1,45	0,00	0,84	0,55	0,59	0,66	0,04
7	1,85	1,91	1,96	1,91	0,00	1,05	0,65	0,70	0,80	0,05
8	1,89	1,94	2,08	1,97	0,00	1,10	0,66	0,73	0,83	0,06
9	2,02	2,08	2,20	2,10	0,00	1,15	0,71	0,76	0,87	0,05
10	2,07	2,12	2,25	2,15	0,00	1,16	0,75	0,81	0,91	0,04
14	2,40	2,41	2,62	2,48	0,00	1,38	0,88	0,92	1,06	0,05
15	2,38	2,36	2,60	2,45	0,00	1,34	0,84	0,94	1,04	0,04
16	2,43	2,43	2,72	2,53	0,00	1,43	0,90	0,93	1,09	0,05
17	2,51	2,57	2,82	2,63	0,00	1,49	0,97	0,99	1,15	0,04
21	2,67	2,59	2,93	2,73	0,00	1,63	1,02	1,09	1,24	0,05
22	2,78	2,69	2,94	2,80	0,00	1,67	1,14	1,16	1,32	0,03
23	2,73	2,64	2,96	2,78	0,00	1,61	1,08	1,12	1,27	0,04
24	2,76	2,71	3,02	2,83	0,00	1,71	1,17	1,18	1,35	0,03
28	2,91	2,82	3,11	2,95	0,00	1,86	1,30	1,33	1,50	0,03
31	2,92	2,82	3,11	2,95	0,00	1,86	1,28	1,31	1,48	0,03
35	3,03	2,88	3,15	3,02	0,00	1,96	1,37	1,41	1,58	0,03
38	3,07	2,93	3,21	3,07	0,00	2,10	1,49	1,55	1,71	0,03
42	3,14	3,03	3,28	3,15	0,00	2,22	1,62	1,68	1,84	0,02
45	3,14	3,03	3,34	3,17	0,00	2,30	1,72	1,73	1,91	0,02
49	3,19	3,04	3,26	3,16	0,00	2,27	1,75	1,75	1,92	0,02
56	3,22	3,13	3,38	3,24	0,00	2,59	2,00	2,02	2,20	0,02
63	3,27	3,17	3,35	3,26	0,00	2,62	2,05	2,10	2,26	0,01
86	3,35	3,23	3,38	3,32	0,00	2,98	2,46	2,55	2,66	0,01
115	3,33	3,23	3,38	3,31	0,00	3,22	2,78	2,83	2,94	0,00
172	3,45	3,32	3,45	3,41	0,00	3,47	3,20	3,21	3,29	0,00
262	3,48	3,35	3,48	3,44	0,00	3,50	3,38	3,39	3,42	0,00
378	3,47	3,37	3,51	3,45	0,00	3,64	3,43	3,44	3,50	0,00

$\mu$  = average values;  $\sigma^2$  = standard deviation

Table 38. Data absorption, average and standard deviation values of the SLJs with SikaDur 30.

Time [d]	Tap Water					Sea Water				
	11	12	16	$\mu$	$\sigma^2$	2	14	20	$\mu$	$\sigma^2$
0	0,00	0,00	0,00	0,00	0,00	0,00	0,00	0,00	0,00	0,00
1	0,48	0,54	0,54	0,52	0,00	0,25	0,31	0,39	0,32	0,03
2	0,79	0,77	0,79	0,78	0,00	0,33	0,39	0,45	0,39	0,01
3	1,00	0,96	0,99	0,98	0,00	0,44	0,47	0,60	0,50	0,02
4	1,29	1,24	1,24	1,25	0,00	0,46	0,54	0,56	0,52	0,01
7	1,81	1,71	1,68	1,73	0,00	0,64	0,69	0,78	0,70	0,01
8	1,86	1,75	1,79	1,80	0,00	0,66	0,68	0,79	0,71	0,01
9	1,93	1,83	1,88	1,88	0,00	0,66	0,67	0,79	0,71	0,01
10	2,04	1,92	1,96	1,98	0,00	0,71	0,75	0,80	0,75	0,00
11	2,11	2,00	2,02	2,04	0,00	0,76	0,87	0,83	0,82	0,00
14	2,29	2,13	2,18	2,20	0,00	0,79	0,83	0,85	0,82	0,00
15	2,32	2,20	2,29	2,27	0,00	0,90	0,84	0,92	0,89	0,00
16	2,32	2,22	2,23	2,26	0,00	0,90	0,84	0,94	0,89	0,00
17	2,32	2,24	2,23	2,27	0,00	0,84	0,88	0,94	0,89	0,00
18	2,40	2,28	2,35	2,34	0,00	0,92	0,97	1,00	0,96	0,00
21	2,50	2,40	2,45	2,45	0,00	1,02	1,12	1,11	1,08	0,00
22	2,56	2,43	2,51	2,50	0,00	1,05	1,13	1,18	1,12	0,00
23	2,62	2,47	2,54	2,54	0,00	1,07	1,13	1,26	1,15	0,00
24	2,62	2,53	2,62	2,59	0,00	1,16	1,24	1,25	1,22	0,00
28	2,67	2,64	2,64	2,65	0,00	1,21	1,36	1,34	1,30	0,00
29	2,74	2,67	2,71	2,71	0,00	1,29	1,42	1,42	1,38	0,00
30	2,72	2,65	2,68	2,68	0,00	1,27	1,41	1,45	1,38	0,00
31	2,67	2,71	2,71	2,69	0,00	1,26	1,33	1,35	1,31	0,00
35	2,77	2,68	2,78	2,74	0,00	1,42	1,53	1,56	1,50	0,00
38	2,81	2,76	2,77	2,78	0,00	1,46	1,54	1,60	1,53	0,00
43	2,79	2,75	2,84	2,80	0,00	1,57	1,70	1,68	1,65	0,00
50	2,84	2,77	2,86	2,83	0,00	1,89	2,02	1,74	1,88	0,00
86	2,87	2,88	2,96	2,90	0,00	2,55	2,66	2,66	2,62	0,00
91	2,94	2,95	2,99	2,96	0,00	2,70	2,77	2,74	2,73	0,00
98	2,89	2,84	2,95	2,89	0,00	2,75	2,80	2,76	2,77	0,00
105	2,92	2,98	2,98	2,96	0,00	2,85	2,91	2,96	2,90	0,00
112	2,96	2,88	2,97	2,94	0,00	2,90	2,87	2,96	2,91	0,00
126	2,96	2,91	2,94	2,94	0,00	2,95	3,00	2,99	2,98	0,00
140	2,94	2,91	2,92	2,92	0,00	3,03	3,09	3,09	3,07	0,00
154	3,04	2,94	2,99	2,99	0,00	3,06	3,10	3,05	3,07	0,00
191	3,04	2,95	3,01	3,00	0,00	3,05	3,19	3,16	3,13	0,00
220	2,96	2,95	2,98	2,96	0,00	3,08	3,08	3,20	3,12	0,00
277	2,96	2,95	2,98	2,96	0,00	3,08	3,08	3,20	3,12	0,00
367	2,98	2,95	3,03	2,99	0,00	3,13	3,08	3,20	3,14	0,00

483 | 2,97 2,98 3,05 3,00 0,00 | 3,13 3,09 3,21 3,15 0,00  
 $\mu$  = average values;  $\sigma^2$  = standard deviation

Table 39. Data absorption of the GFRP adherents.

Time [d]	Tap Water	Sea Water
0	0,00	0,00
1	0,44	0,24
2	0,65	0,30
3	0,81	0,46
4	1,00	0,53
7	1,37	0,70
8	1,51	0,65
9	1,58	0,64
10	1,65	0,63
11	1,72	0,68
14	1,88	0,77
15	1,92	0,80
16	1,99	0,75
17	1,99	0,76
18	2,02	0,86
21	2,18	0,91
22	2,22	0,93
23	2,25	0,95
24	2,32	1,04
28	2,42	1,04
29	2,45	1,05
30	2,47	1,04
31	2,51	1,08
35	2,61	1,26
38	2,64	1,23
43	2,71	1,29
50	2,84	1,63
86	2,99	2,25
91	3,04	2,37
98	2,94	2,39
105	2,99	2,54
112	2,97	2,66
126	2,94	2,71
140	2,92	2,75
154	2,98	2,92
191	3,01	2,93
220	3,02	3,01
277	3,02	3,01
367	3,07	3,04
483	3,17	3,22



## **Appendix B.**

In this appendix all test results are reported. In particular, results collected in Tables 40 and 41 are referred to specimens of Araldite and SikaDur 30, respectively. Furthermore, in Tables 42 and 43 are collected all the results in terms of average and standard deviations values.

For the sake of simplicity each specimen is labelled as follows: AR = Araldite, SD30 = SikaDur30, U = Unaged, SW = aged in sea water and TW = aged in tap water.

It is worth to underline that test conducted but not counted is indicated in () per each table.

Table 40. All test results relative to Araldite specimens.

Unaged specimens										
	Specimen	$P_{nl}$ [N]	$\delta_{nl}$ [mm]	$G_{II, nl}$ [N/mm]	$P_{max,5\%}$ [N]	$\delta_{max,5\%}$ [mm]	$G_{II, max,5\%}$ [N/mm]	$P_u$ [N]	$\delta_u$ [mm]	$G_{II, u}$ [N/mm]
	ARU#1	2010	3,17	0,54	2064	3,29	0,62	1897	3,66	1,14
	(ARU#2)	870	1,50	0,11	893	1,56	0,13	878	1,60	0,16
	ARU#3	1500	2,42	0,31	2250	3,82	0,95	2443	5,75	2,81
	ARU#4	2350	3,92	0,78	4000	7,02	3,11	4516	9,61	7,56
	ARU#5	2350	3,67	0,73	4200	6,91	3,21	2908	7,71	4,91
	(ARU#6)	2600	6,27	1,39	3500	8,88	3,47	3113	9,56	5,20
Sea-water conditioned specimens										
Months	Specimen	$P_{nl}$ [N]	$\delta_{nl}$ [mm]	$G_{II, nl}$ [N/mm]	$P_{max,5\%}$ [N]	$\delta_{max,5\%}$ [mm]	$G_{II, max,5\%}$ [N/mm]	$P_u$ [N]	$\delta_u$ [mm]	$G_{II, u}$ [N/mm]
1	ARSW#4	1380	2,76	0,32	1630	3,43	0,62	1837	7,39	3,16
	ARSW#5	760	1,62	0,10	950	2,13	0,23	1325	5,00	1,48
	(ARSW#6)	2750	16,98	4,05	2764	17,27	4,47	2166	18,03	7,36
	ARSW#32	1420	2,78	0,33	1651	3,48	0,69	1910	7,68	3,20
	ARSW#33	1820	3,96	0,61	2350	5,38	1,41	1900	6,67	2,72
2	(ARSW#7)	650	1,44	0,08	750	1,75	0,15	2880	16,50	11,44
	ARSW#8	2100	3,50	0,62	2900	5,09	1,63	3485	8,08	5,41
	ARSW#9	1680	3,21	0,51	2552	5,02	1,58	3010	7,89	5,32
	ARSW#34	1650	3,06	0,43	2450	4,78	1,30	3063	8,64	5,48
	ARSW#35	2100	3,75	0,67	2700	5,08	1,52	4460	10,27	8,10
3	ARSW#10	1070	3,04	0,27	1235	3,64	0,49	1062	4,38	1,01
	ARSW#11	1130	2,92	0,28	1230	3,35	0,47	1548	4,31	1,00
	ARSW#12	1095	2,97	0,27	1230	3,42	0,48	1060	4,45	1,01
4	(ARSW#13)	790	1,93	0,13	880	2,26	0,22	864	2,57	0,36
	(ARSW#14)	1130	1,98	0,19	1500	2,77	0,46	1851	6,21	2,64
5	ARSW#16	1350	2,62	0,30	1680	3,43	0,64	1914	4,68	1,53
	ARSW#17	1100	2,44	0,23	1700	3,98	0,75	2744	9,28	5,28
	ARSW#38	1540	5,02	0,63	1870	6,45	1,36	1878	8,64	3,31
	ARSW#39	1850	5,61	0,89	2300	7,34	1,89	2325	9,25	3,91
6	ARSW#36	2250	6,82	1,32	2650	8,45	2,51	2497	9,29	3,85
	ARSW#37	1150	2,61	0,26	2050	4,90	1,12	3075	9,27	5,23
	ARSW#44	2550	7,29	1,59	2950	8,87	2,93	2670	9,51	4,31
	ARSW#40	1450	3,58	0,44	1950	5,07	1,10	2323	8,17	3,74
	ARSW#41	1950	7,65	1,29	2550	10,53	3,02	2532	11,17	3,94
9	ARSW#25	1000	3,13	0,27	1130	3,72	0,47	1328	5,84	1,52
	ARSW#15	1050	2,96	0,27	1380	4,09	0,63	1557	6,44	2,03
	ARSW#18	1200	2,67	0,27	1550	3,63	0,63	2835	9,97	6,00
	ARSW#19	1350	2,55	0,29	1550	3,08	0,53	1455	3,35	0,80
	ARSW#22	1250	3,05	0,33	1850	4,75	0,98	3076	8,98	4,37
12	ARSW#23	1550	5,00	0,67	1930	6,55	1,42	1830	8,85	3,34

	ARSW#24	1340	2,78	0,64	2297	8,30	1,95	1966	8,92	3,14
	ARSW#31	1600	5,71	0,79	1900	7,14	1,53	1900	9,39	3,44
	ARSW#20	1230	2,69	0,28	2200	8,91	2,21	2046	9,57	3,21
	(ARSW#21)	1150	2,84	0,28	1250	3,25	0,45	1237	4,37	1,07
	(ARSW#28)	330	1,27	0,04	420	1,70	0,08	681	3,69	0,49

Tap-water conditioned specimens

Months	Specimen	$P_{nl}$	$\delta_{nl}$	$G_{II, nl}$	$P_{max,5\%}$	$\delta_{max,5\%}$	$G_{II, max,5\%}$	$P_u$	$\delta_u$	$G_{II, u}$
		[N]	[mm]	[N/mm]	[N]	[mm]	[N/mm]	[N]	[mm]	[N/mm]
1	ARTW#4	1340	3,27	0,37	1870	4,80	1,00	1558	5,79	1,87
	ARTW#5	1150	2,37	0,23	1330	2,89	0,43	2448	8,77	4,77
	ARTW#6	1390	2,87	0,34	1600	3,47	0,62	1846	5,11	1,75
2	ARTW#7	2050	4,02	0,70	2900	5,99	1,93	4306	10,32	7,27
	ARTW#8	1300	3,38	0,38	1600	4,37	0,78	2586	11,63	6,69
	ARTW#9	1330	3,45	0,45	1700	4,56	0,83	3462	10,18	7,14
3	(ARTW#10)	1700	3,62	0,52	2480	5,55	1,54	3939	11,75	8,98
	ARTW#11	380	0,81	0,03	440	0,99	0,05	2705	13,27	8,53
	ARTW#12	1620	3,51	0,48	2360	5,18	1,45	3785	11,08	8,13
4	(ARTW#13)	690	1,68	0,10	980	2,52	0,28	1030	2,89	0,44
	(ARTW#14)	360	1,20	0,04	381	1,32	0,05	363	1,42	0,08
5	ARTW#16	1550	5,20	0,68	1780	6,19	1,21	1810	7,94	2,86
	ARTW#17	1430	4,12	0,49	1725	5,25	1,04	1810	7,04	2,38
	ARTW#33	1500	5,00	0,65	1730	6,07	1,18	1721	8,10	2,74
	ARTW#34	1450	4,14	0,52	1750	5,26	1,03	1820	7,10	2,45
6	(ARTW#31)	2650	7,16	1,63	3250	9,25	3,36	3265	10,63	5,56
	ARTW#32	1800	6,67	1,03	2000	7,80	1,75	2064	9,72	3,51
	ARTW#35	1650	4,78	0,68	1850	5,64	1,17	1682	7,62	2,71
	ARTW#36	2000	5,41	0,93	2450	6,97	1,91	2514	8,34	3,47
	ARTW#37	1850	7,25	1,16	1946	7,90	1,61	1732	8,29	2,36
9	ARTW#15	1280	3,56	0,37	1450	4,12	0,68	1080	4,60	1,05
	ARTW#18	1090	3,06	0,28	1180	3,74	0,53	1090	4,58	0,99
	ARTW#19	1120	2,94	0,29	1320	3,45	0,47	1045	4,12	0,98
	ARTW#20	1400	3,89	0,47	1950	5,70	1,25	1767	7,51	2,77
	(ARTW#21)	2450	15,71	3,34	2467	15,99	3,66	2435	16,27	4,29
12	ARTW#22	1080	3,04	0,28	1250	3,71	0,52	1078	4,59	1,02
	ARTW#23	1120	2,91	0,28	1220	3,34	0,46	1056	4,40	1,00
	ARTW#24	350	1,09	0,03	560	1,84	0,12	891	3,76	0,63
	ARTW#30	630	2,07	0,11	780	2,69	0,24	1127	4,76	0,96
	ARTW#29	1280	3,88	0,43	1338	4,20	0,59	1147	4,69	1,01

(.) discarded

Table 41. All test results relative to SikaDur30 specimens.

Unaged specimens										
	Specimen	$P_{nl}$	$\delta_{nl}$	$G_{II, nl}$	$P_{max,5}$	$\delta_{max,5\%}$	$G_{II, max,5\%}$	$P_u$	$\delta_u$	$G_{II, u}$
		[N]	[mm]	[N/mm]	[N]	[mm]	[N/mm]	[N]	[mm]	[N/mm]
	SD30U#1	1300	2,50	0,28	1462	2,94	0,47	1406	2,80	0,54
	SD30U#2	1115	2,06	0,20	1134	2,12	0,22	917	1,91	0,30
	SD30U#3	1620	2,61	0,36	1659	2,70	0,40	1506	2,49	0,51
	(SD30U#4)	3750	5,32	1,67	3837	5,47	1,82	2890	5,49	2,92
	SD30U#5	2100	3,04	0,62	2055	3,14	0,77	1640	2,98	0,88
	SD30U#6	1750	2,57	0,43	1808	2,68	0,49	1362	2,69	0,68
Sea-water conditioned specimens										
Months	Specimen	$P_{nl}$	$\delta_{nl}$	$G_{II, nl}$	$P_{max,5}$	$\delta_{max,5\%}$	$G_{II, max,5\%}$	$P_u$	$\delta_u$	$G_{II, u}$
		[N]	[mm]	[N/mm]	[N]	[mm]	[N/mm]	[N]	[mm]	[N/mm]
1	SD30SW#23	780	1,32	0,09	830	1,48	0,14	799	1,67	0,22
	SD30SW#24	1440	2,15	0,26	1457	2,22	0,31	863	2,25	0,43
	SD30SW#25	1630	2,32	0,32	1618	2,27	0,35	925	2,36	0,47
3	SD30SW#13	1290	2,10	0,23	1294	2,11	0,24	887	2,12	0,38
	SD30SW#17	2280	3,56	0,68	2363	3,83	0,94	1745	3,88	1,33
	SD30SW#29	1350	2,17	0,28	1780	2,45	0,45	1650	3,12	1,02
4	SD30SW#1	3150	4,63	1,23	3163	4,67	1,27	1967	4,80	2,04
	SD30SW#3	3080	4,34	1,12	3133	4,47	1,27	1996	4,93	2,18
	SD30SW#4	2980	4,26	1,06	3321	4,83	1,51	2255	4,86	2,25
5	SD30SW#5	1760	2,47	0,36	1875	2,74	0,45	1740	3,22	0,79
	SD30SW#6	2380	3,58	0,72	2409	3,67	0,81	2034	3,85	1,33
	SD30SW#7	1800	2,61	0,39	1936	2,92	0,59	1870	3,23	0,94
6	(SD30SW#8)	3180	4,36	1,16	3170	4,57	1,60	2095	5,25	2,48
	(SD30SW#9)	700	1,46	0,09	720	1,58	0,13	557	1,59	0,17
	SD30SW#10	2680	3,83	0,86	2725	4,00	1,08	1929	4,30	1,74
	SD30SW#35	2650	3,79	0,84	2806	4,13	1,16	2021	4,17	1,67
	SD30SW#36	2850	3,85	0,92	2991	4,12	1,16	1931	4,16	1,70
	SD30SW#37	2650	3,53	0,78	2669	3,61	0,89	1818	3,65	1,36
9	SD30SW#32	2480	3,59	0,75	2721	4,02	1,04	1642	4,06	1,46
	SD30SW#33	2380	3,66	0,73	2560	4,15	1,17	2033	4,17	1,56
	(SD30SW#34)	1180	2,23	0,22	1980	3,93	0,87	2185	5,73	2,41
	SD30SW#38	2150	2,95	0,53	2272	3,20	0,72	1183	3,24	0,88
	SD30SW#39	2280	3,12	0,60	2791	3,96	1,13	1959	4,02	1,60
12	SD30SW#26	1150	1,72	0,17	1169	1,80	0,21	765	1,83	0,30
	SD30SW#28	1480	1,85	0,28	2274	3,21	0,72	1071	3,23	0,81
	SD30SW#30	1285	1,76	0,19	1293	1,79	0,21	1283	1,82	0,24
	SD30SW#11	1180	1,76	0,17	1217	1,89	0,24	1037	2,22	0,45

	(SD30SW#15)	850	1,47	0,11	900	1,63	0,16	911	1,66	0,17
	SD30SW#16	2750	3,72	0,86	2773	3,81	0,98	1920	3,85	1,49
15	SD30SW#19	1180	2,00	0,20	1540	2,75	0,47	1418	3,41	0,94
	SD30SW#21	1830	2,86	0,44	1990	3,27	0,72	1898	3,31	0,86
	SD30SW#22	1850	2,85	0,44	1970	3,19	0,69	1979	3,35	0,86
	SD30SW#31	1620	2,28	0,31	1622	2,29	0,31	931	2,33	0,48
	(SD30SW#12)	3070	4,51	1,16	3270	5,06	1,83	1971	5,10	2,23
	SD30SW#18	980	1,66	0,14	1087	1,92	0,22	698	1,97	0,30

Tap-water conditioned specimens

Months	Specimen	$P_{nl}$	$\delta_{nl}$	$G_{II, nl}$	$P_{max,5\%}$	$\delta_{max,5\%}$	$G_{II, max,5\%}$	$P_u$	$\delta_u$	$G_{II, u}$
		[N]	[mm]	[N/mm]	[%]	[mm]	[N/mm]	[N]	[mm]	[N/mm]
1	SD30TW#4	950	1,56	0,12	950	1,56	0,13	900	1,60	0,18
	SD30TW#7	980	1,75	0,09	1044	1,92	0,15	793	2,06	0,20
	SD30TW#30	2850	4,04	0,97	3211	4,65	1,42	2241	4,66	2,09
3	SD30TW#2	2150	3,47	0,63	2350	3,92	0,94	1891	4,39	1,64
	SD30TW#8	640	1,16	0,06	653	1,20	0,07	541	1,32	0,13
	SD30TW#32	1460	2,07	0,25	1470	2,11	0,28	1108	2,13	0,44
4	SD30TW#1	2050	3,31	0,57	2047	3,32	0,59	1761	3,53	1,04
	SD30TW#3	550	1,10	0,05	574	1,17	0,06	446	1,34	0,12
	SD30TW#5	1840	2,79	0,41	1975	3,14	0,68	1972	3,28	0,84
5	SD30TW#6	1900	2,60	0,41	1935	2,69	0,48	1327	2,75	0,75
	(SD30TW#9)	3050	4,42	1,13	3470	5,23	1,89	2269	5,28	2,55
	SD30TW#10	1600	2,16	0,29	1674	2,30	0,36	1072	2,37	0,55
	SD30TW#37	2450	3,36	0,69	2685	3,79	1,02	1730	3,86	1,44
	SD30TW#38	2550	3,81	0,82	2618	3,99	1,00	1926	4,09	1,54
6	SD30TW#13	1350	1,99	0,23	1371	2,03	0,24	821	2,21	0,41
	SD30TW#14	1170	1,72	0,17	1140	1,76	0,22	1113	2,23	0,47
	SD30TW#15	1462	3,06	0,39	1535	3,28	0,55	1497	3,48	0,71
	SD30TW#39	1380	4,84	0,58	1475	5,45	0,90	1405	6,60	1,73
	SD30TW#40	2350	3,31	0,65	2653	3,85	1,02	1895	3,89	1,47
	SD30TW#36	2300	3,33	0,64	2490	3,73	0,95	1736	3,82	1,37
9	SD30TW#33	2270	3,31	0,63	2359	3,55	0,84	1701	3,65	1,25
	SD30TW#34	2480	3,62	0,75	2557	3,79	0,90	1682	3,82	1,34
	SD30TW#35	2290	3,47	0,67	2330	3,60	0,79	1394	3,69	1,14
	SD30TW#41	2320	3,36	0,65	2342	3,44	0,74	1588	3,48	1,13
12	SD30TW#21	2320	3,46	0,68	2426	3,73	0,90	1752	3,79	1,32
	SD30TW#22	1130	1,71	0,16	1137	1,74	0,18	859	1,77	0,28
	SD30TW#23	1220	1,67	0,17	1223	1,70	0,19	869	1,74	0,30
	SD30TW#24	2570	3,52	0,76	2589	3,63	0,90	1676	3,78	1,36
	SD30TW#31	1050	1,60	0,14	1082	1,68	0,17	617	1,80	0,25
	(SD30TW#17)	2950	3,96	0,98	3069	4,19	1,20	2040	4,24	1,80

	SD30TW#18	2730	3,69	0,84	2742	3,72	0,88	1723	3,74	1,37
	(SD30TW#25)	1290	1,95	0,21	1311	2,02	0,25	1248	2,18	0,40
	SD30TW#26	1480	2,28	0,28	1500	2,36	0,34	1482	2,39	0,38
	SD30TW#27	1780	3,10	0,47	1894	3,41	0,66	1685	3,61	1,00
15	SD30TW#28	1860	2,86	0,45	1980	3,21	0,7	1982	338	0,87
	SD30TW#29	1460	3,04	0,38	1520	3,25	0,49	1493	3,44	0,68
	SD30TW#19	1780	2,83	0,42	2050	3,43	0,78	1719	3,66	1,10
	SD30TW#20	1370	2,82	0,33	1520	3,30	0,56	1148	3,55	0,83

(.) discarded

Table 42. Test results in terms of average and standard deviation values relative to Araldite specimens.

Unaged specimens										
		$P_{nl}$	$\delta_{nl}$	$G_{II, nl}$	$P_{max,5\%}$	$\delta_{max,5\%}$	$G_{II, max,5\%}$	$P_u$	$\delta_u$	$G_{II, u}$
		[N]	[mm]	[N/mm]	[N]	[mm]	[N/mm]	[N]	[mm]	[N/mm]
	$\mu$	2053	3,30	0,59	3129	5,26	1,97	2941	6,68	4,11
	$\sigma^2$	0,03	0,03	0,10	0,10	0,11	0,37	0,11	0,11	0,34
Sea Water Conditioned specimens										
Months		$P_{nl}$	$\delta_{nl}$	$G_{II, nl}$	$P_{max,5\%}$	$\delta_{max,5\%}$	$G_{II, max,5\%}$	$P_u$	$\delta_u$	$G_{II, u}$
		[N]	[mm]	[N/mm]	[N]	[mm]	[N/mm]	[N]	[mm]	[N/mm]
1	$\mu$	1345	2,78	0,34	1645	3,61	0,74	1743	6,69	2,64
	$\sigma^2$	0,08	0,09	0,28	0,09	0,10	0,33	0,02	0,02	0,07
2	$\mu$	1883	3,38	0,56	2651	4,99	1,51	3505	8,72	6,08
	$\sigma^2$	0,01	0,01	0,03	0,00	0,00	0,01	0,03	0,01	0,04
3	$\mu$	1098	2,98	0,27	1232	3,47	0,48	1223	4,38	1,01
	$\sigma^2$	0,00	0,00	0,00	0,00	0,00	0,00	0,04	0,00	0,00
5	$\mu$	1460	3,92	0,51	5668	5,30	1,16	2215	7,96	3,51
	$\sigma^2$	0,04	0,13	0,27	1,29	0,10	0,19	0,03	0,06	0,15
6	$\mu$	1870	5,59	0,98	2430	7,56	2,14	2619	9,48	4,21
	$\sigma^2$	0,07	0,14	0,29	0,02	0,09	0,16	0,01	0,01	0,02
9	$\mu$	1170	2,87	0,29	1492	3,85	0,65	2050	6,92	2,94
	$\sigma^2$	0,01	0,01	0,01	0,03	0,02	0,07	0,13	0,12	0,43
12	$\mu$	1430	4,05	0,59	2082	7,73	1,77	1935	9,18	3,28
	$\sigma^2$	0,01	0,11	0,10	0,01	0,01	0,03	0,00	0,00	0,00
Tap Water Conditioned specimens										
Months		$P_{nl}$	$\delta_{nl}$	$G_{II, nl}$	$P_{max,5\%}$	$\delta_{max,5\%}$	$G_{II, max,5\%}$	$P_u$	$\delta_u$	$G_{II, u}$
		[N]	[mm]	[N/mm]	[N]	[mm]	[N/mm]	[N]	[mm]	[N/mm]
1	$\mu$	1293	2,84	0,31	1600	3,72	0,68	1951	6,56	2,80
	$\sigma^2$	0,01	0,02	0,04	0,02	0,05	0,12	0,04	0,06	0,25
2	$\mu$	1560	3,62	0,51	2067	4,97	1,18	3451	10,71	7,03
	$\sigma^2$	0,05	0,01	0,07	0,08	0,02	0,20	0,04	0,00	0,00
3	$\mu$	1233	2,65	0,34	1760	3,91	1,01	3476	12,03	8,55
	$\sigma^2$	0,24	0,24	0,42	0,28	0,28	0,45	0,02	0,01	0,00
5	$\mu$	1483	4,62	0,59	1746	5,69	1,12	1790	7,55	2,61
	$\sigma^2$	0,00	0,01	0,02	0,00	0,01	0,01	0,00	0,00	0,01
6	$\mu$	1825	6,03	0,95	2062	7,08	1,61	1998	8,49	3,01
	$\sigma^2$	0,00	0,03	0,03	0,01	0,02	0,03	0,03	0,01	0,03
9	$\mu$	1223	3,36	0,35	1475	4,25	0,73	1246	5,20	1,45
	$\sigma^2$	0,01	0,01	0,05	0,04	0,04	0,18	0,06	0,07	0,28
12	$\mu$	892	2,60	0,23	1030	3,16	0,38	1060	4,44	0,92

	$\sigma^2$	0,15	0,13	0,38	0,09	0,07	0,21	0,01	0,01	0,03
--	------------	------	------	------	------	------	------	------	------	------

$\mu$  = average values;  $\sigma^2$  = standard deviation

Table 43. Test results in terms of average and standard deviation values relative to SikaDur30 specimens.

Unaged specimens										
		P <sub>nl</sub> [N]	δ <sub>nl</sub> [mm]	G <sub>II, nl</sub> [N/mm]	P <sub>max,5%</sub> [N]	δ <sub>max,5%</sub> [mm]	G <sub>II, max,5%</sub> [N/mm]	P <sub>u</sub> [N]	δ <sub>u</sub> [mm]	G <sub>II, u</sub> [N/mm]
	μ	1577	2,56	0,38	1624	2,72	0,47	1366	2,57	0,58
	σ <sup>2</sup>	0,05	0,01	0,14	0,04	0,02	0,14	0,03	0,02	0,11
Sea Water Conditioned specimens										
Months		P <sub>nl</sub> [N]	δ <sub>nl</sub> [mm]	G <sub>II, nl</sub> [N/mm]	P <sub>max,5%</sub> [N]	δ <sub>max,5%</sub> [mm]	G <sub>II, max,5%</sub> [N/mm]	P <sub>u</sub> [N]	δ <sub>u</sub> [mm]	G <sub>II, u</sub> [N/mm]
1	μ	1283	1,93	0,22	1302	1,99	0,27	862	2,09	0,37
	σ <sup>2</sup>	0,08	0,05	0,19	0,07	0,03	0,12	0,00	0,02	0,09
3	μ	1640	2,61	0,40	1812	2,80	0,54	1427	3,04	0,91
	σ <sup>2</sup>	0,08	0,07	0,26	0,06	0,07	0,29	0,07	0,06	0,19
4	μ	3070	4,41	1,14	3206	4,66	1,35	2073	4,86	2,16
	σ <sup>2</sup>	0,00	0,00	0,00	0,00	0,00	0,01	0,00	0,00	0,00
5	μ	1980	2,89	0,49	2073	3,11	0,62	1881	3,43	1,02
	σ <sup>2</sup>	0,02	0,03	0,11	0,01	0,02	0,06	0,00	0,01	0,05
6	μ	2708	3,75	0,85	2798	3,97	1,07	1925	4,07	1,62
	σ <sup>2</sup>	0,00	0,00	0,00	0,00	0,00	0,01	0,00	0,00	0,01
9	μ	2323	3,33	0,65	2586	3,83	1,02	1704	3,87	1,38
	σ <sup>2</sup>	0,00	0,01	0,02	0,01	0,01	0,03	0,04	0,01	0,04
12	μ	1569	2,16	0,33	1745	2,50	0,47	1215	2,59	0,66
	σ <sup>2</sup>	0,15	0,13	0,63	0,14	0,11	0,46	0,10	0,10	0,49
15	μ	1492	2,33	0,31	1642	2,68	0,48	1385	2,87	0,69
	σ <sup>2</sup>	0,06	0,04	0,16	0,04	0,04	0,17	0,14	0,04	0,13
Tap Water Conditioned specimens										
Months		P <sub>nl</sub> [N]	δ <sub>nl</sub> [mm]	G <sub>II, nl</sub> [N/mm]	P <sub>max,5%</sub> [N]	δ <sub>max,5%</sub> [mm]	G <sub>II, max,5%</sub> [N/mm]	P <sub>u</sub> [N]	δ <sub>u</sub> [mm]	G <sub>II, u</sub> [N/mm]
1	μ	1593	2,45	0,39	1735	2,71	0,57	1311	2,77	0,82
	σ <sup>2</sup>	0,31	0,21	1,08	0,36	0,26	1,13	0,25	0,24	1,18
3	μ	1417	2,23	0,31	1491	2,41	0,43	1180	2,61	0,74
	σ <sup>2</sup>	0,19	0,18	0,57	0,22	0,22	0,74	0,22	0,25	0,78
4	μ	1480	2,40	0,34	1532	2,54	0,44	1393	2,72	0,67
	σ <sup>2</sup>	0,20	0,15	0,40	0,20	0,15	0,38	0,23	0,13	0,35
5	μ	2125	2,98	0,55	2228	3,19	0,72	1514	3,27	1,07
	σ <sup>2</sup>	0,03	0,05	0,15	0,04	0,05	0,17	0,05	0,05	0,16
6	μ	1669	3,04	0,44	1777	3,35	0,65	1411	3,71	1,03
	σ <sup>2</sup>	0,08	0,11	0,19	0,11	0,13	0,26	0,07	0,16	0,25
9	μ	2340	3,44	0,68	2397	3,59	0,82	1591	3,66	1,22
	σ <sup>2</sup>	0,00	0,00	0,00	0,00	0,00	0,01	0,01	0,00	0,00
12	μ	1837	2,61	0,46	1867	2,70	0,54	1249	2,77	0,81

	$\sigma^2$	0,15	0,13	0,44	0,15	0,14	0,44	0,14	0,13	0,44
15	$\mu$	1622	2,82	0,39	1744	3,16	0,59	1585	59,11	0,81
	$\sigma^2$	0,01	0,01	0,03	0,02	0,01	0,06	0,03	4,45	0,08

$\mu$  = average values;  $\sigma^2$  = standard deviation

## **Appendix C.**

In this appendix, all the experimental data recorded, relating to the desorption phenomenon, are collected. In particular, the results reported in each table are referred to the three specimens for each type of condition. Furthermore, the average and standard deviation values are also reported.

Table 44. Experimental data of the absorption and the desorption phenomenon relative to SLJ.

Araldite										
Time [d]	Tap Water					Sea Water				
	#1	#2	#3	$\mu$	$\sigma^2$	#1	#2	#3	$\mu$	$\sigma^2$
0	0,00	0,00	0,00	0,00	0,00	0,00	0,00	0,00	0,00	0,00
1	0,69	0,76	0,72	0,72	0,00	0,53	0,30	0,36	0,40	0,06
2	0,99	1,04	0,98	1,00	0,00	0,65	0,42	0,42	0,49	0,05
3	1,22	1,25	1,28	1,25	0,00	0,79	0,48	0,50	0,59	0,06
4	1,41	1,49	1,45	1,45	0,00	0,84	0,55	0,59	0,66	0,04
7	1,85	1,91	1,96	1,91	0,00	1,05	0,65	0,70	0,80	0,05
8	1,89	1,94	2,08	1,97	0,00	1,10	0,66	0,73	0,83	0,06
9	2,02	2,08	2,20	2,10	0,00	1,15	0,71	0,76	0,87	0,05
10	2,07	2,12	2,25	2,15	0,00	1,16	0,75	0,81	0,91	0,04
14	2,40	2,41	2,62	2,48	0,00	1,38	0,88	0,92	1,06	0,05
15	2,38	2,36	2,60	2,45	0,00	1,34	0,84	0,94	1,04	0,04
16	2,43	2,43	2,72	2,53	0,00	1,43	0,90	0,93	1,09	0,05
17	2,51	2,57	2,82	2,63	0,00	1,49	0,97	0,99	1,15	0,04
21	2,67	2,59	2,93	2,73	0,00	1,63	1,02	1,09	1,24	0,05
22	2,78	2,69	2,94	2,80	0,00	1,67	1,14	1,16	1,32	0,03
23	2,73	2,64	2,96	2,78	0,00	1,61	1,08	1,12	1,27	0,04
24	2,76	2,71	3,02	2,83	0,00	1,71	1,17	1,18	1,35	0,03
28	2,91	2,82	3,11	2,95	0,00	1,86	1,30	1,33	1,50	0,03
31	2,92	2,82	3,11	2,95	0,00	1,86	1,28	1,31	1,48	0,03
35	3,03	2,88	3,15	3,02	0,00	1,96	1,37	1,41	1,58	0,03
38	3,07	2,93	3,21	3,07	0,00	2,10	1,49	1,55	1,71	0,03
42	3,14	3,03	3,28	3,15	0,00	2,22	1,62	1,68	1,84	0,02
45	3,14	3,03	3,34	3,17	0,00	2,30	1,72	1,73	1,91	0,02
49	3,19	3,04	3,26	3,16	0,00	2,27	1,75	1,75	1,92	0,02
56	3,22	3,13	3,38	3,24	0,00	2,59	2,00	2,02	2,20	0,02
63	3,27	3,17	3,35	3,26	0,00	2,62	2,05	2,10	2,26	0,01
86	3,35	3,23	3,38	3,32	0,00	2,98	2,46	2,55	2,66	0,01
115	3,33	3,23	3,38	3,31	0,00	3,22	2,78	2,83	2,94	0,00
172	3,45	3,32	3,45	3,41	0,00	3,47	3,20	3,21	3,29	0,00
262	3,48	3,35	3,48	3,44	0,00	3,50	3,38	3,39	3,42	0,00
378	3,47	3,37	3,51	3,45	0,00	3,64	3,43	3,44	3,50	0,00
379	3,03	3,01	3,06	3,03	0,00	3,04	2,99	2,95	2,99	0,00
380	2,83	2,81	2,88	2,84	0,00	2,83	2,78	2,76	2,79	0,00

381	2,77	2,74	2,81	2,77	0,00	2,74	2,70	2,68	2,71	0,00
382	2,65	2,62	2,72	2,66	0,00	2,61	2,58	2,56	2,58	0,00
383	2,59	2,55	2,65	2,60	0,00	2,55	2,54	2,53	2,54	0,00
384	2,53	2,49	2,59	2,54	0,00	2,50	2,49	2,48	2,49	0,00
385	2,51	2,47	2,58	2,52	0,00	2,50	2,49	2,48	2,49	0,00
386	2,49	2,46	2,57	2,51	0,00	2,49	2,49	2,47	2,48	0,00
387	2,47	2,44	2,55	2,49	0,00	2,48	2,48	2,46	2,48	0,00
388	2,42	2,39	2,50	2,44	0,00	2,43	2,43	2,41	2,42	0,00
389	2,40	2,37	2,48	2,42	0,00	2,40	2,42	2,39	2,40	0,00
390	2,38	2,34	2,46	2,39	0,00	2,37	2,39	2,36	2,37	0,00
391	2,35	2,33	2,44	2,37	0,00	2,36	2,38	2,35	2,36	0,00
392	2,33	2,30	2,42	2,35	0,00	2,34	2,35	2,33	2,34	0,00
393	2,31	2,28	2,39	2,33	0,00	2,31	2,33	2,30	2,32	0,00
394	2,26	2,24	2,36	2,29	0,00	2,26	2,28	2,26	2,26	0,00
395	2,26	2,22	2,35	2,28	0,00	2,25	2,27	2,24	2,25	0,00
396	2,25	2,22	2,35	2,27	0,00	2,24	2,27	2,24	2,25	0,00
397	2,23	2,21	2,33	2,25	0,00	2,24	2,26	2,23	2,24	0,00
398	2,22	2,19	2,30	2,24	0,00	2,22	2,25	2,22	2,23	0,00
399	2,21	2,19	2,30	2,23	0,00	2,22	2,24	2,21	2,22	0,00
400	2,20	2,18	2,29	2,22	0,00	2,21	2,24	2,21	2,22	0,00
402	2,17	2,14	2,26	2,19	0,00	2,19	2,23	2,20	2,21	0,00
406	2,13	2,09	2,21	2,14	0,00	2,15	2,19	2,17	2,17	0,00
409	2,08	2,05	2,17	2,10	0,00	2,11	2,16	2,13	2,13	0,00
413	2,04	2,02	2,13	2,06	0,00	2,07	2,12	2,09	2,09	0,00
416	2,03	2,00	2,11	2,05	0,00	2,07	2,12	2,09	2,09	0,00
420	2,00	1,97	2,09	2,02	0,00	2,07	2,11	2,08	2,09	0,00
427	1,98	1,97	2,00	1,98	0,00	2,07	2,10	2,08	2,08	0,00
435	1,96	1,96	1,96	1,96	0,00	2,06	2,10	2,07	2,08	0,00
441	1,95	1,95	1,96	1,95	0,00	2,06	2,09	2,07	2,07	0,00
445	1,95	1,95	1,95	1,95	0,00	2,05	2,08	2,06	2,06	0,00
511	1,94	1,94	1,94	1,94	0,00	2,04	2,07	2,05	2,05	0,00

$\mu$  = average values;  $\sigma^2$  = standard deviation



## **Appendix D.**

In this appendix, all the ENF test results are reported. In particular, the results collected in Tables 45 and 46 are referred to the SLJ specimens of Araldite and SikaDur 30, respectively.

Furthermore, the values, referred to the unaged and aged (absorption only) specimens, were already published in [30] but are also published here again for the sake of clarity and for a better and rapid comprehension.

Table 45. Test results relating to the Araldite specimens.

Unaged specimens									
Specimen	P <sub>nl</sub> [N]	δ <sub>nl</sub> [mm]	G <sub>II,Pnl</sub> [N/mm]	P <sub>max</sub> [N]	δ <sub>max</sub> [mm]	G <sub>II,Pmax</sub> [N/mm]	P <sub>u</sub> [N]	δ <sub>u</sub> [mm]	G <sub>II,Pu</sub> [N/mm]
ARU#1	2010	3,17	0,54	2064	3,29	0,62	1897	3,66	1,14
(ARU#2)	870	1,50	0,11	893	1,56	0,13	878	1,60	0,16
ARU#3	1500	2,42	0,31	2250	3,82	0,95	2443	5,75	2,81
ARU#4	2350	3,92	0,78	4000	7,02	3,11	4516	9,61	7,56
ARU#5	2350	3,67	0,73	4200	6,91	3,21	2908	7,71	4,91
(ARU#6)	2600	6,27	1,39	3500	8,88	3,47	3113	9,56	5,20
Sea-water conditioned specimens, Absorption									
Specimen	P <sub>nl</sub> [N]	δ <sub>nl</sub> [mm]	G <sub>II,Pnl</sub> [N/mm]	P <sub>max</sub> [N]	δ <sub>max</sub> [mm]	G <sub>II,Pmax</sub> [N/mm]	P <sub>u</sub> [N]	δ <sub>u</sub> [mm]	G <sub>II,Pu</sub> [N/mm]
ARSW#23	1550	5,00	0,67	1930	6,55	1,42	1830	8,85	3,34
ARSW#24	1340	2,78	0,64	2297	8,30	1,95	1966	8,92	3,14
ARSW#31	1600	5,71	0,79	1900	7,14	1,53	1900	9,39	3,44
ARSW#20	1230	2,69	0,28	2200	8,91	2,21	2046	9,57	3,21
(ARSW#21)	1150	2,84	0,28	1250	3,25	0,45	1237	4,37	1,07
(ARSW#28)	330	1,27	0,04	420	1,70	0,08	681	3,69	0,49
Tap-water conditioned specimens, Absorption									
Specimen	P <sub>nl</sub> [N]	δ <sub>nl</sub> [mm]	G <sub>II,Pnl</sub> [N/mm]	P <sub>max</sub> [N]	δ <sub>max</sub> [mm]	G <sub>II,Pmax</sub> [N/mm]	P <sub>u</sub> [N]	δ <sub>u</sub> [mm]	G <sub>II,Pu</sub> [N/mm]
ARTW#22	1080	3,04	0,28	1250	3,71	0,52	1078	4,59	1,02
ARTW#23	1120	2,91	0,28	1220	3,34	0,46	1056	4,40	1,00
ARTW#24	350	1,09	0,03	560	1,84	0,12	891	3,76	0,63
ARTW#30	630	2,07	0,11	780	2,69	0,24	1127	4,76	0,96
ARTW#29	1280	3,88	0,43	1338	4,20	0,59	1147	4,69	1,01
Sea-water conditioned specimens, Desorption									
Specimen	P <sub>nl</sub> [N]	δ <sub>nl</sub> [mm]	G <sub>II,Pnl</sub> [N/mm]	P <sub>max</sub> [N]	δ <sub>max</sub> [mm]	G <sub>II,Pmax</sub> [N/mm]	P <sub>u</sub> [N]	δ <sub>u</sub> [mm]	G <sub>II,Pu</sub> [N/mm]
(ARSW#26)	800	1,27	0,09	1100	1,84	0,22	1055	2,56	0,56
ARSW#27	1640	2,52	0,35	2180	3,53	0,85	2364	5,69	2,82
(ARSW#29)	2080	3,06	0,53	2150	3,33	0,79	2062	4,31	1,74
ARSW#30	2140	3,82	0,69	2480	4,66	1,28	2702	7,98	4,67
ARSW#42	2250	3,81	0,72	2470	4,41	1,21	2585	8,09	4,73
ARSW#43	1950	3,20	0,53	2380	4,11	1,08	3709	7,97	5,33
Tap-water conditioned specimens, Desorption									
Specimen	P <sub>nl</sub> [N]	δ <sub>nl</sub> [mm]	G <sub>II,Pnl</sub> [N/mm]	P <sub>max</sub> [N]	δ <sub>max</sub> [mm]	G <sub>II,Pmax</sub> [N/mm]	P <sub>u</sub> [N]	δ <sub>u</sub> [mm]	G <sub>II,Pu</sub> [N/mm]
(ARTW#25)	1080	2,04	0,19	1250	2,48	0,34	1123	2,64	0,50
(ARTW#28)	730	1,66	0,10	780	1,87	0,16	1253	4,42	1,16
ARTW#38	1550	2,67	0,35	1950	3,54	0,77	2931	8,35	5,30
ARTW#40	1480	2,55	0,32	1780	3,23	0,64	2848	8,71	5,55
ARTW#41	1480	2,64	0,33	1940	3,65	0,79	2113	7,15	3,46

ARSW#42 |2140 3,82 0,69 |2480 4,66 1,28 |2653 8,24 4,67

Table 46. Test results relating to the SikaDur 30 specimens.

Unaged specimens									
Specimen	P <sub>nl</sub> [N]	δ <sub>nl</sub> [mm]	G <sub>II,Pnl</sub> [N/mm]	P <sub>max</sub> [N]	δ <sub>max</sub> [mm]	G <sub>II,Pmax</sub> [N/mm]	P <sub>u</sub> [N]	δ <sub>u</sub> [mm]	G <sub>II,Pu</sub> [N/mm]
SD30U#1	1300	2,50	0,28	1462	2,94	0,47	1406	2,80	0,54
SD30U#2	1115	2,06	0,20	1134	2,12	0,22	917	1,91	0,30
SD30U#3	1620	2,61	0,36	1659	2,70	0,40	1506	2,49	0,51
(SD30U#4)	3750	5,32	1,67	3837	5,47	1,82	2890	5,49	2,92
SD30U#5	2100	3,04	0,62	2055	3,14	0,77	1640	2,98	0,88
SD30U#6	1750	2,57	0,43	1808	2,68	0,49	1362	2,69	0,68
Sea-water conditioned specimens, Absorption									
Specimen	P <sub>nl</sub> [N]	δ <sub>nl</sub> [mm]	G <sub>II,Pnl</sub> [N/mm]	P <sub>max</sub> [N]	δ <sub>max</sub> [mm]	G <sub>II,Pmax</sub> [N/mm]	P <sub>u</sub> [N]	δ <sub>u</sub> [mm]	G <sub>II,Pu</sub> [N/mm]
SD30SW#19	1180	2,00	0,20	1540	2,75	0,47	1418	3,41	0,94
SD30SW#21	1830	2,86	0,44	1990	3,27	0,72	1898	3,31	0,86
SD30SW#22	1850	2,85	0,44	1970	3,19	0,69	1979	3,35	0,86
SD30SW#31	1620	2,28	0,31	1622	2,29	0,31	930	2,33	0,48
(SD30SW#12)	3070	4,51	1,16	3270	5,06	1,83	1971	5,10	2,23
SD30SW#18	980	1,66	0,14	1087	1,92	0,22	698	1,97	0,30
Tap-water conditioned specimens, Absorption									
Specimen	P <sub>nl</sub> [N]	δ <sub>nl</sub> [mm]	G <sub>II,Pnl</sub> [N/mm]	P <sub>max</sub> [N]	δ <sub>max</sub> [mm]	G <sub>II,Pmax</sub> [N/mm]	P <sub>u</sub> [N]	δ <sub>u</sub> [mm]	G <sub>II,Pu</sub> [N/mm]
(SD30TW#25)	1290	1,95	0,21	1311	2,02	0,25	1248	2,18	0,40
SD30TW#26	1480	2,28	0,28	1500	2,36	0,34	1482	2,39	0,38
SD30TW#27	1780	3,10	0,47	1894	3,41	0,66	1685	3,61	1,00
SD30TW#28	1860	2,86	0,45	1980	3,21	0,70	1982	338	0,87
SD30TW#29	1460	3,04	0,38	1520	3,25	0,49	1493	3,44	0,68
SD30TW#19	1780	2,83	0,42	2050	3,43	0,78	1719	3,66	1,10
SD30TW#20	1370	2,82	0,33	1520	3,30	0,56	1148	3,55	0,83

(discarded)



## References

- [1] Correia JR. GFRP pultruded profiles in civil engineering: hybrid solutions, bonded connections and fire behaviour [PhD thesis in civil engineering] Instituto Superior Técnico, Technical University of Lisbon; 2008.
- [2] Carra G, Carvelli V. Long-term bending performance and service life prediction of pultruded glass fibre reinforced polymer composites. *Compos Constr* 2015;127:308–15.
- [3] Machado JJM, Marques EAS, da Silva LFM. Influence of low and high temperature on mixed adhesive joints under quasi-static and impact conditions. *Compos Constr* 2018;194:68–79.
- [4] Liao K, Schultheisz CR, Hunston DL. Effects of environmental aging on the properties of pultruded GFRP. *Compos B Eng* 1999;30(5):485–93.
- [5] Cabral-Fonseca S, Correia JR, Rodrigues MP, Branco FA. Artificial accelerated ageing of GFRP pultruded profiles made of polyester and vinylester resins: characterization of physical-chemical and mechanical damage. *Strain* 2012;48(2):162–73.
- [6] Mara V, Haghani R, Harrysin P. Bridge decks of fibre reinforced polymer (FRP): a sustainable solution. *Constr Build Mater* 2014;50:190–9.
- [7] Minghini F, Tullini N, Laudiero F. Vibration analysis of pultruded FRP frames with semi-rigid connections. *Eng Struct* 2010;32:3344–54.
- [8] Manalo A, Aravinthan T, Fam A, Benmokrane B. State-of-the-art review on FRP sandwich systems for lightweight civil infrastructure. *J Compos Constr* 2017;21(1).
- [9] Report EUR 27666 EN (CEN TC/250). Prospect for new guidance in the design of FRP. JRC Science for Policy Report

(<https://ec.europa.eu/jrc/en/publication/eurscientific-and-technical-research-reports/prospect-new-guidance-design-frp>).

- [10] Mosallam AS. Design guide for FRP composite connections. Manuals of practice (MOP) 102. American Society of Civil Engineers (ASCE).
- [11] Heshmati, M, Haghani, R, Al-Emrani, M. Durability of bonded FRP-to-steel joints: effects of moisture, de-icing salt solution, temperature and FRP type. *Compos B Eng* 2017; 119: 153–167.
- [12] Keller T, Vallée T. Adhesively bonded lap joints from pultruded GFRP profiles. Part I: stress-strain analysis and failure modes. *Compos B Eng* 2005; 36: 331–40
- [13] Razaqpur AG, Ascione F, Lamberti M, Spadea S, Malagic M. GFRP hollow column to built-up beam adhesive connection: Mechanical behaviour under quasi-static, cyclic and fatigue loading. *Compos Struct* 2019; 224, 111069.
- [14] de Castro J, Keller T. Design of robust and ductile FRP structures incorporating ductile adhesive joints. *Compos B Eng* 2010; 41: 148–56.
- [15] Zhang Z, Bay, Y, He X, Jin L, Zhu I. Cyclic performance of bonded sleeve beam-column connections for FRP tubular sections. *Compos B Eng* 2018; 142: 171-182.
- [16] Abbey KJ. *Advances in epoxy adhesives*. Adv. Struct. Adhes. Bond., Woodhead Publishing Limited 2010; 20–34.
- [17] Michels J, Widmann, R, Czaderski C, Allahvirdizadeh R, Motavalli M. Glass transition evaluation of commercially available epoxy resins used for civil engineering applications, *Compos Part B Eng* 2015; 77: 484–493.
- [18] Bowditch MR. The durability of adhesive joints in the presence of water. *Int J Adhes Adhes* 1996; 16: 73–79.

- [19] Hirulkar NS, Jaiswal PR, Reis PNB, Ferreira JAM. Bending strength of single-lap adhesive joints under hygrothermal aging combined with cyclic thermal shocks. *J Adhesion*: <https://doi.org/10.1080/00218464.2019.1681981>.
- [20] Machado JJM, Marques EAS, Barbosa AQ, da Silva LFM. Effect of hygrothermal aging on the quasi-static behaviour of CFRP joints varying the overlap length. *Compos Struct* 2019; 214: 451-462.
- [21] Savvilitidou M, Vassilopoulos AP, Frigione M, Keller T. Effects of aging in dry environment on physical and mechanical properties of a cold-curing structural epoxy adhesive for bridge construction, *Constr Build Mater* 2017; 140: 552– 561.
- [22] Sousa JM, Correia JR, Cabral-Fonseca S. Some permanent effects of hygrothermal and outdoor ageing on a structural polyurethane adhesive used in civil engineering applications. *Int J Adhes Adhes* 2018; 84: 406–419.
- [23] Sousa JM, Correia JR, Gonilha J, Cabral-Fonseca S, Firmo JP, Keller T. Durability of adhesively bonded joints between pultruded GFRP adherends under hygrothermal and natural ageing. *Compos Part B* 2019; 158: 475–488.
- [24] Sousa JM, Correia JR, Cabral-Fonseca S. Durability of an epoxy adhesive used in civil structural applications. *Constr Build Mater* 2018; 161: 618–633.
- [25] Bank LC, Mosallam AS, Gonsoir HE. Beam-to-column connections for pultruded FRP structures. In: Suprenant B, editor. *Serviceability and durability of construction materials. Proceedings of the first materials engineering congress, Denver, CO, 13–15 August, ASCE; 1990. p. 804–13.*
- [26] Bank LC, Mosallam AS, McCoy GT. Design and performance of connections for pultruded frame structures. *J Reinf Plast Compos* 1994;15:1052–67.

- [27] Mosallam AS. Stiffness and strength characteristics of PFRP UC/beam-to- column connections. In: Composite material technology, PD-vol.53, Proceedings, ASME Energy-Sources Technology Conference and Expo, TX, 331 January-4 February; 1993. p. 275–83.
- [28] Mosallam AS, Abdelhamid MK, Conway JH. Performance of pultruded FRP connections under static and dynamic loads. *J Reinf Plast Compos* 1994;13:386–407.
- [29] Bank LC, Yin J, Moore L. Experimental and numerical evaluation of beam-to- column connections for pultruded structures. *J Reinf Plast Compos* 1996;15:1052–67.
- [30] Smith SJ, Parsons ID, Hjelmstad KD. An experimental study of the behaviour of connections for pultruded GFRP I-beams and rectangular tubes. *J Compos Constr* 1998;42:281–90.
- [31] Smith SJ, Parsons ID, Hjelmstad KD. Experimental comparisons of connections for GFRP pultruded frames. *J Compos Constr* 1999;3:20–6.
- [32] Mottram JT, Zheng Y. Further tests on beam-to-column connections for pultruded frames: web-cleated. *J Compos Constr* 1999;3:3–11.
- [33] Mottram JT, Zheng Y. Further tests of beam-to-column connections for pultruded frames: flange-cleated. *J Compos Constr* 1999;3:108–16.
- [34] Qureshi J, Mottram JT. Behaviour of pultruded beam-to-column joints using steel web cleats. *Thin-Walled Struct* 2013;73:48–56.
- [35] Clarke JL. Structural design of polymer composites: EUROCOMP design code and handbook. London: E & FN Spon; 1996.

- [36] Qureshi J, Mottram JT. Response of beam-to-column web cleated joints for FRP pultruded members. *J Compos Constr* 2014;18.
- [37] Qureshi J, Mottram JT. Moment-rotation response of nominally pinned beam- to-column joints for frames of pultruded fibre reinforced polymer. *Constr Build Mater* 2015;77:396–403.
- [38] Zhang Z, Wu C, Nie X, Bai Y, Zhu L. Bonded sleeve connections for joining tubular GFRP beam to steel member: Numerical investigation with experimental validation. *Composite structures* 157 (2016) 51-61
- [39] Wu C, Zhang Z, Bai Y. Connections of tubular GFRP wall studs to steel beams for building. *Construction. Composite part B* 95 (2016) 64-75
- [40] Martins D, Proença M, Correia JR, Gonilha J, Arruda M, Silvestre N. Development of a novel beam-to-column connection system for pultruded GFRP tubular profiles. *Composite Structures* 171 (2017) 263-276
- [41] Ascione F, Lamberti M, Razaqpur AG, Spadea S. Strength and stiffness of adhesively bonded GFRP beam-column moment resisting connections. *Composite Structures* Volume 160, Pages 1248 – 1257
- [42] Russo S. On failure modes and design of multi-bolted FRP plate in structural joints. *Composite Structures* 218 (2019) 27-39
- [43] Qiu C, Bai Y, Zhang L, Jin L. Bending Performance of Splice Connections for Assembly of Tubular Section FRP Members: Experimental and Numerical Study. *Journal of Composites for Construction*, Volume 23 Issue 5 (2019)
- [44] Hizam RM, Manalo AC, Karunasena W, Bai Y. Joint Strength of Single-Bolted Pultruded GFRP Square Hollow Sections with

- Mechanical Inserts under Elevated Temperatures. *Journal of Composites for Construction*, Volume 24 Issue 1 (2020)
- [45] Feng P. Quasi-plastic flexural behavior of adhesive-bolt hybrid connection for large scale pultruded GFRP frame. *Engineering Structures* Volume 238, 1 July 2021, 112200
- [46] Wang J, GangaRao H, Liang R, Zhou D, Liu W, Fang Y. Durability of glass fiber-reinforced polymer composites under the combined effects of moisture and sustained loads. *J Reinf Plast Compos* 2015; 34(21): 1739–1754.
- [47] Ray BC. Temperature effect during humid ageing on interfaces of glass and carbon fibers reinforced epoxy composites. *J Colloid Interface Scienc* 2006; 298: 111-117.
- [48] Bian L, Xiao J, Zeng J, Xing S. Effects of seawater immersion on water absorption and mechanical properties of GFRP composites. *J Compos Mat* 2012; 46:3151-3162.
- [49] Ellyin F, Rohrbacher C. Effect of Aqueous Environment and Temperature on Glass-Fibre Epoxy Resin Composites. *J Reinf Plast Compos* 2000; 19: 1405-1423.
- [50] Kootsookos A, Mouritz AP. Seawater durability of glass- and carbon-polymer composites. *Compos Sci Technol* 2004; 64: 1503-1511.
- [51] Gellert EP, Turley DM. Seawater immersion ageing of glass-fibre reinforced polymer laminates for marine applications. *Compos Part A* 1999; 30: 1259–1265.
- [52] Narasimha Murthy HN, Sreejith M, Krishna M, Sharma SC, Sheshadri TS. Seawater durability of epoxy/vinyl ester reinforced with glass/carbon composites. *J Reinf Plast Compos* 2010; 29: 1491–1499.
- [53] Mourad AHI, Idrisi AH, Wrage MC. Long-term durability of thermoset composites in seawater environment. *Compos Part B* 2019; 168: 243-253.

- [54] Mourad AHI, Abdel-Magid BM, El-Maaddawy T, Grami ME. Effect of Seawater and Warm Environment on Glass/Epoxy and Glass/Polyurethane Composites. *Appl Compos Mat* 2010; 17: 557-573.
- [55] Aktasa A, Uzu I. Sea water effect on pinned-joint glass fibre composite materials. *Compos Struct* 2008; 85: 59-63.
- [56] Wang Z, Zhao XL, Xian G, Wu G, Singh Raman RK, Al-Saadi S, Haque A. Long-term durability of basalt- and glass-fibre reinforced polymer (BFRP/GFRP) bars in seawater and sea sand concrete environment. *Constr build mat* 2017; 139: 467-489.
- [57] Ascione F, Granata L, Lombardi A. The influence of hygrothermal ageing on the strength and stiffness of adhesives used in civil engineering applications: an experimental and numerical investigation. Submitted to *Journal of Adhesion* 2021;  
<https://doi.org/10.1080/00218464.2021.1936507>
- [58] Siriruk A, Penumadu D, Weitsman YJ. Effect of sea environment on interfacial delamination behavior of polymeric sandwich structures. *Compos Scienc Tech* 2009; 69: 821-828.
- [59] SikaDur30 technical data sheet; 2019 – ita.sika.com.
- [60] Araldite technical data sheet; 2020 - huntsman.com.
- [61] Guadagno L, Raimond M, Vertuccio L, Naddeo, C, Barra G, Longo P, Lamberti P, Spinelli G, Nobile MR. Morphological, rheological and electrical properties of composites filled with carbon nanotubes functionalized with 1-pyrenebutyric acid. *Compos B Eng* 2018; 147: 12–21.
- [62] Grammatikos SA, Evernden M, Mitchels J, Zafari B, Mottram JT, Papanicolaou GC. On the response to hygrothermal aging of pultruded FRPs used in the civil engineering sector. *Mat Des* 2016; 96: 283–295.

- [63] de Moura MFSF, de Morais AB Equivalent crack based analyses of ENF and ELS tests. *Eng Fract Mech* 2008; 75: 2584–2596.
- [64] Carlsson LA, Gillespie JW, Pipes RB. On the analysis and design of end notched flexure (ENF) for mode II testing. *J Compos Mater* 1986; 20: 594–604.
- [65] de Morais AB, de Moura MFSF. Assessment of initiation criteria used in interlaminar fracture tests of composites. *Engng Fract Mech* 2005, 72: 2615-2627.
- [66] Blackman BRK, Kinloch AJ, Paraschi M. The determination of the mode II adhesive fracture resistance,  $G_{IIc}$ , of structural adhesive joints: an effective crack length approach. *Engng Fract Mech* 2005; 72: 877–97.
- [67] Blackman BRK, Brunner AJ, Williams JG. Mode II fracture testing of composites: a new look at an old problem. *Engng Fract Mech* 2006; 73: 2443–55
- [68] Wang J, Qiao P. Novel beam analysis of end notched flexure specimen for mode II fracture. *Engng Fract Mech* 2004;71:219–31.
- [69] Ascione F, Granata L, Guadagno L, Naddeo C. Hygrothermal durability in terms of mode II fracture energy of epoxy adhesives used in civil structural applications. *Compos Struct* 2021; 265: 113591.
- [70] Viana G, Costa M, Banea MD, da Silva LFM. Behaviour of environmentally degraded epoxy adhesives as a function of temperature. *J Adhesion* 2017;93: 95-112.
- [71] Ascione F, Lamberti M, Razaqpur AG, Spadea S, Malagic M. Pseudo-ductile failure of adhesively joined GFRP beam-column connections: an experimental and numerical investigation. *Compos Struct* 2018; 200: 864–73.
- [72] EN ISO 62:2008. Plastics-Determination of water absorption.

- [73] Spinelli G, Lamberti P, Tucci V, Vertuccio L, Guadagno L. Experimental and theoretical study on piezoresistive properties of a structural resin reinforced with carbon nanotubes for strain sensing and damage monitoring. *Compos B Eng* 2018; 145: 90–99.
- [74] Lee SW, Hong KJ, Park S. Current and future applications of glass-fibre reinforced polymer decks in Korea. *Struct Eng Int* 2010; 20: 405–408.
- [75] Michels J, Sena-Cruz J, Christen R, Czaderski C, Motavalli M. Mechanical performance of cold-curing epoxy adhesives after different mixing and curing procedures, *Compos Part B Eng*. 2016; 98: 434–443.
- [76] Moussa O, Vassilopoulos AP, Keller T. Effects of low-temperature curing on physical behavior of cold-curing epoxy adhesives in bridge construction, *Int. J. Adhes. Adhes.* 2012; 32: 15–22.
- [77] Top Glass Industries S.p.A; [www.topglass.it](http://www.topglass.it)
- [78] Volkersen O. Die Niekraftverteilung in Zugbeanspruchten mit Konstanten Laschenquerschnitten. *Luftfahrtforschung* 1938;15:41–7.
- [79] Goland M, Reissner E. The stresses in cemented joints. *J Appl Mech* 1944;11:A17–27.
- [80] de Bruyne NA. The strength of glued joints. *Aircraft Eng* 1944;16:115–8.
- [81] Hart-Smith LJ. Adhesive-bonded single-lap joints. NASA 1973:CR-112236.
- [82] Hart-Smith LJ. Adhesive. Bonded double-lap joints. NASA 1973:CR-112235.
- [83] Tsai MY, Oplinger DW, Morton J. Improved theoretical solutions for adhesive lap joints. *Int J Solids Struct* 1998;35(12):1163–85.

- [84] Bigwood DA, Crocombe AD. Elastic analysis and engineering design formulae for bonded joints. *Int J Adhes Adhes* 1989;9(4):229–42.
- [85] Anderson GP, Brinton SH, Ninow KJ, DeVries KL. A fracture mechanics approach to predicting bond strength. *Advances and adhesively-bonded joints*. New York: ASME; 1988. p. 93–101.
- [86] Chai H. Shear fracture. *Int J Fract* 1988;37:137–59.
- [87] Crocombe AD, Hua YX, Loh WK, Abdel Wahab MM, Ashcroft IA. Predicting the residual strength for environmentally degraded adhesive lap joints. *Int J Adhes Adhes* 2006;26:325–36.
- [88] Fernlund G, Papini M, McCammond D, Spelt JK. Fracture load predictions for adhesive joints. *Compos Sci Technol* 1994;51:587–600.
- [89] Papini M, Fernlund G, Spelt JK. The effects of geometry on the Fracture of Adhesive joints. *Int J Adhes Adhes* 1994;14:5–13.
- [90] Suo Z, Hutchinson JW. Interface crack between two elastic layers. *Int J Fract* 1990;43:1–18.
- [91] Tong L. Bond strength for adhesive bonded single lap joints. *Acta Mech* 1996;117:103–13.
- [92] Tsai MY, Morton J. An evaluation of analytical and numerical solutions to the single-lap joint. *Int J Solid Struct* 1994;31:2537–63.
- [93] Keller T, Vallée T. Adhesively bonded lap joints from pultruded GFRP profiles. Part II: joint strength prediction. *Composites: Part B* 2005;36:311–50.
- [94] Keller T, Vallée T. Adhesively bonded lap joints from pultruded GFRP profiles. Part III: Effects of chamfers. *Composites: Part B* 2005;37:328–36.

- [95] Loh WK, Crocombe AD, Abdel Wahab MM, Ashcroft IA. Modelling anomalous mixture uptake, swelling and thermal characteristics of a rubber toughened epoxy adhesive. *Int J Adhes Adhes* 2005;25:1–12.
- [96] Tong L, Sheppard A, Kelly D. Relationship between surface displacement and adhesive peel stress in bonded double lap joints. *Int J Adhes Adhes* 1995;15:43–8.
- [97] Yu XX, Crocombe AD, Richardson G. Material modelling for rate-dependent adhesives. *Int J Adhes Adhes* 2001;21:197–210.